AMINOLYTIC SYNTHESIS AND FERROMAGNETIC RESONANCE OF COBALT AND MANGANESE BASED SPINEL FERRITE NANOPARTICLES

A Dissertation
Presented to
The Academic Faculty

by

Helen Wei-Ya Chen

In Partial Fulfillment
of the Requirements for the Degree
Doctor of Philosophy in the
School of Chemistry and Biochemistry

Georgia Institute of Technology
August 2018

AMINOLYTIC SYNTHESIS AND FERROMAGNETIC RESONANCE OF COBALT AND MANGANESE BASED SPINEL FERRITE NANOPARTICLES

Approved by:

Dr. Z. John Zhang, Advisor
School of Chemistry and Biochemistry
Georgia Institute of Technology

Dr. Younan Xia
School of Chemistry and Biochemistry
Georgia Institute of Technology

Dr. Angus Wilkinson
School of Chemistry and Biochemistry
Georgia Institute of Technology

Dr. John Papapolymerou
Electrical and Computer Engineering
Michigan State University

Dr. Mostafa El-Sayed
School of Chemistry and Biochemistry
Georgia Institute of Technology

Date Approved: May 2, 2018

To my Grandfather

ACKNOWLEDGEMENTS

I would like to convey my gratitude to those who have been supporting me throughout the doctorate program in Georgia Tech. Firstly I would like to thank my advisor, Dr. John Zhang, who has been constantly helping me out with both research guidance and useful life suggestions. He has been a truly great mentor and made my PhD journey with a lot less struggles. His insightful ideas and interesting stories have been the main stepping stones for me to finish the program. I would also like to thank my committee members Dr. Angus Wilkinson, Dr. El-Sayed, Dr. Younan Xia and Dr. John Papapolymerou for all their feedback and comments for my thesis works. Their suggestions have definitely improved my dissertation quality. I would like to thank Dr. Xia for the help in acquiring ICP-MS data and Dr. Papapolymerou for the collaboration of the film project.

I would also like to take this opportunity to express my gratitude towards to past and present group members for their help in lab. I would like to thank Dr. Dan Sabo who answered all my experiment questions and gave me research suggestions even though he did not really overlap with me in the presence in the group. I would also like to thank Julianne Robbins who introduced the lab to me for the very first time and showed me all the basic setups. Her company in the group really helped me to adapt to PhD student life quickly. I would like to thank Eric Drew, who has been helping me

with all the lab chores and having insightful conversions, which led to several research breakthroughs, with me. I really appreciate all his help and suggestions as well as his humorous comments. I would also like to thank Yi Cao, who helped taking care of the lab and continuing part of my projects so that I could focus on working my final dissertation without worries. Her strong sense of responsibility has eased my nerves.

Finally I would like to thank my family and friends for their support. Although they are eight thousand miles away my parents have always been there for me with the strongest support and patience. My brother has always reminded that I am not alone and he also takes great care of the family so that I could concentrate on my studies. I would like to thank all my friends, no matter they are in Atlanta or not, they have provided the timeliest consolation for me and have been there for me to relax and re-charge. I truly appreciate all the help along the way for me to become a Dr.!

TABLE OF CONTENTS

LIST OF FIGURES

LIST OF TABLES

SUMMARY

Magnetic ferrite nanoparticle is a potential material in a number of fields such as catalyst system, data storage, sensors and bio-medical usages. Designing of such applications requires the fine-tuning of magnetic properties through synthesis by chemical composition and dimensional control. In order to manipulate the specific material performance, the fundamental relationship between the microstructure and magnetic properties is a topic of high interests. Spinel ferrite materials often have a strong coupling to electromagnetic signals due to high permeability and permittivity and thus could be used in a variety of microwave devices, e.g. from military shielding to wireless communication signal enhancement. The purpose of this thesis is to study the magnetic correlations and ferromagnetic resonance (FMR) through different spinel ferrite nanoparticles with systematic size and composition variations, and thus one could design materials that meet the best application properties. **Chapter 2** studies the versatility and mechanism of aminolytic method, the nanoparticle synthesis method which has been developed in Zhang group. It is shown that with fine controls of synthesis conditions, a wide range of spinel ferrites with different sizes and compositions can be made successfully. **Chapter 3** utilizes aminolytic method and investigates the magnetic property changes with rare-earth elements substitution within spinel ferrite lattices. In **Chapter 4**, a series of spinel ferrite nanoparticles were

made and their physical properties were examed with different techniques including SQUID (superconducting quantum interference device) magnetometry and EPR (electron paramagnetic resonance) spectroscopy. A negative correlation between magnetic susceptibility (χ) and FMR field (H) has been found and it provides a shortcut to foresee H with one single measurable χ without further structural information such as degree of inversion and magnetic structures. **Chapter 5** investigates the detailed quantitative correlation between magnetic susceptibility (χ) and FMR field (H) with a series of $MnFe_2O_4$ (3-9 nm), $Zn_xMn_{1-x}Fe_2O_4$ and $Co_xMn_{1-x}Fe_2O_4$. This chapter also demonstrates how one could tune FMR absorption profile (both H and ΔH) of the material through synthesis controls. **Chapter 6** explores the fabrication of nanomagnetic films and their microwave absorption performance in wireless communication devices. This provides the way to utilize well-designed particles in film forms for actual applications. The thesis ultimate goal is to understand the physical properties of magnetic solids through the systematic studies and further satisfy the need of certain material applications.

CHAPTER 1. INTORDUCTION

1-1 Background of magnetism

1-1-1 Background and brief theory[1-5]

Magnetism has been discovered and applied in uses as early as the 12th century when lodestone compasses were designed to navigate for sailing. But however it was not until the 1930s that magnetic materials have been widely studied for their magnetic, structure, and electronic properties. The magnetism in the magnetic material arises from the spin magnetic moments: the intrinsic electron spin and the orbital angular momentum from the motion of the electrons around the nucleus. As the Pauli's exclusion principle states, in which that only two electrons with opposite intrinsic magnetic moments (spins) can be paired and occupy into the same orbital, the electrons within the materials would preferentially adopt arrangements where the magnetic moment of each electron is cancelled by its paired counterpart, the opposite moment of another electron. Thus it is often to find magnetic materials contain unpaired electrons. It is also worthy to note that even when the electron configuration of a certain material contains unpaired electrons and/or non-filled subshells, it is possible to find that the various electrons in the solid contribute magnetic moments

pointing in random directions, and as a result, the material would not appear to be magnetic. In addition to the intrinsic magnetic moment arising from the spin of the unpaired electrons, the moment arising from orbital angular momentum could not be ignored in the cases of rare earth elements, in which the *f* orbitals are occupied. The magnetic behavior of a material depends on both the electron configuration of the composed atoms/ions but also the atomic structure. Metal oxides, alloys and other compounds containing magnetic metal ions are the most common magnetic materials.

Based on the magnetic response under an applied magnetic field, one certain material can be classified into one certain magnetism; and those different magnetic classes have different magnetic moment orderings. The magnetic induction of a material while being placed in an applied magnetic field can be described as:

$$\mathbf{B} = \mathbf{H} + 4\pi M$$

Where **B** is the magnetic induction and **H** is the applied field and *M* represents the magnetic moment of the material per volume. If we divide the equation by the applied magnetic field, one could get the following relation:

$$\frac{\mathbf{B}}{\mathbf{H}} = 1 + 4\pi\frac{M}{\mathbf{H}} \equiv P = 1 + 4\pi\chi$$

The ratio of magnetic induction over the applied field is the permeability (P) and χ is

the magnetic susceptibility. One material can be easily classified using its magnetic susceptibility. There are five major classes of material magnetism: diamagnetism, paramagnetism, ferromagnetism, antiferromagnetism, and ferrimagnetism.

Diamagnetism

Diamagnetism is a fundamental property of all matter even though it is usually weak compared to other magnetisms. This is arising from paired electrons, i.e., diamagnetic materials contain no net magnetic moments. When the material is exposed to an external field, a negative magnetization would be produced against the applied field, and thus exhibit negative susceptibility and permeability value less than one. In addition, the susceptibility is temperature independent.

Paramagnetism

Paramagnetism arises from unpaired electrons with an overall zero magnetic moment, i.e., the magnetic spins do not interact with each other. According to the Langevin model, the magnetic moments (from the spin of each atom/ion) are

randomly oriented due to thermal agitation. When the material is experiencing an external field, the moments would start to align with the field. With a higher temperature, it would become more difficult for the moments to align with the field since the thermal agitation increases. This could be described by Curie' Law:

$$\chi = \frac{C}{T}$$

Where C is the Curie constant and T is temperature. Curie's Law is only applicable to systems containing non-interacting magnetic moments. In this case, a positive susceptibility and permeability larger than one could be obtained.

Ferromagnetism

Ferromagnetic materials contain magnetic moments that are aligned parallel to each other and exhibit a positive exchange interaction due to the lattice arrangements. This would result in a positive and large susceptibility and permeability much larger than one. It was initially proposed by Weiss in 1907 that within these materials, there are domains where the magnetic moments would align with respect to each other, which mainly due to the presence of the molecular field from the material. While experiencing an external field, the domain walls would move and result in an induced

magnetic moment. In quantum mechanics, the Heisenberg model of ferromagnetism is used, and it describes the parallel alignment of magnetic moments in terms of an exchange interaction between neighboring moments. Ferromagnetism behavior is temperature dependent since above a critical temperature, Curie temperature (T_c), the large thermal fluctuations would override the exchange interactions and the material would behave as paramagnetism. This could be described as the Curie-Weiss Law:

$$\chi = \frac{C}{T - \theta}$$

Where is the same as the Curie's law but with an extra θ which is a temperature constant.

Ferrimagnetism and Antiferromagnetism

In the comparison of the strictly-defined ferromagnetism, in which all of the magnetic moments are aligned and adding a positive contribution to the net magnetization, ferrimagnetic materials contain some of the magnetic moments subtract from the net magnetization (if they are partially anti-aligned). In the extreme case where the sublattices with anti-aligned magnetic moments result in zero net magnetization, the material exhibits antiferromagnetism. All of these anti-alignment

effects take place at temperatures below the T_C, (for ferrimagnets) or the Neel temperature (T_N) (for antiferromagnets). Ferrimagnetism behaves similarly as ferromagnetism but with a lower saturation magnetization. Antiferromangetic materials would have a positive susceptibility and permeability larger than one.

The classifications are listed in Fig. 1-1 as a brief illustration[6]:

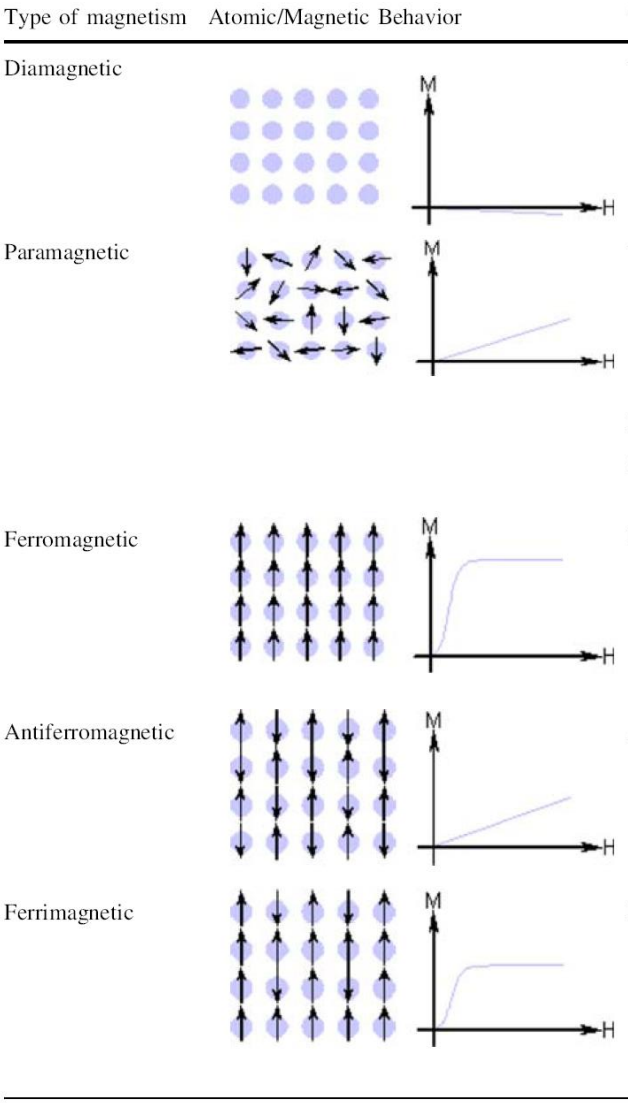

Fig. 1-1 Brief illustration of different magnetisms based on their susceptibility (which is temperature dependent as described in the paragraph. (reprinted from *J. Mater. Sci.-Mater. Electron.* **2009)**

1-1-2 Experimental measurements[1,2,5]

Besides the temperature dependent susceptibility measurements described previously to mainly distinguish out the magnetism classification under different temperature, field dependent hysteresis loop measurement is a common experiment for studying the magnetic materials. A permanent magnet is the magnetic material in which the magnetic moments do not relax to zero after it is magnetized with an applied field. Fig. 1-2 shows a typical hysteresis loop example.

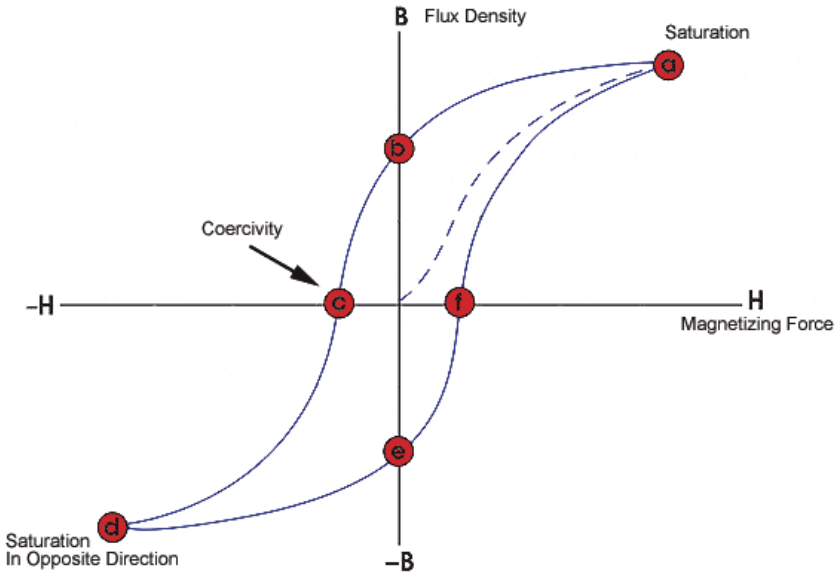

Fig. 1-2 Typical hysteresis loop for a magnetic sample. (reprinted and modified from NDT online education source[7]

Points (a) and (d) mark the saturation magnetization (M_S) which is the maximum amount of magnetization that the system could achieve with an external field. Points

(b) and (e) mark the remanent (remnant) magnetization (M_R). This is the magnetization the system would retain once the applied field is removed. The points (c) and (f) represent the coercivity (H_C) which is the magnetic field strength needed to reverse the direction of the magnetic moments and to remove this retained magnetization. The larger the loop is, the harder the magnet is, i.e., being more difficult to de-magnetize once it is magnetized.

In a typical magnetic property characterization, a temperature dependent susceptibility would be measured to confirm the material magnetism under the certain interested temperature. And once the temperature is selected, a hysteresis loop measurement could provider further magnetism behaviors so

1-2 Domain theory and superparamagnetism[1,2,6,8-10]

Magnetic domain theory was firstly developed by Pierre-Ernest Weiss in 1906 and later got modified with quantum theory. It was proposed that large number of atomic magnetic moments would align parallel, forming one domain, and the direction of alignment varies from domain to domain, which separated through domain walls. A bulk material would have a multi-domain structure since it contains a collection of magnetic domains. This multi-domain structure can effectively reduce the magnetostatic energy, which is caused from the extending magnetic field in space.

Studies have shown complicated changes of magnetic moments of a multi-domain material under different applied fields. It has been shown that not only the moment alignment but also the movements/ changes of the domain walls would occur. Domain wall is a theoretical concept and its movement could be affected by many factors so that experimentally it is difficult to illustrate.

As the grain size of a material is reduced to a critical point, a single domain structure could be obtained. When each particle contains only one domain, there is no longer the domain wall issue and this results in uniform magnetization. The magnetic properties could also be correlated directly to the magnetic structure of the materials since the spin moments determine the magnetism exclusively. Fig. 1-3 illustrates the domain wall concepts.

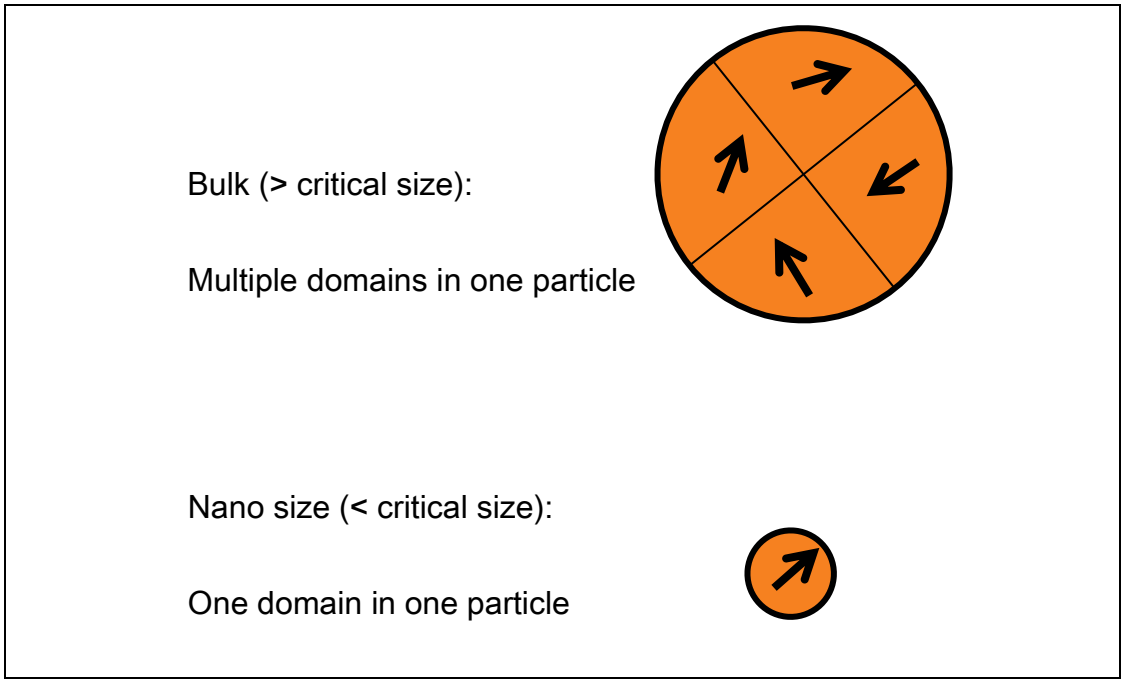

Fig. 1-3 Figure illustration of the multi-domain and dingle domain structures

A special magnetism occurs for single domain materials: superparamagnetism. The magnetization of the single domain is collinear with its easy axis of magnetization and as the temperature increases, random fluctuations occur which results in a paramagnetic behavior. These materials show paramagnetism even at temperature below their T_c (of their bulk counterpart). The magnetic susceptibility, however, is much larger than a normal paramagnetic material. Stoner-Wohlfarth model describes the reversal of magnetization of the particle by magnetization coherent rotation. The following equation illustrates the magnetic anisotropy of a non-interacting single domain particle with a uniaxial anisotropy:

$$E_A = KV \sin^2 \theta$$

E_A is the energy barrier of the nanoparticle, K is the magnetocrstallie anisotropy constant, V is the particle volume, and θ is the angle between the particle mament and its easy axis. Blocking temperature, T_B, is a special term for magnetic nanoparticle materials. Above the blocking temperature, the particles show superparamagnetism and below T_B ferrimagnetism or ferromagnetism would be appeared. The blocking temperature is correlated with the E_A in the Stoner-Wohlfarth model.

1-3 Magnetic nanoparticles: structures, applications and synthesis

1-3-1 Spinel ferrites and other microwave ferrites[2,6,7,11-14]

Magnetic nanoparticles have been applied in numerous application fields such as catalyst systems, data storage, sensors, and bio-medication usages. In this thesis, the applications in microwave technology would be focused. Due to their low radio frequency (RF) loss, various ferrimagnets have been used in RF/ microwave device components such as circulators, phase shifters, antennas… etc. Ferrite nanoparticles have been shown great potential due to their magnetic property tailorability, low eddy curret losses, and high permeability. Spinel ferrites are especially widely studies since its magnetic structure is easy to tune and it is as well relatively cheap and easy to prepare. Garnet ferrites and hexaferrites are also great candidate materials but more synthesis efforts would be required for further applications. In this thesis, various

spinel ferrite nanoparticles would be made and studied thoroughly both structurally and magnetically and further incorporation into actual RF applications setups would be investigated.

Spinel Ferrites

Spinel structure has the general formula as AB_2O_4 where *A* represents tetrahedral cation sites and *B* represents octahedral sites within the closed packed cubic lattice of oxygen ions. As shown in Fig. 1-4, within the spinel lattice, 8 *A* sites and 16 *B* sites are occupied by divalent and trivalent cations with various cation occupancies. A more detailed general formula for spinel ferrites can be written as $(M^{2+}_{1-\delta}Fe^{3+}_{\delta})_A[M^{2+}_{\delta}Fe^{3+}_{2-\delta}]_BO_4$ where ions inside the round brackets are in *A* sites and the ones in the square brackets are in *B* sites. The number δ is the inversion degree which describes the material tendency towards to an inversed spinel ferrite structure, in which the divalent ions only occupy in *B* sites. Both the cation size and crystal field stabilization energy play important roles for occupancy preferences.

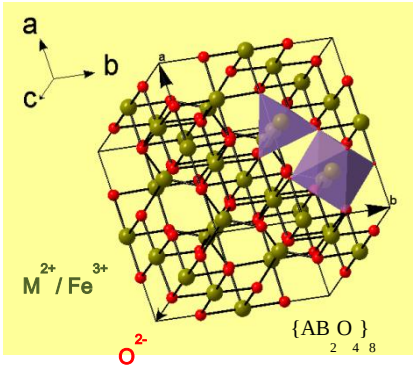

Fig. 1-4 Spinel ferrite unit cell with A and B cation sites

The most intriguing aspect of spinel ferrite materials is their magnetic ordering within the lattice. Antiferromagnetism arises as a result of the cation sites (*A* and *B*) arrangement within the lattice structure. While *A* site cations align parallel with other *A* site cations and so do the *B* site cations which align parallel to each other, the alignment between *A* sites and *B* sites is anti-parallel. The A-B superexchange interaction is the main cause for the observed magnetism. As it is possible to mix different components and tune the degree of inversion through various synthnesis routes, all different magnetic properties including magnetic moments, super-exchange strength, and Neel/ blocking temperature.

Garnets and hexaferrites

Even through spinel ferrites have been studied extensively for microwave applications, garnet ferrites show lower losses and are potentially the best microwave

material in the 1–10 GHz band. A general formula for garnets is written as $Me_3Fe_5O_{12}$ (Me = Er, Dy, Sm, Y trivalent ions). The garnet unit cell is relatively larger, and there are three metal cation sites: *A* with 16 Fe^{3+}, *B* with 24 Fe^{3+} and *C* with 24 Me^{3+}. Between *A* and *B* the alignment is antiparallel and *C* is again antiparallel to the summation of *A* + *B*. Yttrium iron garnet is a common garnet example, in which Y(III) is nonmagnetic so that the resulting magnetic moment is due to the superexchange between *A* and *B* only. Hexaferrites have been gaining more and more attention especially for 1–100GHz band materials. Since hexaferrites are usually hard magnets with high coercivity, the strong internal anisotropy could sufficiently decrease the external field for achieving the target ferromagnetic resonance condition. There are several different types of hexaferrites and the phase diagram is shown in Fig. 1-5, mainly denoted as M, W, Y and Z types. The most common example is barium ferrite,$BaFe_{12}O_{19}$, which has an anisotropy field of 17k G and thus could be served as self-bias hexaferrite microstrip circulators.

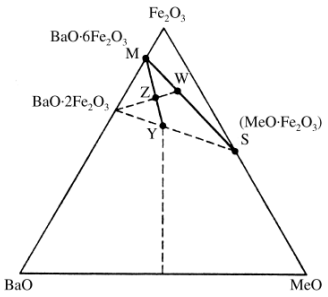

Fig. 1-5 Phase diagram of hexaferrites[14] (reprinted from *J. Magn. Magn. Mater.* **2000**)

1-3-2 Synthesis methods for metal oxide nanoparticles [2,15-23]

Over the past several decades, various new/ updated synthesis methods for the production of metal oxide nanoparticles have been continuously reported. With considerations of cost, recyclability, product quality and yield, the Zhang group has been focusing on three directions: 1) the usage of simple, cheap precursors and add recyclability to the reaction scheme, 2) a simple reaction scheme, in which the target sample could be made with less steps of mechanisms and still result in high yield and good quality product production, and 3) the possibility to produce a wide range of products from the same reaction and equipment, by simply changing precursors or reaction conditions. The previous research within the Zhang group results have been handed down and the synthesis part of this thesis work has been directly undertaken Dr. Dan Sabo's development in aminolytic method. Herein, the following section

would briefly review the main synthetic strategies that have been studied in the Zhang group following the logic based on the thesis of Dr. Sabo. The main developments and also the demonstrations of the aminolytic synthesis strategies can be found in the following chapters.

Micro-emulsion co-precipitation is a well-studied bottom-up synthesis technique for the production of metal oxide nanoparticles. It is usually carried out by mixing source-containing micelles and once the reaction between the precursors occurs, the desired metal oxide particles could form. The micelles act as microreactors and can prevent further aggregation. The quality and size of the micelles are the keys to control the particle size and size distributions. This method requires only simple metal salts as precursors but often a huge amount of solvent consumption is needed. Also it is rare to control the particles size to only several nm ranges. Other advantage of these reactions is the reduced crystal lattice defects and cation distributions that are equalized throughout the particles due to the reaction speed being slow (under room temperature and diffusion through micelles takes time). For the practical applications in the Zhang group, it has been found that the product yield is low and it is difficult to reduce the waste production.

In recent years, the thermal decomposition method has been extensively

researched for the production of nanoparticles, mainly due to its ability to produce tunable and highly crystalline products. The decomposition of certain precursors in the presence of a surfactant dissolved in a high boiling point, non-reacting solvent is the basic concept for the slow sources releasing. It has been found that although with the use of multiple precursors it is possible to produce a range of particles with various compositions, the releasing conditions among different precursors would often mismatch. Another drawback for this method is the large toxic waste-to-product ratio. Many attempts has been made to improve and modify the thermo decomposition method and the aminolytic method actually shares the similar concepts of slowly releasing sources with surfactant protecting.

Other methods such as hydrothermal method and sol-gel methods are both common crystalline synthesis methods which have been established for over 100 years. Both micro-meter and nano-sized crystalline could be made through these routes. The hydrothermal method grows crystals using reactions in a water medium at elevated temperatures and pressures. Although there are no defined lower limits on temperature and pressure for the hydrothermal method, the majority of procedures found today in the literature use temperatures above 100^{o}C and 1 atm (usually less than 300^{o}C and 500 atm). While preparing nano-crystals, the need of capping agents or additional surfactants is essential or otherwise larger crystals would tend to grow.

Sol-gel techniques is also a well-studied method and it has been shown that this method could produce nanoparticles through the use of a gel matrix to control the mixing of precursors. The reaction usually involves the integration of solution of metal alkoxides (sol) into a polymer matrix (gel). Once the precursors are fully incorporated into the matrix, they undergo a hydrolysis reaction which forms the product. But however the final step of the reaction is usually the calcination of the sol-gel and this could cause the agglomeration of the particles and increase the size distribution range.

Dr. Man Han developed a version of the thermal decomposition method that later referred in term as the “aminolytic method”. This method utilizes the use of metal organic precursors (metal acetates) that are suspended with a surfactant (oleylamine) in a high boiling point solvent. It has improved over previous thermal decomposition routes with the application of both the metal acetate precursors and oleylamine. As metal acetates are simple to make in lab and allow for the use of a wide range of metals in various oxidation states, various metal oxides and even metal nanoparticles could be made. The oleylamine serves as both the amine supply (for the reaction initiation) and the surfactant. Another advantage of the aminolytic method was proven by Dr. Lisa Vaughan. She tested the recyclability of this method to investigate if there was any degradation of product yield or crystallinity with repeated use of the high

boiling. Dr. Vaughan has also showed that the dibenzyl ether could be reused ten times without any loss of product or quality. The aminolytic method retains all the advantages of the thermal decomposition method, such as monodispersity and high crystallinity, but at the same time it overcomes the issue of matching thermal decomposition temperature of the precursors. Dr. Sabo has demonstrated that a variety range of metal oxides, including spinel ferrites, manganese oxides and garnet ferrites could be produced through this synthetic route. In this thesis, the proposed mechanism has been verified and extended reaction conditions have been studied for precise controls over phase, size and chemical composition.

1-4 Ferromagnetic resonance[13,14,24-27]

1-4-1 Background and theory

Ferromagnetic resonance (FMR) is a spectroscopic technique to measure the magnetization of the ferromagnetic sample through the detection of precession resonance arising from the sample magnetic moment. This is, conceptually, similar to electron paramagnetic resonance (EPR) and instead of the excitation of unpaired electron spins which occurs in EPR, FMR probes the magnetization from sample dipolar coupling magnetic moments. In a macroscopic view, the external applied field can cause the precession of the net magnetic moment from the sample, and thus once

an RF field that matches the precession frequency is introduced into the system, the resonance condition applies and the RF power could be absorbed. This resonance frequency of the sample is arising from the Zeeman splitting, which shares the same concepts in EPR:

$$h\nu = g_e \mu_B H_0$$

Where hν is the photon energy of the incident wave, which matches the resonance frequency, g_e is the g-factor and μ_B is the Bohr magneton. As shown in Fig. 1-6, the energy splitting of the sample magnetic moment is caused by the external field and the resonance condition matches when the incident frequency is at the same frequency of the energy difference.

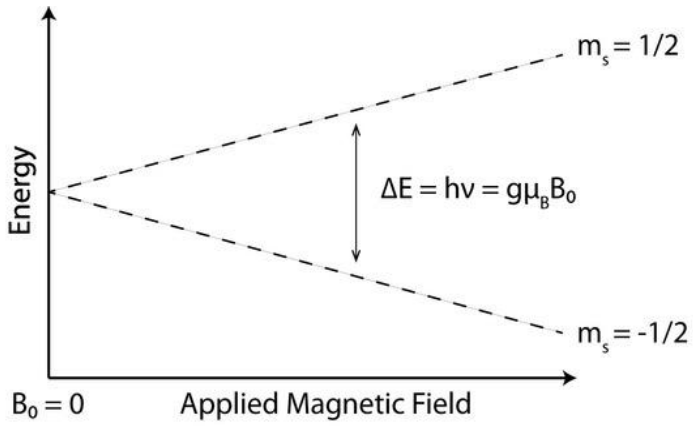

Fig. 1-6 Diagram for EPR/ FMR concept

1-4-2 Experimental setup

The FMR measurements can be done in the EPR instrument and usually the basic setup requires a microwave resonant cavity and an electromagnet. The resonant cavity can be set fixed at a certain frequency based on different microwave band measurements. The magnetic field is swept during the measurement and the absorption of the incident microwave is detected to capture the resonance field when the microwave is absorbed at most. Fig. 1-7 shows the typical experimental setup of the FMR measurements.

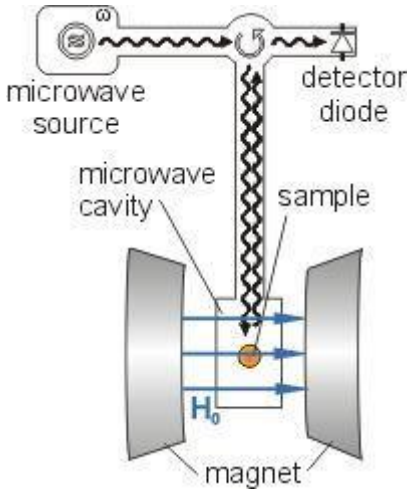

Fig. 1-7 Diagram for FMR/ EPR setup (reprinted from Kuch group techniques, Freie Unucersitat, Berlin[28])

A Bruker EMX spectrometer operating at X-band frequency has been used in this thesis work. The spectra were recorded under room temperature (300 K) and with ν = 9.88 GHz, center field = 5125.0 G, and sweeping width = 9750.0 G. Samples were

prepared by suspending nanoparticle powders into KCl with 1–10 % (wt./ wt.) dependent on different compositions. Both the resonance field and the linewidth were extracted from the first derivative absorption plots.

1-5 Instrumentation

1-5-1 Powder X-Ray Diffraction[29-32]

Powder X-ray Diffraction (XRD) is a valuable analytical technique that is useful for structural analysis for crystalline materials. It is a nondestructive and rapid method for determining the crystalline phase of the sample. For the experiments in the following chapters, the Bruker D8 Advanced X-ray diffractometer with a Cu-Kα source was used for phase analysis. Comparison of the sample diffraction pattern to the patterns reported in the International Centre for Diffraction Data's Powder Diffraction File (ICDD file number), the phase(s) of the sample along with its lattice data and grain size can be determined.

XRD patterns are results from the constructive interference of reflected x-rays satisfying Bragg's Law. When the inter-planar crystalline spacing, d, is an integer multiple of the x-ray's wavelength, the diffracted X-ray would constructively interfere. Note that in the setup here, the incident x-ray is at a fixed wavelength, 1.54 Å for the Cu-Kα source. The Bragg's Law relation is as following:

$$n\lambda = 2dsin\theta$$

Where n is the order of diffraction, λ is the wavelength of the incident beam, d is the inter-planar spacing of the crystal, and θ is the angle of reflection of incidence.

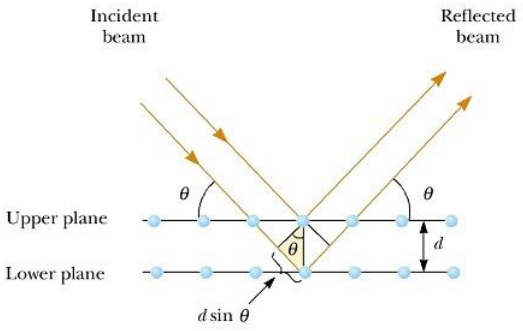

Fig. 1-8 A two-dimensional description of the reflection of an x-ray beam from two parallel crystalline planes. The beam reflected from the lower plane travels farther than the one reflected from the upper plane by a distance 2dsinθ (reprinted from KSHITIJ Online education source)

In addition to the pattern identification of crystalline phase, the Scherrer equation analysis calculating the particle average size has also been applied extensively throughout the following chapters. The Scherrer equation is:

$$d = \frac{K\lambda}{\beta cos\theta}$$

where d is the average dimension of the crystal perpendicular to the reflection planes, K is the Scherrer constant which 0.9 is used for sphere shape approximation, λ is the

X-ray wavelength, θ is the Bragg angle, and β is the full width at half maximum (FWHM) of the diffraction peak (in radians).

1-5-2 Transmission Electron Microscopy (TEM)[33,34]

Transmission Electron Microscopy (TEM) is a highly useful characterization technique for studying nanomaterials. TEM allows the visualization of the material so that one could study the morphology and size/ shape distribution of the material. The TEM studies were performed on a JEOL 100CX2 at the Center of Nanostructure Characterization, Georgia Institute of Technology. Samples were prepared by dispersing 5-10 mg of sample into 5-10 mL of hexanes. A drop of this solution was then placed on a copper grid and allowed to dry. More stripping/ surface coating procedures would be discussed in the later chapters.

The use of a beam of electrons could result in a resolution into nm range. The electron beam generated by the TEM interacts differently with various materials due to differences in electron density of the sample and thus images could be generated based on those contrast differences. A thin sample (~1μm) on a grid is required in order to obtain a useful image from TEM. It must also be able to withstand vacuum conditions since a TEM is utilized in a UHV environment. In an analogy to conventional optical microscopy, the TEM utilizes the electron beam as the incident

beam and electronmagnetic lens system is used to focus the beam along the path.

1-5-3 Superconducting Quantum Inference Device (SQUID)[35-37]

Superconducting Quantum Inference Device (SQUID) magnetometer is one of the most sensitive magnetometers, with a resolution up to 10^{-11}G. This extremely high sensitivity allows this instrument to be useful for the investigation of magnetic properties of nanoparticles over a wide range of temperatures and applied magnetic fields. The presence of a superconducting coil in SQUID magnetometers require the use of liquid helium in order to operate and to measure samples at low temperatures. All magnetic measurements presented in the thesis were performed on a Quantum Design MPMS-5S with a maximum magnetic field of 5 T.

A typical sample preparation stars with weighing out the powder and then placing it into a gelatin capsule. In a hysteresis measurement, the powder sample is immobilized in icosane ($C_{20}H_{42}$) to prevent physical movement of the sample. The gel capsule is sealed with Kapton tape and inserted into a plastic sample straw. It is important that the materials used to contain the sample are nonmagnetic as to prevent complication in data interpretation. The sample straw is then sealed at one end using Kapton tape and the opposite end is attached to the sample rod, which is then inserted into the sample chamber. The sample chamber is under vacuum in order to prevent

atmospheric gases, O_2 and N_2, from freezing at low temperatures (< 90 K). Detailed measurement setups would be described thoroughly in the following chapters.

1-5-4 Inductively Coupled Plasma Mass Spectroscopy (ICP-MS)

Inductively Coupled Plasma Mass Spectroscopy (ICP-MS) is a technique used for the calculation of metal concentrations in a sample and has a resolution down to one part in 10^{15}. A sample solution is firstly placed in inductively coupled plasma, and while the system is coupling to mass spectrometry, the ions from the plasma are extracted through a series of cones into a mass spectrometer and separated based on their mass-to-charge ratio and a detector receives the ion signal proportional to the concentration. All measurements for elemental analysis throughout the thesis have been performed with a Perkin-Elmer NexION ICP-MS by the Xia group, Georgia Institute of Technology.

1-6 References

(1) Jiles, D. *Introduction to magnetism and magnetic materials*; CRC press, 2015.

(2) Sabo, D. E., Georgia Institute of Technology, 2012.

(3) Cullity, B. D.; Graham, C. D. *Introduction to magnetic materials*; John Wiley & Sons, 2011.

(4) O'handley, R. C. *Modern magnetic materials: principles and applications*; Wiley, 2000.

(5) McCurrie, R. A. *Ferromagnetic materials: structure and properties*; Academic Press, 1994.

(6) Ozgur, U.; Alivov, Y.; Morkoc, H. *J. Mater. Sci.-Mater. Electron.* **2009**, *20*, 789.

(7) NDT Resource Center; Vol. 2018.

(8) Jun, Y. W.; Seo, J. W.; Cheon, A. *Accounts Chem. Res.* **2008**, *41*, 179.

(9) Osterloh, F. E.; Hiramatsu, H.; Dumas, R. K.; Liu, K. *Langmuir* **2005**, *21*, 9709.

(10) Liu, C.; Zou, B. S.; Rondinone, A. J.; Zhang, J. *J. Am. Chem. Soc.* **2000**, *122*, 6263.

(11) Smart, L. E.; Moore, E. A. *Solid state chemistry: an introduction*; CRC

press, 2012.

(12) Wadas, R. *Google Scholar*, 484.

(13) Harris, V. G.; Geiler, A.; Chen, Y. J.; Yoon, S. D.; Wu, M. Z.; Yang, A.; Chen, Z. H.; He, P.; Parimi, P. V.; Zuo, X.; Patton, C. E.; Abe, M.; Acher, O.; Vittoria, C. *J. Magn. Magn. Mater.* **2009**, *321*, 2035.

(14) Pardavi-Horvath, M. *J. Magn. Magn. Mater.* **2000**, *215*, 171.

(15) Boles, M. A.; Engel, M.; Talapin, D. V. *Chem. Rev.* **2016**, *116*, 11220.

(16) Polshettiwar, V.; Luque, R.; Fihri, A.; Zhu, H. B.; Bouhrara, M.; Bassett, J. M. *Chem. Rev.* **2011**, *111*, 3036.

(17) Kulandaisarny, A. J.; Rayappan, J. B. B. *J. Nanosci. Nanotechnol.* **2018**, *18*, 5222.

(18) Huang, F.; Zhang, H. Z.; Banfield, J. F. *Nano Lett.* **2003**, *3*, 373.

(19) Reyes-Coronado, D.; Rodriguez-Gattorno, G.; Espinosa-Pesqueira, M. E.; Cab, C.; de Coss, R.; Oskam, G. *Nanotechnology* **2008**, *19*.

(20) Song, Q.; Zhang, Z. J. *J. Phys. Chem. B* **2006**, *110*, 11205.

(21) Song, Q.; Ding, Y.; Wang, Z. L.; Zhang, Z. J. *Chem. Mat.* **2007**, *19*, 4633.

(22) Zheng, L.; Zheng, H.; Deng, J. X.; Ying, Z. H.; Wu, J.; Zhou, J. J.; Qin, H. B. In *Advanced Materials and Processes, Pts 1-3*; Guo, Z. N., Ed.; Trans Tech Publications Ltd: Stafa-Zurich, 2011; Vol. 311-313, p 1294.

(23) Liu, C.; Zhang, Z. J. *Chem. Mat.* **2001**, *13*, 2092.

(24) Kittel, C.; McEuen, P.; McEuen, P. *Introduction to solid state physics*; Wiley New York, 1996; Vol. 8.

(25) Von Sovskii, S. V. e. *Ferromagnetic resonance: the phenomenon of resonant absorption of a high-frequency magnetic field in ferromagnetic substances*; Elsevier, 2016.

(26) Cini, A.; Ceci, P.; Falvo, E.; Gatteschi, D.; Fittipaldi, M. *Z. Phys. Chemie-Int. J. Res. Phys. Chem. Chem. Phys.* **2017**, *231*, 745.

(27) Yang, X.; Zhou, Z.; Nan, T.; Gao, Y.; Yang, G. M.; Liu, M.; Sun, N. X. *J. Mater. Chem. C* **2016**, *4*, 234.

(28) Kuch, W.; Freie University.

(29) Pecharsky, V.; Zavalij, P. *Fundamentals of powder diffraction and structural characterization of materials*; Springer Science & Business Media, 2008.

(30) Giacovazzo, C. *Fundamentals of crystallography*; Oxford university press, USA, 2002; Vol. 7.

(31) Klug, H. P.; Alexander, L. E. *X-Ray Diffraction Procedures: For Polycrystalline and Amorphous Materials, 2nd Edition, by Harold P. Klug, Leroy E. Alexander, pp. 992. ISBN 0-471-49369-4. Wiley-VCH, May 1974.* **1974**, 992.

(32) Cullity, B. D. **2001**.

(33) Skoog, D. A.; Holler, F. J.; Crouch, S. R. *Principles of instrumental analysis*; Cengage learning, 2017.

(34) Wang, Z. L. *Adv. Mater.* **1998**, *10*, 13.

(35) Granata, C.; Vettoliere, A. *Phys. Rep.-Rev. Sec. Phys. Lett.* **2016**, *614*, 1.

(36) Drung, D.; Kluwer, Dordrecht: 1996.

(37) Wang, Z. L.; Liu, Y.; Zhang, Z. *Handbook of Nanophase and Nanostructured Materials: Materials systems and applications I*; 2003; Vol. 3.

CHAPTER 2. AMINOLYTIC SYNTHESIS OF SPINEL FERRITE NANOPARTICLES AND THEIR SIZE DEPENDENT MAGNETIC PROPERTIES

2-1 Abstract

In this chapter, the aminolytic method, the main nanoparticle synthesis route applied throughout the thesis, has been carefully studied. The capability to control sizes and compositions has been tested and the reaction mechanism was illustrated. The aminolytic method utilizes metal acetates as precursors and oleylamine as both reaction initiator and surface capping agent so that a wide range of metal oxide nanoparticles could be made without having the issue of mismatch conditions of metal ion releasing from the precursors, a common problem in typical thermal decomposition methods. To illustrate the size control and reaction mechanism of aminolytic method, cobalt ferrite ($CoFe_2O_4$) nanoparticles with size ranging from 6 to 14 nm were made and their size dependent magnetic properties were also analyzed. Other spinel ferrites such as manganese ferrite, magnetite, nickel ferrite and zinc ferrite along with related metal oxide nanoparticles were also synthesized and the

reaction conditions were documented. This chapter demonstrates that with proper combination of metal acetates, solvents and reaction conditions, i.e. temperature, time and atmosphere… etc., various metal oxide nanoparticles with different chemical compositions and sizes can be made through out this single aminolytic method route.

2-2 Introduction

The size-dependent chemical and physical properties displayed by metal and semiconductor nanocrystals have initiated the intensive research in nanomaterials[1,2]. Spinel ferrites form an important class of compounds because of the unique magnetic, electrical and catalytic properties. Among the various ferrite materials, cobalt ferrite ($CoFe_2O_4$) nanoparticles are well known to have high coercivity, moderate saturation magnetization, great chemical stability and mechanical hardness. Hence cobalt ferrite has a wide range of applications such as high density recording media, magnetic fluids, magnetic refrigerants and targeted drug delivery[3-6]. Magnetic and electrical properties of the ferrite nanoparticles are strongly dependent on their size, shape and chemical purity. Thus with a good control over stoichiometry, crystallite size/ size distribution and particle shape, $CoFe_2O_4$ nanoparticles with desirable properties could be produced and further applied in the specific field[1,5-10].

Research in developing versatile synthesis methods of spinel ferrite nanoparticles has attracted significant attention from both fundamental science and industrial fields. Currently the production of $CoFe_2O_4$ nanoparticles with controllable properties is still a challenge. Conventional synthesis routes include sol-gel processing, hot spraying, evaporation condensation, matrix isolation and thermal decomposition methods[4,9-17]. Generally, under the solution phase synthesis condition, the growth of nanoparticles has most commonly been explained through a La Mer type model based on fundamental thermodynamic principles[1,2,14,18]. According to La Mer plot, during the crystal nucleation process, the concentration of atoms/ ions steadily increases with time as the precursor is decomposed. Colloidal nanocrystal formation comprises the following three steps: (1) the atoms/ ions start to aggregate into nuclei via self-nucleation as increasing the monomer concentration in the solution to supersaturation levels; (2) then monomers continuously aggregate on the pre-existing nuclei or seed which leads to gradual decrease in the monomer concentration. As long as the concentration of reactants is kept below the critical level, further nucleation is discouraged; (3) with a continuous supply of atoms via ongoing precursor decomposition, the nuclei will grow into nanocrystals of increasingly larger size until an equilibrium state is reached between the atoms on the surface of the nanocrystal and the atoms in the solution[2]. Nanoparticles with high quality are

produced by maintaining the growth solution as slightly supersaturated with metal precursors so that the lowest energy equilibrium positions can be attained. Surface stabilizing reagents, i.e. surfactants, are often added as they can effectively prevent the formation of cluster agglomeration during the precipitation process[8,9,15,19,20]. In addition, microemulsion or nanometer cavities are used for isolating nucleation process from the growth stage by decreasing the diffusion rate of new substances towards to the nuclei[14].

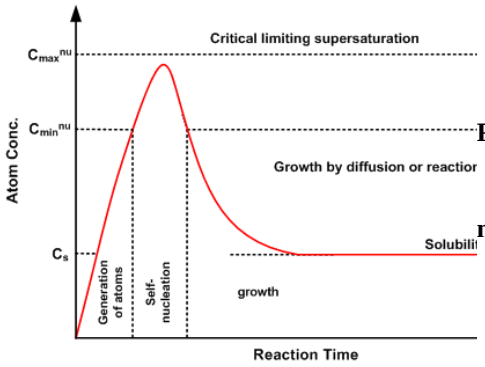

Fig. 2-1 Plot of Lar Mer model showing the nucleation and growth of the particles[2]

Among several synthesis methods for ferrite nanoparticles, thermal decomposition reaction of metal-organic precursor shows excellent control over the particle size distribution and mono-dispersibility[3]. Iron cupferron complex, iron pentacarbonyl, iron acetylacetonate and iron carbocylate complex are all suitable metal precursors which resulted in particles with excellent quality. In order to trigger the reaction with the desired chemical composition, the decomposition temperatures

of different metal precursors should be similar. A large difference in thermal decomposition temperatures among different metal precursors would result in predominant formation of binary metal oxides. Thus the preparation of various metal-organic precursors, which often requires multi-step synthesis and purification process, is necessary in this kind of synthesis method. The formation of a metal oxide is highly dependent on the reaction temperature of the metal precursor. A large difference in reaction temperatures among various metal precursors would result in mixed metal oxides and thus the chemical composition is difficult to control if the target product contains more than one metal cation species.

An alternative way is to apply the aminolytic reaction and use only metal acetates as precursors. According to the Han group, the aminolytic reaction between certain metal acetates and long chain primary amines can produce metal oxides, ZnO mainly, in both high quality and large quantity[21,22]. The intriguing aspect of the aminolytic reaction is that the reaction temperature is independent of metal cations. The formation of amide bonds is thermally activated at 180 ^{o}C as long as metal acetates are used and thus it is possible to synthesize various metal oxides with certain chemical compositions[21,22].

Upon changing the chemical composition, size, and shape of spinel ferrites, the

magnetic properties can be tuned and further applied in different fields. The study of size dependent magnetic properties has been conducted for many spinel ferrite systems. Generally, as predicted by the Stoner-Wohlfarth model, larger nanoparticles have greater magnetic anisotropy energy, E_A:

$$E_A = KV\sin^2\theta$$

where K is the anisotropy energy constant, V is the volume of the nanoparticle, and θ is the angle between the particle easy axis and the applied field direction. Larger E_A results in a higher blocking temperature, which represents the threshold at which thermal activation is strong enough to overcome E_A. In addition, particles with a larger size contain a larger magnitude of net magnetic moment. Therefore, increasing the size of magnetic particles increases the magnitude of the magnetocrystalline energy barrier, and increases in saturation magnetization, remnant magnetization and coercivity are commonly observed[5,9,23-25].

2-3 Experimental

2-3-1 Synthesis of metal acetate precursors

Metal acetate precursors were prepared by reacting metal hydroxide with acetic acid. In brief, $CoCl_2$ (5 mmol) and $FeCl_3$ (10 mmol) were first dissolved in 100 mL of distilled water. Upon the addition of 50 mL of 1.5 M NaOH solution, dark brown metal hydroxide solids precipitated out. The solution was stirred for 2 hours. Then the precipitate was collected and washed 3 times with distilled water through centrifugation. The metal hydroxide solids were re-dispersed in 100 mL of glacial acetic acid (99%) and then dried at 70 ^{o}C for 12 hours. Upon completely evaporating the liquid, a fine powder with stoichiometric ratio of 1:2 mixture Co(II) acetate and iron (III) acetate was collected. Synthesis of individual metal acetate at one time was also applicable.

2-3-2 Synthesis of spinel ferrite nanoparticles

$CoFe_2O_4$ was synthesized via aminolytic reaction. The stoichiometric ratio of 1:2 metal acetate precursors (7.5 mmol) were suspended in a mixture of 10 mL of oleylamine and 40 mL dibenzyl ether (one single mixed acetate precursor and

multiple metal acetates are both applicable; see results in discussion). The turbid metal acetate solution was then heated to 140 ^{o}C and stirred for 1 hour under an Ar-purged reflux system. After all the solids dissolved, the temperature was raised to 240 ^{o}C (or any other certain temperature as described in the discussion section) at ramping rate of 5 ^{o}C/min. and the reaction solution was agitated for a certain reaction time. The reaction was quenched by simply removing the heating bath. The mixture was transferred into a beaker after the reaction solution cooled down to 40 ^{o}C. The nanoparticles were collected by a magnet and washed with ethanol for four times.

2-3-3 Instrumental

Powder X-ray diffraction (XRD) patterns were collected with the Bruker AXS D8 Advance Powder X-Ray Diffractometer with copper Kα source over 15^{o}–85^{o} 2θ range. Particle sizes were determined from the average peak broadening by performing Debye-Scherrer equation analysis with the commercial program TOPAS. Elemental analysis was conducted with Inductively Coupled Plasma Mass Spectrometry (ICP-MS) and the samples were prepared by digesting particles into nitric acid with a final dilution of 100–200 ppb metal ion in 1% HNO_3. Transmission electron microscopy (TEM) measurements were conducted using JEOL 100CX2 at

100 kV. Samples were prepared by dispersion of particles in hexane (sonication > 30 min.) and spread onto copper grids. Magnetic measurements were performed with Quantum Design MPMS-5S Superconducting QUantum Interference Device (SQUID). Zero-field cooled (ZFC) susceptibility measurements were performed under an applied field of 100 G. Hysteresis measurements were performed at 5 K with applied fields up to 5 T. For the hysteresis measurements, the nanoparticles were mixed with eicosane to prevent physical movements of the nanoparticles.

2-4 Results and discussion

2-4-1 Aminolytic synthesis route

The aminolytic reaction between a single metal-acetate precursor and long chain primary amine producing a binary metal oxide is well documented[21,22]. Oleylamine essentially has hydrophobic property at low temperatures due to its long hydrocarbon chain (18-C) with a weak base property. At elevated temperatures, however, thermal energy allows the hydrophilic amine group to interact with a metal acetate precursor, which is a water soluble salt. Initially, the electron rich nucleophile amine group selectively binds with the electrophile (COO^-) and leaves as oleyl acetamide to form

metal hydroxide, which later undergoes a condensation reaction to form metal oxide. As shown in Fig. 2-2, ^{1}H NMR spectrum of the residue shows peak with a chemical shift of 5.56 ppm due to the formation of amide bonds, which confirms the formation of the by-product oleyl acetamide[21]. Formation of amide bonds is a slow process which can be thermally activated (~180 ^{0}C). On the other hand, the condensation reaction of metal hydroxide to metal oxide is a fast process at elevated temperature (180 ^{0}C–270 ^{0}C). Therefore, concentration of the available metal hydroxide can be controlled by thermodynamically reducing the speed of amide bond formation in order to achieve successful separation of the nucleation and growth process. Oleylamine is not only a reaction reagent but also a surface stabilizing reagent. The hydrophilic -NH_2 group of oleylamine has a certain affinity to the surface of the nanoparticle and acts as a surfactant. Forming an oleylamine shell on the surface controls the growth rate of the nanoparticle by limiting the diffusion rate of the available metal precursor onto the surface. In the meantime, the hydrophobic tail allows oleylamine coated nanoparticles to be suspended individually in the dibenzyl ether solvent. Therefore, nanoparticles are dispersed in any organic solvent very well due to the oleylamine coating on the surface. Removal of oleylamine from the surface is demonstrated by multiple dispersions of nanoparticles in organic solvent with precipitation by ethanol. Such a process produces bare nanoparticles that can be

dispersed in a polar solvent.

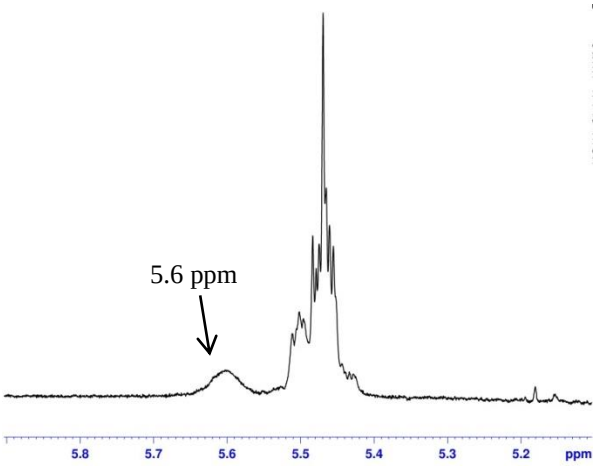

Fig. 2-2 ^{1}H NMR spectrum of the reaction residue of cobalt acetate, ferric acetate and oleylamine. The broad peak with a chemical shift 5.6 ppm confirming the side produt oleyl acetamide (-CO-NH-). Neighboring peaks are attributed to the protons from oleylamine.

2-4-2 $CoFe_2O_4$ nanoparticles and their size dependent magnetic properties

Synthesis of pure $CoFe_2O_4$ by aminolytic method

By varying the reaction temperatures and times during the aminolytic reaction, $CoFe_2O_4$ nanoparticles with different sizes were synthesized successfully. Fig. 2-3

shows the XRD patterns of the resulting particles. With the temperature ranging from 240 ^{o}C to 270 ^{o}C, all samples appeared only single spinel ferrite phase (magnetite JCPDS: 19-0629). In addition, the particle average sizes were analyzed through peak fittings with the Scherrer equation. The relationship of the average size with reaction temperature and time is plotted in Fig. 2-4. Larger particles could be obtained with either increasing the reaction temperature or time. According to the Lar Mer model, increasing the reaction temperature could both increase the monomer concentration and the growth rate. Increasing the reaction time allowed the particles to grow and thus resulted in bigger particles. The chemical compositions were examed by ICP-MS and all the samples contained Fe/Co molar ratio around 2.0 (2.0 ± 0.3). With the success of the synthesis method, other metal acetates were also applied into the system aiming to synthesize various ternary metal oxides.

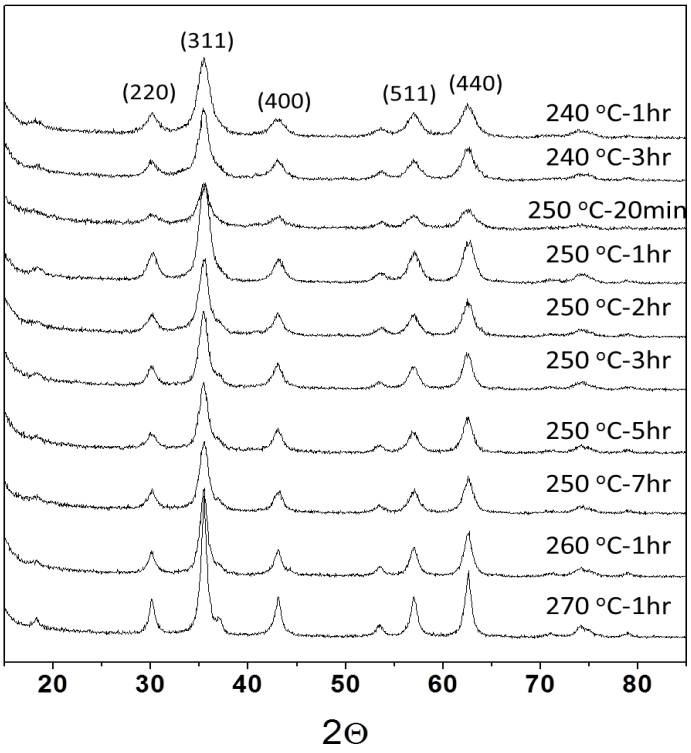

Fig.2-3 XRD patterns of samples with different reaction temperatures and times

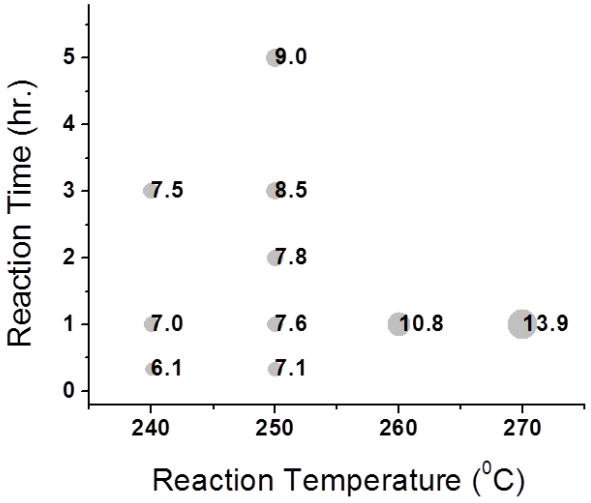

Fig. 2-4 Particle average sizes (nm) with varying reaction temperatures and times

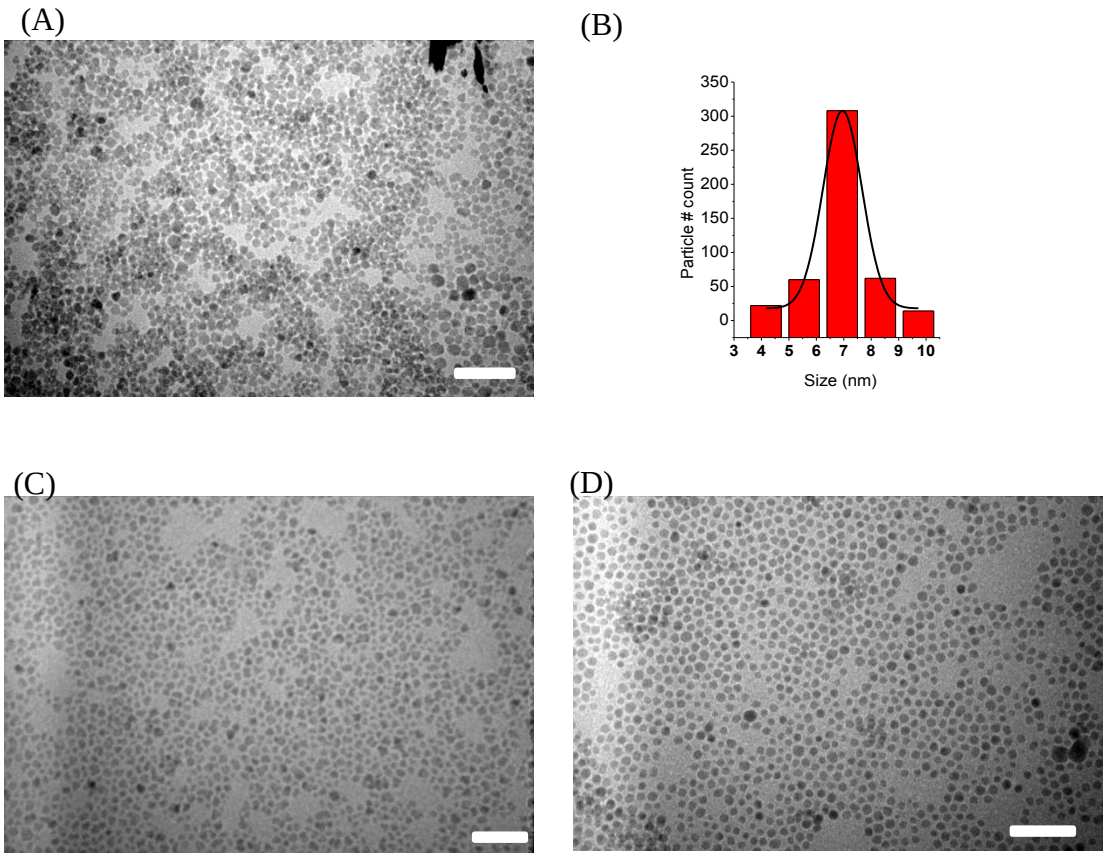

Fig. 2-5 Selected TEM images of the samples. (A) Avg. 7 nm $CoFe_2O_4$ NPs made by aminolytic method (B) Particle size normal distribution fitting of (A). The center is at 6.9 nm and FWHM = 1.7 nm (C) Oleic acid coated $CoFe_2O_4$ NPs made by aminolytic method (D) Avg. 8 nm $CoFe_2O_4$ NPs made by thermo decomposition method (metal acetylacetonates as precursors). Scale bar = 50 nm

The size distributions of the samples were also examined by TEM images (selected images are shown in Fig. 2-5). Fig. 2-5-(A) and (B) demonstrate the typical size distribution analysis of $CoFe_2O_4$ synthesized below 270 ^oC and as shown in (B), the full width at half maximum (FWHM) of the Gaussian normal distribution is 1.7 nm and so that the size distribution is within $\pm$ 12%. Note that while preparing TEM samples, the replacement into oleic acid as the surface capping agent could result in a better particle dispersion as shown in Fig. 2-5-(C). A comparison of particle quality with the $CoFe_2O_4$ made through typical thermo decomposition method, which has been proved to produce homogenous nanoparticles with high quality but smaller batch yield, is shown in (D). In conclusion, aminolytic method could produce $CoFe_2O_4$ nanoparticles with different size ranges and small size distribution successfully with several other advantages such as good batch yield (> 0.5 g/ batch; > 90% yield), cheap metal acetate precursors and reusable solvents.

Size-dependent magnetic properties

The size-dependent magnetic properties of pure $CoFe_2O_4$ nanoparticles are shown in Fig. 2-6 and 2-7. As particle size increases, both magnetic coercivity and blocking temperature increases, which is in accordance with previous research[12,23]. As

predicted by the Stoner-Wohlfarth model, larger nanoparticles have greater E_A and larger E_A results in a higher blocking temperature, which represents the threshold at which thermal activation is strong enough to overcome E_A. In addition, particles with a larger size contain a larger magnitude of net magnetic moment. Therefore, increasing the size of magnetic particles increases the magnitude of the magnetocrystalline energy barrier, and increases in saturation magnetization, remnant magnetization and coercivity are commonly observed.

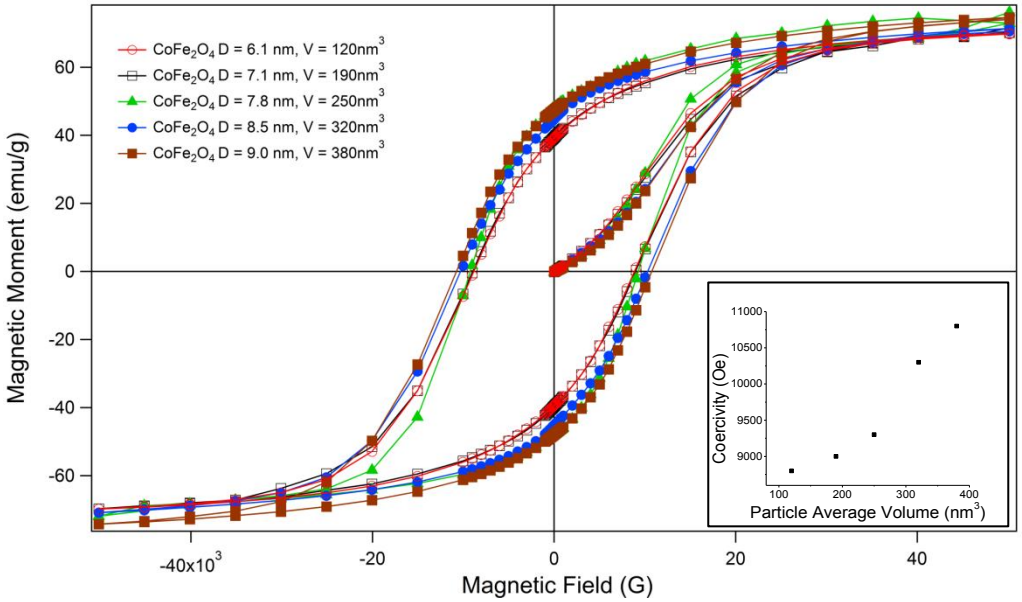

Fig. 2-6 Hysteresis curves at 5 K for $CoFe_2O_4$ NPs with different sizes; the coercivity to particle volume plot is shown in the inset

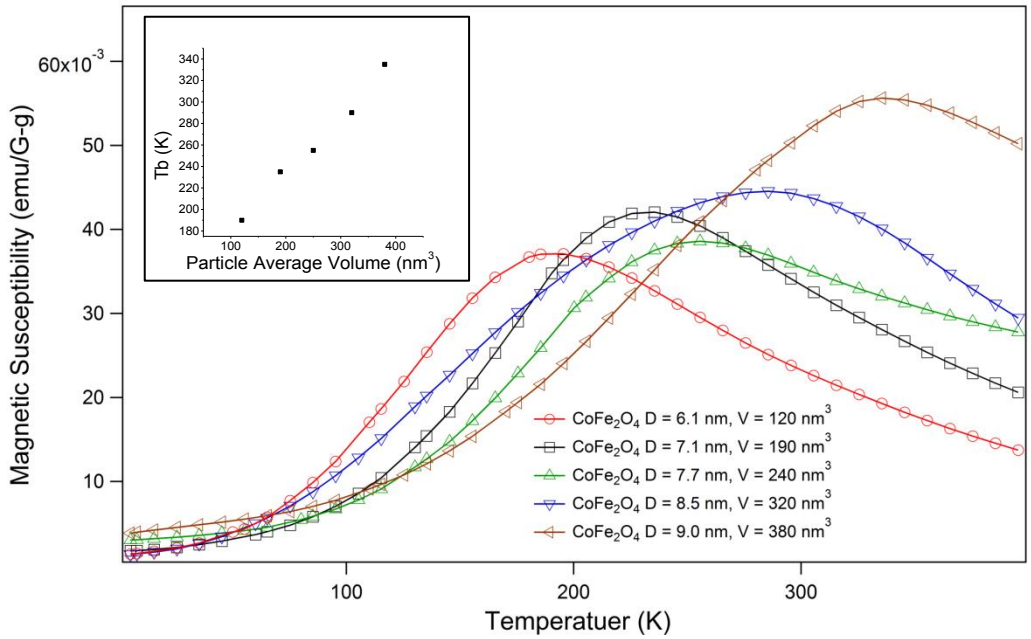

Fig. 2-7 Temperature dependent susceptibility measurements for $CoFe_2O_4$ NPs with different sizes; the blocking temperature to particle volume plot is shown in the inset

2-4-3 Results of other spinel ferrites

It has been demonstrated that $CoFe_2O_4$ nanoparticles could be made through this aminolytic route with tunable sizes and thus other metal acetate precursors were used to verify the capability of composition control using aminolytic method. Different attempts were made to synthesize other spinel ferrites MFe_2O_4, M = Mn(II), Fe(II), Ni(II) and Zn(II). Fig. 2-8 shows the XRD patterns of those attempts and related metal oxides as impurities could be found. Panel (A) shows the mix of both $MnFe_2O_4$ and MnO phases since individual precursors, manganese acetate and iron

acetate, were used during the synthesis. Pure MnO phase could be made when only manganese acetate was used as precursor (as shown in (B)) and pure $MnFe_2O_4$ spinel phase was made successfully when the mixed acetate (manganese/ iron acetate with Mn(II):Fe(III) = 1:2 mol/mol) was used (Fig. 2-8-(C)). Note that similar results could be found in $ZnFe_2O_4$ series since both MnO and ZnO are thermally stable phases compared to spinel ferrites. The usage of mix acetates as precursor is crucial in these cases since the close spatial proximity between the M(II) and Fe(III) could easily result in mixed oxides and further led the reaction towards to the spinel ferrite phase. Panel (D) and (E) demonstrate the case of $ZnFe_2O_4$. Magnetite (Fe_3O_4) could be made by using only iron(III) acetate with a larger quantity of oleylamine so that enough Fe(III) could be reduced into Fe(II) to form the spinel phase. In contrary, without sufficient reducing agent oleylamine, Fe_2O_3 could be seen as the impurity. Fig. 2-8-(F) and (G) demonstrate these different attempts synthesizing magnetite nanoparticles. Fig. 2-8-(H) shows that $NiFe_2O_4$ could be made but Ni metal would also present as an impurity even though the mixed acetate precursor was used. The presence of Ni in the final product means that Ni(II) in the precursor went through a reduction process, $Ni^{2+} + 2e^- \rightarrow Ni^{(0)}$ (E^o = -0.25 V). Since oleylamine is a reducing agent and in this case the reduction barrier is relatively small, Ni nanoparticles could be form.

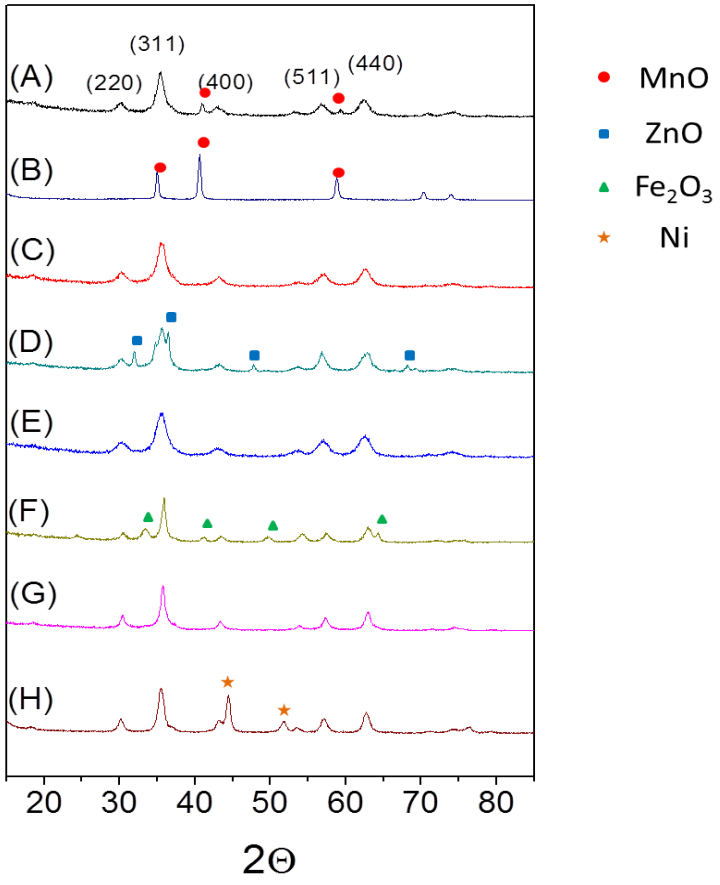

Fig. 2-8 XRD patterns for various attempts making spinel ferrites. (A): Individual acetates, i.e., Mn(II) acetate and Fe(III) acetate, were used and resulted in both spinel phase and MnO impurity. (B): Only Mn(II) acetate was used and MnO pure phase was obtained. (C): Mixed acetate containing both Mn(II) and Fe(III) was used and pure spinel phase was obtained. (D): Individual acetates, i.e., Zn(II) acetate and Fe(III) acetate, were used and resulted in both spinel phase and ZnO impurity. (E): Mixed acetate containing both Zn(II) and Fe(III) was used and pure spinel phase was obtained. (F) Only Fe(III) acetate was used and the oleylamine amount was kept as typical aminolytic method (5 mL/ g precursors). This resulted in both

spinel ferrite phase and Fe_2O_3 impurity. (G) Only Fe(III) acetate was used and the oleylamine amount was increased to 10 mL/ g precursors; which resulted in pure spinel ferrite phase (magnetite). (H) Mixed acetate containing both Ni(II) and Fe(III) was used and Ni metal nanoparticle was found as an impurity phase

Further attempts are still undergoing to create a less reducing synthetic environment to prevent Ni formation. Mr. Eric Drew in the Zhang group has found that with the atmosphere replacement of Ar into O_2 could successfully suppress the Ni(II) reduction and pure $NiFe_2O_4$ spinel phase could be obtained. Currently more tests are undergoing to verify these findings.

With the presence of metal oxides as impurities, the reaction temperature control also becomes a critical parameter since those impurity phases might be more thermally stable than the spinel ferrite phase. Thus the size control could not be easily achieved by using the same approach as shown in the $CoFe_2O_4$ series: change of the reaction temperatures. According to Lar Mer model, with similar amount of overall precursors, more nuclei centers form at once would result in smaller particles. Herein the $MnFe_2O_4$ series was used as an example that temperature ramping rate in the aminolytic method can control particle sizes since it directly control the metal ion releasing rate. The quicker the rate is, more ions releasing out at once and more nuclei

centers would form. Fig. 2-9 shows the XRD patterns of $MnFe_2O_4$ particles synthesized under different temperature ramping rates from 0.92–5.5 ^oC/min. (reaction temperature evaluated from 140–250 ^oC) and particles with different sizes could be obtained. The chemical compositions were also confirmed by ICP-MS to ensure the formation of manganese ferrite spinel and all the samples contained Fe/Mn molar ratio within 2.0 ± 0.3. As particle size increases, the trend of increasing blocking temperature could be seen in accordance with the Stoner-Wohlfarth model, which states that larger nanoparticles have greater E_A and larger E_A results in a higher blocking temperature (Fig. 2-10).

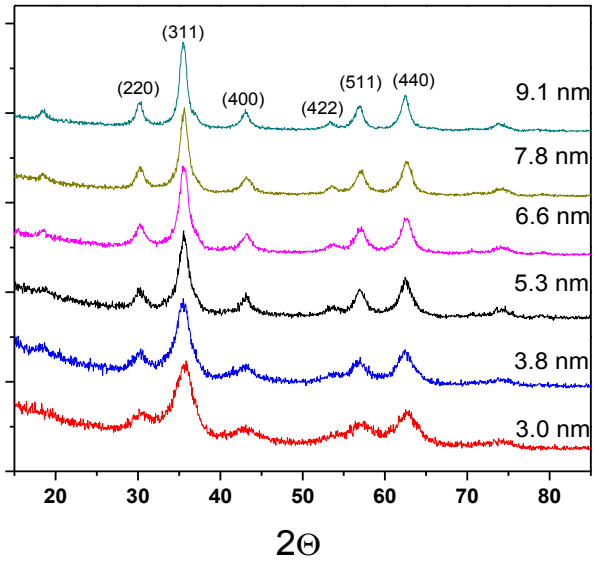

Fig. 2-9 XRD patterns of $MnFe_2O_4$ NPs with different sizes

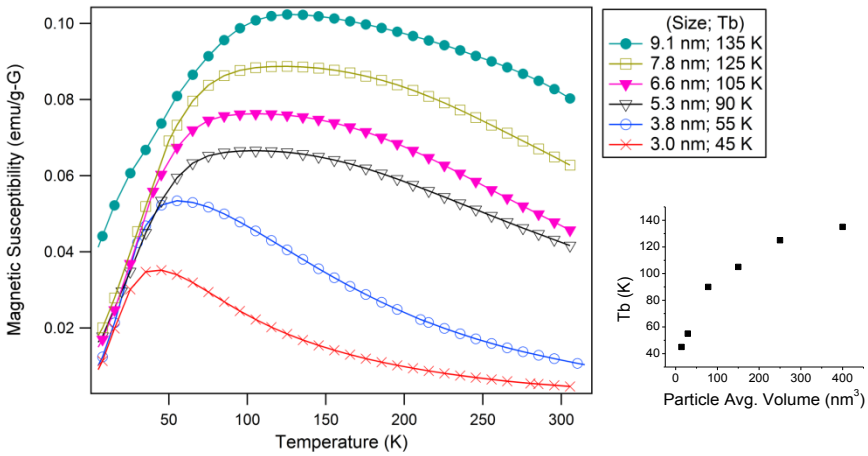

Fig. 2-10 Temperature dependent susceptibility measurements for $MnFe_2O_4$ NPs with different sizes; the blocking temperature to particle volume plot is shown on the right

2-5 Conclusions

In summary, a versatile, inexpensive, environmental-friendly, high-yield and large-scale synthesis method for spinel ferrite ($CoFe_2O_4$, $MnFe_2O_4$, Fe_3O_4 and $ZnFe_2O_4$) nanoparticles has been demonstrated. Multi-cation oxides could be produced through the aminolytic reaction between different metal acetate precursors and oleylamine, and the presence of the by-product oleyl acetamide has proved the

aminolytic mechanism. Chemical compositions and even particle phases can be controlled with proper choices of acetate precursors, reaction temperature and atmosphere. Particle sizes can be tuned by changing the reaction time, temperature, and temperature ramping rate. Particle properties show great quality and size dependent magnetic properties are in good agreement with the theoretical prediction. $CoFe_2O_4$ nanoparticles with size ranging from 6 to 14 nm and $MnFe_2O_4$ particles from 4 nm to 9 nm were made successfully and both series along with the production of other spinel ferrites and metal oxides have demonstrate the capability of aminolytic method.

2-6 References

(1) Alivisatos, A. P. *Science* **1996**, *271*, 933.

(2) Nguyen, T.-D.; Do, T.-O. *Size- and Shape-Controlled Synthesis of Monodisperse Metal Oxide and Mixed Oxide Nanocrystals*, 2011.

(3) Sun, S. H.; Zeng, H.; Robinson, D. B.; Raoux, S.; Rice, P. M.; Wang, S. X.; Li, G. X. *J. Am. Chem. Soc.* **2004**, *126*, 273.

(4) Rajendran, M.; Pullar, R. C.; Bhattacharya, A. K.; Das, D.; Chintalapudi, S.

N.; Majumdar, C. K. *J. Magn. Magn. Mater.* **2001**, *232*, 71.

(5) Moumen, N.; Bonville, P.; Pileni, M. P. *J. Phys. Chem.* **1996**, *100*, 14410.

(6) Kahn, M. L.; Zhang, Z. J. *Appl. Phys. Lett.* **2001**, *78*, 3651.

(7) Cheng, F. X.; Jia, J. T.; Xu, Z. G.; Zhou, B.; Liao, C. S.; Yan, C. H.; Chen, L. Y.; Zhao, H. B. *J. Appl. Phys.* **1999**, *86*, 2727.

(8) Liu, C.; Zou, B. S.; Rondinone, A. J.; Zhang, J. *J. Am. Chem. Soc.* **2000**, *122*, 6263.

(9) Moumen, N.; Pileni, M. P. *Chem. Mat.* **1996**, *8*, 1128.

(10) Komarneni, S.; Li, Q.; Stefansson, K. M.; Roy, R. *J. Mater. Res.* **1993**, *8*, 3176.

(11) Vestal, C. R.; Zhang, Z. J. *Nano Letters* **2003**, *3*, 1739.

(12) Vestal, C. R.; Zhang, Z. J. *Chem. Mat.* **2002**, *14*, 3817.

(13) Vestal, C. R.; Zhang, Z. J. *Journal of the American Chemical Society* **2002**, *124*, 14312.

(14) Cushing, B. L.; Kolesnichenko, V. L.; O'Connor, C. J. *Chem. Rev.* **2004**, *104*, 3893.

(15) Hyeon, T.; Chung, Y.; Park, J.; Lee, S. S.; Kim, Y. W.; Park, B. H. *J. Phys. Chem. B* **2002**, *106*, 6831.

(16) Liu, C.; Zou, B. S.; Rondinone, A. J.; Zhang, Z. J. *J. Phys. Chem. B* **2000**, *104*, 1141.

(17) Komarneni, S.; Roy, R.; Li, Q. H. *Mater. Res. Bull.* **1992**, *27*, 1393.

(18) Roucoux, A.; Schulz, J.; Patin, H. *Chem. Rev.* **2002**, *102*, 3757.

(19) Xiong, G.; Mai, Z. H.; Xu, M.; Cui, S. F.; Ni, Y. M.; Zhao, Z. X.; Wang, X.; Lu, L. D. *Chem. Mat.* **2001**, *13*, 1943.

(20) Rondinone, A. J.; Samia, A. C. S.; Zhang, Z. J. *J. Phys. Chem. B* **1999**, *103*, 6876.

(21) Zhang, Z. H.; Liu, S. H.; Chow, S. Y.; Han, M. Y. *Langmuir* **2006**, *22*, 6335.

(22) Zhang, Z. H.; Zhong, X. H.; Liu, S. H.; Li, D. F.; Han, M. Y. *Angew. Chem.-Int. Edit.* **2005**, *44*, 3466.

(23) Lu, A. H.; Salabas, E. L.; Schuth, F. *Angew. Chem.-Int. Edit.* **2007**, *46*, 1222.

(24) Vestal, C. R.; Zhang, Z. J. *International Journal of Nanotechnology* **2004**, *1*, 240.

(25) Han, M.; Vestal, C. R.; Zhang, Z. J. *Journal of Physical Chemistry B* **2004**, *108*, 583.

CHAPTER 3. SYNTHESIS AND CHARACTERIZATION OF RARE-EARTH ELEMENT SUBSTITUTED COBALT FERRITE NANOPARTICLES

3-1 Abstract

In this chapter, the aminolytic synthesis method has been utilized to incorporate rare earth elements into the spinel ferrite lattice to further study the influence on the magnetic properties. In brief, neodymium and holmium trivalent cations were introduced into cobalt ferrite nanoparticles to partially substitute the iron(III)$_{(Oh)}$ and the effective substitution amount is less than 5%. XRD, ICP-MS elemental analysis and TEM measurements have shown that both the $Nd_xCoFe_{2-x}O_4$ and $Ho_xCoFe_{2-x}O_4$ nanoparticle series appeared as spinel ferrite phase with successful RE substitution and within 7 nm ± 10% size range. Magnetic measurements by SQUID have showed that the small substitution amount (at only ~3%) changes the blocking temperature by 30 K without altering the magnetic hysteresis features. This could be rationalized that the RE substitution brings in multiple effects on the anisotropy and cation distribution changes. The significant change in only the blocking temperature could be useful in

tuning the working temperature of materials in certain application needs.

3-2 Introduction

Metal-substituted cobalt ferrite ($CoFe_2O_4$) nanoparticle is a potential material in a number of applications including data storage, ferrofluid technology, contrast enhancement in MRI, drug delivery system and hyperthermia treatment[1-3]. Designing of such applications requires not only the fine-tuning of magnetic properties by chemical composition and dimensional control, but also inexpensive industry-friendly synthesis methods. Though various synthesis methods have been reported, the synthesis of RE-substituted $CoFe_2O_4$ nanoparticles remains a challenge. The chapter's first aim is to develop a robust synthesis protocol, i.e. the aminolytic nanoparticle synthesis method, in order to control the size and composition of RE-substituted $CoFe_2O_4$. With the success of the synthesis method, we could not only synthesize various $CoFe_2O_4$-based materials but also systematically study the relationship between physical properties and particle size and chemical composition. It has been shown that the exchange interaction between rare earth-transition (3d-4f) metal elements can lead to changes of magnetic properties, which could be applied in material designing and fulfill various application purposes. A few research groups have reported the magnetic property change in RE-substituted $CoFe_2O_4$ but so far no

detailed relationship between the structure and the magnetism has been illustrated[4-7]. The thesis aim is to synthesize well-defined RE-substituted $CoFe_2O_4$ nanoparticles and study the magnetic effects of the incorporation of rare earth elements into the spinel ferrite lattice.

3-3 Experimental

3-3-1 Synthesis of metal acetate precursors

Metal acetate precursors were prepared by reacting acetic acid with metal hydroxide, which at first was prepared via either chloride or nitrate salt and NaOH. In brief, $CoCl_2$ / $FeCl_3$ / $RE(NO_3)_3$ (RE = Nd^{3+} or Ho^{3+}) (20 mmol) was first dissolved in 100 mL of distilled water respectively. Upon the addition of 70 mL of 1.5 M NaOH solution, metal hydroxide solids precipitated out. The solution was stirred for 2 hours. Then the precipitate was collected and washed 3 times with distilled water through centrifugation. Since both $Nd(NO_3)_3$ and $Ho(NO_3)_3$ are strong oxidizing agents, the above procedures making $RE(OH)_3$ should be done under ice bath and Ar atmosphere ensuring the inert environment. The metal hydroxide solids were re-dispersed in 100 mL of glacial acetic acid (99%) and then dried at 70 ^oC for 12 hours. Upon completely

evaporating the liquid, a fine powder of metal acetate precursor was collected. Note that due to the electronic configurations, each metal acetate appeared distinctive color, namely, iron(III) acetate: dark orange, cobalt(II) acetate: brown, neodymium(III) acetate: grey, and holmium(III) acetate: pink.

3-3-2 Synthesis of spinel ferrite nanoparticles

According to stoichiometry, reaction yields, and literature reports, the molecular formulas for as synthesized precursors are as following: $[Fe_3O(OAc)_6(H_2O)_3]OAc$, $Co(OAc)_2{\cdot}4H_2O$, $Nd(OAc)_3{\cdot}4H_2O$, and $Ho(OAc)_3{\cdot}4H_2O$, where OAc^- stands for $CH_3CO_2^-$. $CoRE_xFe_{2-x}O_4$ was synthesized via aminolytic reaction using individual acetate precursors. Based on different substitution amounts, different stoichiometric ratio of metal acetate precursors (with a total metal ion 7.5 mmol) were suspended in a mixture of 10 mL of oleylamine and 40 mL dibenzyl ether. The turbid metal acetate solution was then heated to 140 ^oC and stirred for 1 hour under an Ar-purged reflux system. After all the solids dissolved, the temperature was raised to 240–245 ^oC at ramping rate of 5 ^oC/min. and the reaction solution was agitated for a certain reaction time. The reaction was quenched by simply removing the heating bath. The mixture was transferred into a beaker after the reaction solution cooled down to 40 ^oC. The

nanoparticles were collected by a magnet and washed with ethanol for four times.

3-3-3 Instrumental

Powder X-ray diffraction (XRD) patterns were collected with the Bruker AXS D8 Advance Powder X-Ray Diffractometer with copper Kα source over 15^{o}–85^{o} 2θ range. Particle sizes were determined from the average peak broadening by performing Debye-Scherrer equation analysis with the commercial program TOPAS. Elemental analysis was conducted with inductively coupled plasma mass spectrometry (ICP-MS) and the samples were prepared by digesting particles into nitric acid with a final dilution of 100–200 ppb metal ion in 1% HNO_3. Transmission electron microscopy (TEM) measurements were conducted using JEOL 100CX2 at 100 kV. Samples were prepared by dispersion of particles in hexane (sonication > 30 min.) and spread onto copper grids. Magnetic measurements were performed with Quantum Design MPMS-5S Superconducting QUantum Interference Device (SQUID). Zero-field cooled (ZFC) susceptibility measurements were performed under an applied field of 100 G. Hysteresis measurements were performed at 5 K with applied fields up to 5 T. For the hysteresis measurements, the nanoparticles were mixed with eicosane to prevent physical movements of the nanoparticles.

3-4 Results and discussion

3-4-1 Nd(III) substitution in $CoFe_2O_4$

The aminolytic reaction route described in Chapter 2 opens up a variety of chemical possibilities for production of metal oxide nanoparticles. With the incorporation of neodymium(III) acetate and holmium(III) acetate, the rare earth (RE) metal cations could participate into the spinel ferrite nucleation and growth process through the same releasing mechanism which is initiated from oleylamine nucleophilic attacking metal acetate. Lots of attempts to introduce RE cations into spinel ferrite lattice system using co-precipitation and/or sol-gel methods have been reported[5,8-15]. Since RE nitrates and chlorides are the most commercially available RE element products, an aqueous based synthesis system is adequate for all metal cation sources to dissolve in the same media (without the need of a further step for ion releasing) so that further nucleation and growth could occur. Various RE substituted spinel ferrites have been made by the simple mixing of metal cation salts together under aqueous solution; often with some additives or gel media to control the growth process[5,8,16]. Compared to slower reaction processes, such as thermo decomposition methods, the control over the particle sizes and shapes for co-precipitation and even

sol-gel methods have their limitations. Thus most of the reported "RE substituted spinel ferrites" are in the form of particles with dimensions in micro-meter range. Micelle/reversed micelle methods has been applied to achieve nano-sized RE spinel ferrites and particles with the scale of several tens nanometer could be produced[6].

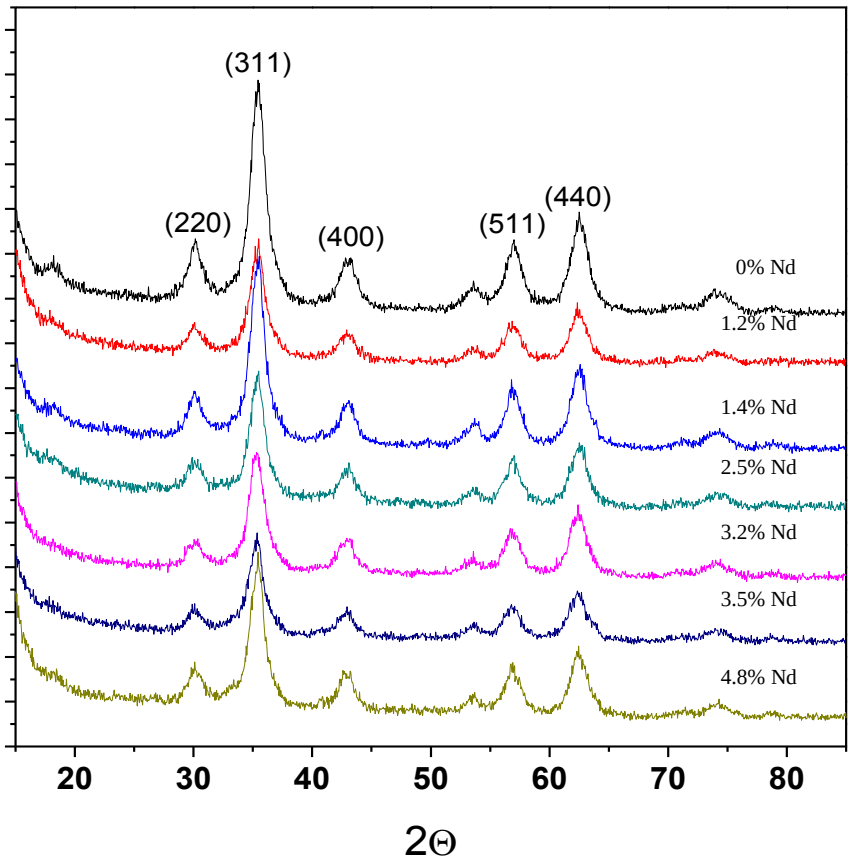

Fig. 3-1 XRD patterns of Nd(III) substituted $CoFe_2O_4$ samples; the percentage is the molar ratio of $Nd^{3+}/(Nd^{3+}+Fe^{3+})$, which measured through ICP-MS (Fe, Co, & Nd elements). Peak broadening

has been analyzed with Debye-Scherrer equation for average particle size.

As shown in Fig. 3-1, only pure spinel ferrite phase could be observed on the XRD patterns and the peak broadening analysis confirmed the narrow average size range 6.8 ± 0.3 nm across different Nd(III) substitution ratios, which have been measured by ICP-MS. Therefore it has been demonstrated that Nd(III) substituted $CoFe_2O_4$ under 10 nm could be synthesized successfully by the aminolytic approach. The aminolytic method could retain the advantage of traditional thermo decomposition method in which the ion sources are released slowly, but at the same time, requires only simple precursor sources, which could be started as simple as a chloride or nitrate salt. Note that the substitution tends to have a roughly 5% upper limit based on the experiment results. Fig. 3-2 shows the representative TEM image of Nd(III) substituted $CoFe_2O_4$ sample and one could obtain the size distribution 7.0 ± 0.8 nm based on a total of > 200 particle counts.

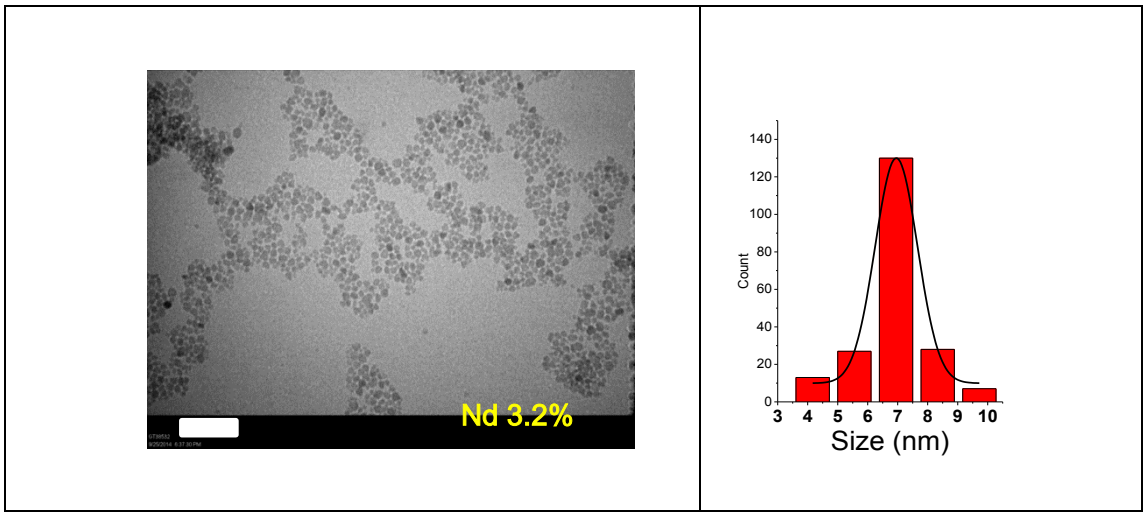

Fig. 3-2 TEM image of Nd(III) substituted $CoFe_2O_4$ with Nd(III) substitution, $Nd^{3+}/(Nd^{3+}+Fe^{3+})$, 3.2%. The scale bar represents 50 nm. Particle size counts for distribution analysis is on the right.

3-4-2 Ho(III) substitution in $CoFe_2O_4$

With the successful substitution of Nd(III), another RE element Ho(III) was introduced to the spinel ferrite lattice to compare the effects on magnetic properties between different 4f electron configurations. As shown in Fig. 3-3, pure spinel ferrite phase could be observed on the XRD patterns and the peak broadening analysis confirmed the average size range 6.7 ± 0.6 nm across different Ho(III) substitution ratios (which were measured by ICP-MS). Note that the substitution amount could

exceed over 5% compared to the Nd(III) case, but a slight hump at $2\theta = 41^{o}$ could be observed for the 8% sample and this could be arisen from the Nd_2O_3 impurities. Fig. 3-4 shows the representative TEM image of Ho(III) substituted $CoFe_2O_4$ sample and one could obtain the size distribution 6.9 $\pm$ 0.8 nm based on a total of > 450 particle counts.

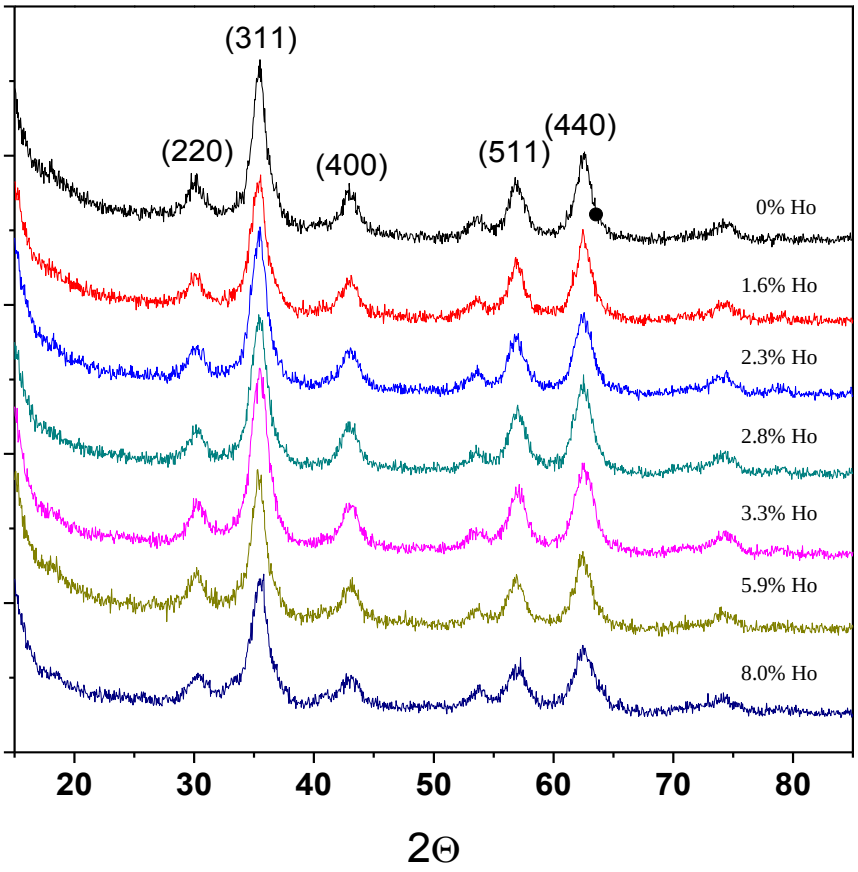

Fig. 3-3 XRD patterns of Ho(III) substituted $CoFe_2O_4$ samples; the percentage is the molar ratio of $Ho^{3+}/(Ho^{3+}+Fe^{3+})$, which measured through ICP-MS (Fe, Co, & Ho elements). Peak broadening has been analyzed with Debye-Scherrer equation for average particle size.

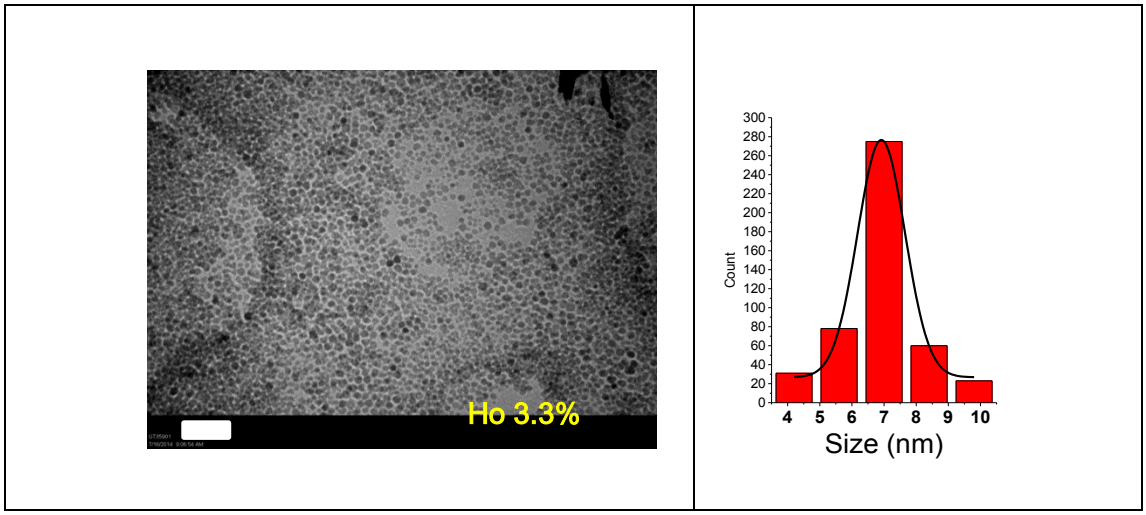

Fig. 3-4 TEM image of Ho(III) substituted $CoFe_2O_4$ with Ho(III) substitution, $Ho^{3+}/(Ho^{3+}+Fe^{3+})$, 3.3%. The scale bar represents 50 nm. Particle size counts for distribution analysis is on the right.

3-4-3 Effects of RE substitution on magnetic properties

The aminolytic method has been shown to possess the advantage of traditional thermo decomposition method in which the ion sources are released slowly, and at the same time, require only simple precursor sources, which could be started as simple as a chloride or nitrate salt. And therefore with the aminolytic synthetic strategy, both Nd(III) and Ho(III) substituted $CoFe_2O_4$ under 10 nm could be synthesized successfully and samples all appeared as single phase, with confirmed chemical

composition and under 10 nm in size with narrow size distribution within ± 9% (or smaller). This is a significant research progress for magnetism studies in RE effects in substituted spinel ferrites since a well-defined nanoparticle system could not only avoid the domain wall issues but also directly correlate magnetic properties with particle sizes and compositions, which both could be controlled precisely from the aminolytic synthesis route. One of the most appealing properties of spinel ferrites for applications is that the mixing of different compositions can change the sum moment, superexchange strength, Neel/ blocking temperature and degree of inversion. The cation occupancy in either the tetrahedral or octahedral sites plays an important role in determining the overall magnetism. Both the Rietveld refinement of the XRD results and literatures have suggested that the RE element would occupy the octahedral sites due to the much larger size compared to that of the transition metal ions. Fig. 3-5 shows the hysteresis curves at 5 K for representative samples to compare exclusively the RE effects. Note that the samples selected to be focused on the magnetic property studies were the ones with RE substitution amount less than 5% in consideration of phase purity. Extracted data is shown in Table 3-1, and both Nd(III) and Ho(III) substitution over Fe(III) have not significantly changed the saturation and remanence magnetization and only 3.2% of Nd(III) increased coercivity slightly (~10%). Considering the electronic configuration of Nd(III) with $4f^3$ and Ho(III) with $4f^{10}$,

their substitution over Fe(III) $3d^5$could theoretically decrease the net magnetic moment and increase the magnitude of the magnetocrystalline energy barrier. But however as the substitution amount has been as low as only ~3%, the large hysteresis loop under low temperature, a signature character of $CoFe_2O_4$ nanoparticles, remains.

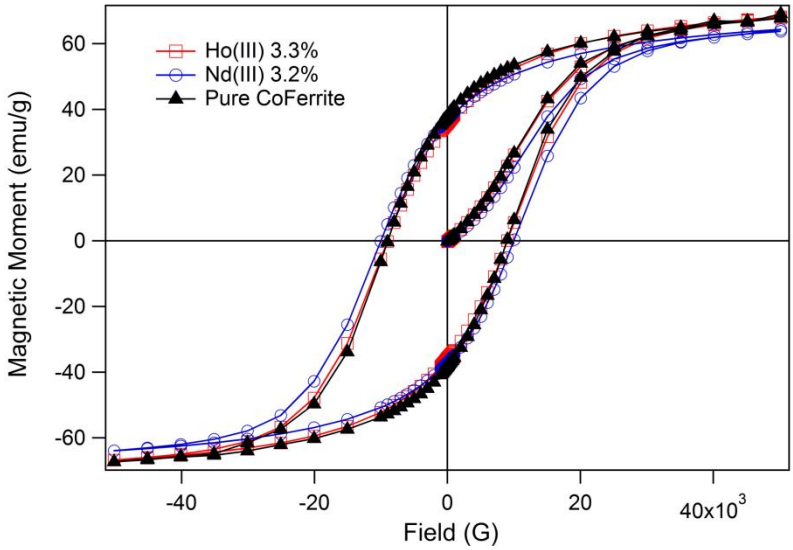

Fig. 3-5 Hysteresis curves at 5 K for representative RE substituted $CoFe_2O_4$ NPs

Table 3-1 Extracted data from the magnetic hysteresis loops in Fig. 3-5; M_S = saturation magnetization and M_R = Remanent magnetization

	M_S (emu/g)	M_R (emu/g)	Coercivity (G)
Pure $CoFe_2O_4$	68.5	38.0	8960
Nd 3.2%	64.0	36.8	10000
Ho 3.3%	68.0	36.0	9000

Temperature dependent susceptibility measurements have been carried out under an external field at 100 G and Fig. 3-6 depicts the plotting results. As the RE substitution amount increased, the blocking temperature shifted towards to the lower temperature end. And as shown in Fig. 3-6, between Nd(III) and Ho(III), Ho(III) could lower the blocking temperature in a greater tendency. The blocking temperature/ Neel temperature (for samples considering as bulk in the particle size) lowering effects of RE element substitution have been reported in literatures[4,5,8-11,16,17]. According to Stoner-Wohlfarth model, a lower blocking temperature indicates a smaller anisotropy energy barrier to overcome. Both magnetocrystalline arising from spin-orbit couplings and surface dis-orderness could contribute the anisotropy and compared with the coercivity results shown in Table 3-1, multiple effects in this Nd(III)/ Ho(III) substituted $CoFe_2O_4$ could simultaneously take place. Note that for the system $CoFe_2O_4$ itself, with a significant angular momentum contribution from Co^{2+}, d^7, the energy barrier for the blocking random fluctuations of magnetic moments is large and thus the blocking temperature (without RE) would start at a higher end intrinsically. It has also been reported that the cation distribution between Co^{2+} and Fe^{3+} in the spinel lattice could change due to different synthesis methods and it is possible that the introduction of RE elements into the octahedral could change the Co^{2+} and Fe^{3+} occupancy and thus the anisotropy could also change. Thus from Fig.

3-5 and 3-6, with a small Nd(III) and Ho(III) substituted amount (~3%) over Fe(III) in $CoFe_2O_4$ nanoparticles, blocking temperature could decreased more than 30 K without much change in the magnetic hysteresis. This could be useful in tuning the working temperature of materials for certain application needs.

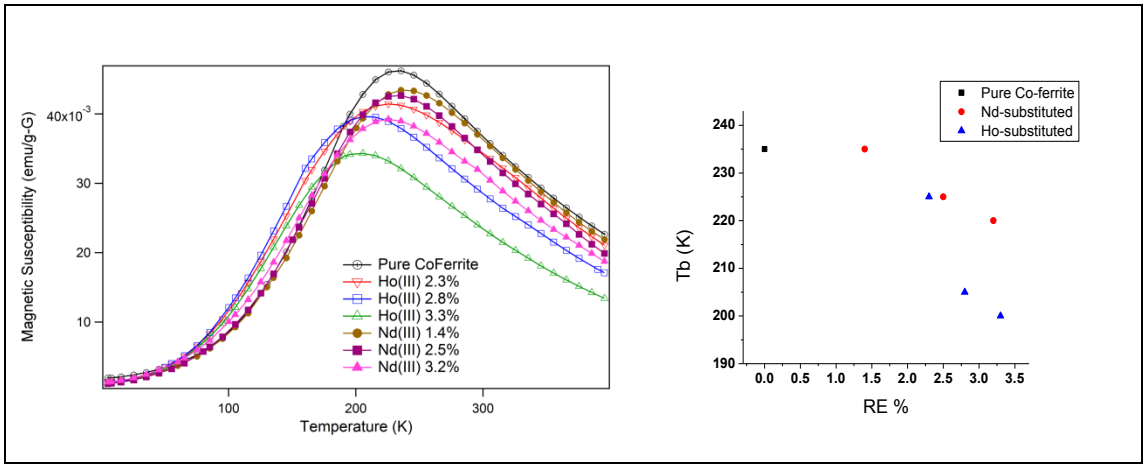

Fig. 3-6 Temperature dependent susceptibility measurements of $CoFe_2O_4$ NPs with different RE(III) substitution amount. The percentage is the molar ratio of $RE^{3+}/(RE^{3+}+Fe^{3+})$

3-5 Conclusions

In summary, $Nd_xCoFe_{2-x}O_4$ and $Ho_xCoFe_{2-x}O_4$ nanoparticles under 10 nm with good size distribution (± less than 10%) have been made successfully by using the aminolytic metal oxide synthesis strategy. The aminolytic method described in Chapter 2 retains the advantage of traditional thermo decomposition method in which the ion sources are released slowly, and at the same time, only simple precursor sources, which could be started as simple as a chloride or nitrate salt, are required. Thus the size scale and distribution could be controlled more precisely in this approach compared to other common methods such as co-precipitation, sol-gel and micelle methods. Magnetic data has indicated that with a small Nd(III) and Ho(III) substituted amount (~3%) over $Fe(III)_{(Oh)}$ in $CoFe_2O_4$ nanoparticles, blocking temperature could decreased more than 30 K without much change in the magnetic hysteresis. This provides useful ideas for tuning the working temperature of ferrite materials for actual applications.

3-6 References

(1) Nguyen, T.-D.; Do, T.-O. *Size- and Shape-Controlled Synthesis of Monodisperse Metal Oxide and Mixed Oxide Nanocrystals*, 2011.

(2) Cushing, B. L.; Kolesnichenko, V. L.; O'Connor, C. J. *Chem. Rev.* **2004**, *104*, 3893.

(3) Roucoux, A.; Schulz, J.; Patin, H. *Chem. Rev.* **2002**, *102*, 3757.

(4) Amiri, S.; Shokrollahi, H. *J. Magn. Magn. Mater.* **2013**, *345*, 18.

(5) Ali, I.; Islam, M. U.; Ishaque, M.; Khan, H. M.; Ashiq, M. N.; Rana, M. U. *J. Magn. Magn. Mater.* **2012**, *324*, 3773.

(6) Kahn, M. L.; Zhang, Z. J. *Appl. Phys. Lett.* **2001**, *78*, 3651.

(7) Cheng, F. X.; Jia, J. T.; Xu, Z. G.; Zhou, B.; Liao, C. S.; Yan, C. H.; Chen, L. Y.; Zhao, H. B. *J. Appl. Phys.* **1999**, *86*, 2727.

(8) Bhongale, S. R.; Ingawale, H. R.; Shinde, T. J.; Vasambekar, P. N. *J. Rare Earths* **2018**, *36*, 390.

(9) Bulai, G.; Diamandescu, L.; Dumitru, I.; Gurlui, S.; Feder, M.; Caltun, O. F. *J. Magn. Magn. Mater.* **2015**, *390*, 123.

(10) Naik, S. R.; Salker, A. V. *J. Mater. Chem.* **2012**, *22*, 2740.

(11) Kumar, P.; Sharma, S. K.; Knobel, M.; Chand, J.; Singh, M. *J. Electroceram.* **2011**, *27*, 51.

(12) Muthuselvam, I. P.; Bhowmik, R. N. *J. Magn. Magn. Mater.* **2010**, *322*, 767.

(13) De Silva, C. R.; Smith, S.; Shim, I.; Pyun, J.; Gutu, T.; Jiao, J.; Zheng, Z. P. *J. Am. Chem. Soc.* **2009**, *131*, 6336.

(14) Bharathi, K. K.; Chelvane, J. A.; Markandeyulu, G. *J. Magn. Magn. Mater.* **2009**, *321*, 3677.

(15) Cheng, F. X.; Liao, C. S.; Kuang, J. F.; Xu, Z. G.; Yan, C. H.; Chen, L. Y.; Zhao, H. B.; Liu, Z. *J. Appl. Phys.* **1999**, *85*, 2782.

(16) Patankar, K. K.; Ghone, D. M.; Mathe, V. L.; Kaushik, S. D. *J. Magn. Magn. Mater.* **2018**, *454*, 71.

(17) Upadhyay, R. V.; Gupta, A.; Sudakar, C.; Rao, K. V.; Parekh, K.; Desai, R.; Mehta, R. V. *J. Appl. Phys.* **2006**, *99*.

CHAPTER 4. FIELD SHIFTS OF FERROMAGNETIC RESONANCE AMONG SPINEL FERRITE NANOPARTICLES WITH DIFFERENT SPIN ORDERS

4-1 Abstract

In this chapter, various spinel ferrite nanoparticles with defined sizes and chemical compositions were made and their ferromagnetic resonance properties were studied with both SQUID and EPR. Among a wide range of spinel ferrites with different transition metal ion centers including Mn(II), Fe(II), Fe(III), Co(II) and Zn(II), a negative correlation between magnetic susceptibility and FMR field was discovered and this provides a shortcut to foresee the resonance field with one single measurable susceptibility without further structural information such as degree of inversion and magnetic structures.

4-2 Introduction

Magnetic ferrite nanoparticle is a potential material in a number of applications including data storage, signal transmission, electromagnetic interference, contrast enhancement in MRI, and hyperthermia treatment[1-4]. Designing of such applications requires the fine-tuning of magnetic properties by chemical composition and dimensional control, and in order to manipulate the specific material performance, the fundamental relationship between the microstructure and magnetic properties still needs further illustration[4-8]. Ferrite materials often have a strong coupling to electromagnetic signals due to high permeability and permittivity and thus could be used in a variety of microwave devices, e.g. from military shielding to wireless communication signal enhancement. Microwave technology has been expanding towards to higher frequencies and bandwidths, and therefore how to design the corresponding microwave ferrites for devices has become a topic of high interests[1,8-13]. The magnetic superexchange of cations in ferrite sublattices strongly depends on bonding lengths and angles, which could be simply tuned by structure modifications and chemical substitutions. Numerous studies have focused on how structural and chemical modifications affect ferrite magnetism, yet the fundamental relationship between magnetic structure and ferromagnetic resonance[6,7,10,14-16], which is the actual property being utilized in microwave applications, is still obscure. Studies have

demonstrated how different ferrites could have different microwave absorption behaviors, but most of the findings and conclusions are empirical[2,5,6,8,14,16-18].

Spinel ferrites are the most popular microwave ferrites and have been used in 3-30 GHz band[8,10,11,19]. Mixed spinel ferrites have been commonly used in various microwave applications. For example, MnZn ferrites ($Zn_{1-x}Mn_xFe_2O_4$) have been used in microwave applications below 5 MHz and NiZn ferrites ($Zn_{1-x}Ni_xFe_2O_4$) have been demonstrated as the common materials for inductors at 70 MHz to 3 GHz[5,10,18]. In this research, a series of spinel ferrite nanoparticles were studied thoroughly in order to shed some light on the theoretical correlations between magnetic properties and microwave absorption behaviors.

4-3 Experimental

4-3-1 Synthesis

Spinel ferrite (MFe_2O_4, M = Mn(II), Co(II) and Zn(II)) nanoparticles were synthesized via aminolytic reaction as described in previous chapters. The metal acetate precursor (7.5 mmol) with stoichiometric ratio of M(II) to Fe(III) = 1:2 were suspended in a mixture of 10 mL of oleylamine and 40 mL dibenzyl ether. Particles

with more than two metal ion centers, i.e. mixed spinel ferrites/ RE substituted spinel ferrites, were made from appropriate mixture of metal acetates. The turbid metal acetate solution was heated to 140 ^{o}C and stirred for 1 hour under an Ar-purged reflux system. After all the solids dissolved, the temperature was raised to 240–255 ^{o}C at a ramping rate of 5 ^{o}C/min. and the reaction solution was agitated for 1–2 hours. The reaction was quenched by simply removing the heating bath. The mixture was transferred into a beaker after the reaction solution cooled down to 40 ^{o}C. The nanoparticles were collected by a magnet and washed with ethanol for four times.

4-3-2 Instrumentation

Powder X-ray diffraction (XRD) patterns were collected with the Bruker AXS D8 Advance Powder X-Ray Diffractometer with copper Kα source over 15^{o}–85^{o} 2θ range. Particle sizes were determined from the average peak broadening by performing Debye-Scherrer equation analysis with the commercial program TOPAS. Elemental analysis was conducted with inductively coupled plasma mass spectrometry (ICP-MS) and the samples were prepared by digesting particles into nitric acid with a final dilution of 100–200 ppb metal ion in 1% HNO_3. Magnetic measurements were performed with Quantum Design MPMS-5S Superconducting

QUantum Interference Device (SQUID). Zero-field cooled (ZFC) susceptibility measurements were performed under an applied field of 100 G. Ferromagnetic resonance absorption profiles were measured with Bruker EMX spectrometer operating at X-band frequency. The spectra were recorded under room temperature (300 K) and with ν = 9.88 GHz, center field = 5125.0 G, and sweeping width = 9750.0 G. Samples were prepared by suspending nanoparticle powders into KCl with 1–10 % (wt./ wt.) depending on Co(II) concentration. With Co(II) amount increases, it is required to increase the weight percentage to ensure EPR spectrum with clear resolutions.

4-4 Results and discussion

As shown in Fig. 4-1, spinel ferrite nanoparticles with different chemical compositions were made and their XRD patterns indicate single cubic spinel phase (magnetite JCPDS: 19-0629). The chemical compositions were analyzed by ICP-MS and the corresponding chemical formulas are listed. Fig. 4-2 shows temperature dependent magnetic susceptibility measurements at 100 G. Susceptibility (χ) indicates the degree of magnetization of a material under an applied magnetic field, and strongly depends on the material structures, both atomic and magnetic. With positive

susceptibilities, all spinel ferrite nanoparticles listed in this paper are paramagnetic, more specifically, superparamagnetic, due to much larger susceptibilities than that of paramagnets. Spinel ferrite nanoparticles are single-domain, and thus the magnetization for each particle is the sum of all the individual magnetic moments carried by the metal cations. Blocking temperature (T_B) and maximum susceptibility vary with chemical composition and thus each type of spinel ferrite nanoparticle has its own characteristic induced magnetization profile. According to the Stoner-Wohlfarth model[3], high blocking temperature indicates large magnetic anisotropy energy (E_A) due to a large volume and anisotropy energy constant: $E_A = K V \sin^2\theta$, where K is the anisotropy energy constant, V is the volume of the nanoparticle, and θ is the angle between the particle easy axis and the applied field direction. With a significant angular momentum contribution from $Co^{2+}_{(Oh)}$, in which the electron configuration is $t_{2g}^5 e_g^2$, the energy barrier for the blocking random fluctuations of magnetic moments is large and this results in a high blocking temperature at 300 K. Both Mn^{2+} with d^5 and Zn^{2+} with d^{10} exhibit no anisotropy contribution and thus the blocking temperatures of $MnFe_2O_4$ and $ZnFe_2O_4$ are relatively smaller (< 100 K). $Fe^{2+}_{(Oh)}$ in Fe_3O_4 has the electron configuration $t_{2g}^4 e_g^2$ and the moderate angular momentum causes a blocking temperature within the medium range (~150 K). For more complicated mixed spinel ferrites containing

multiple cation species, the blocking temperature follows the similar trend: $Co_{0.1}Mn_{0.9}Fe_2O_4$ has a higher blocking temperature than that of $MnFe_2O_4$ with similar size, and $Zn_{0.2}Mn_{0.8}Fe_2O_4$ has a blocking temperature in between the range of the T_B of pure $MnFe_2O_4$ and $ZnFe_2O_4$ with similar sizes. The introduction of rare-earth cations into pure $MnFe_2O_4$ (Gd^{3+}, f^7) and $CoFe_2O_4$ (Nd^{3+}, f^3 and Ho^{3+}, f^{10}) has lowered T_B which suggests that the anisotropy has been decreased and/or the inversion degree has been changed. Similar results can be found in the literature and it is worth noting that the degree of inversion of spinel ferrites could be easier to tune compared to that of their bulk counterparts.

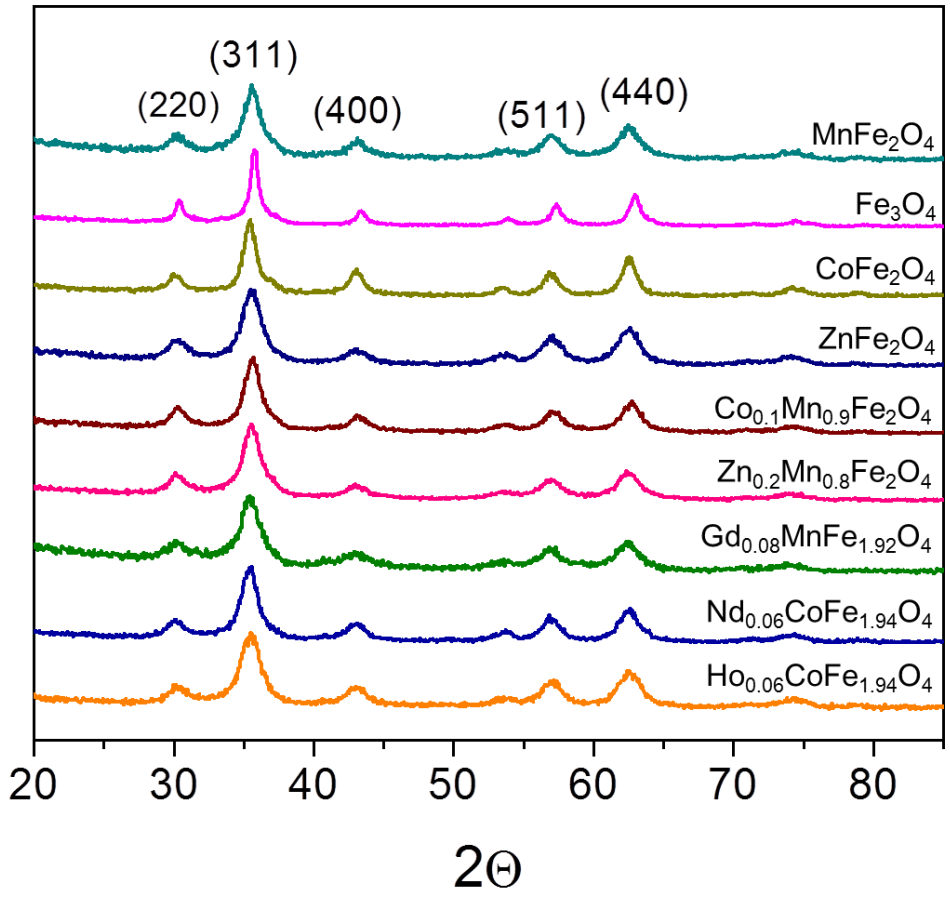

Fig. 4-1 XRD patterns of various nanoparticle samples, indicating pure spinel ferrite phase was made successfully with different chemical compositions. Bragg peak broadening data and Scherrer equation were used to calculate the average size of each sample, and the results are listed in Table 1. Chemical composition of each sample was confirmed with ICP-MS and converted into its chemical formula.

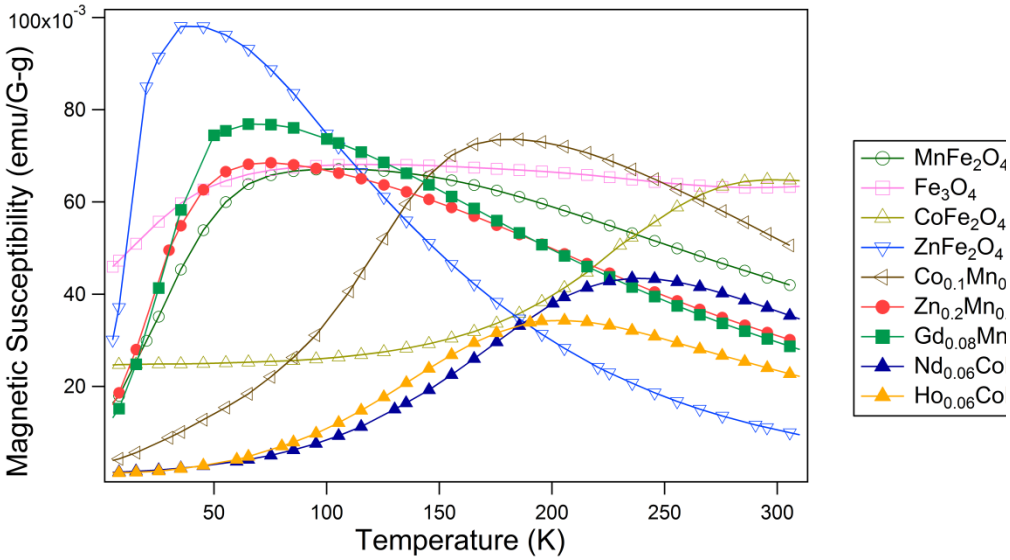

Fig. 4-2 Temperature dependent susceptibility of each spinel ferrite nanoparticle samples; zero-field cooled (ZFC) susceptibility measurements were conducted under an applied field of 100 G with temperature range from 5 – 310 K.

Ferromagnetic resonance (FMR) arises from the procession of the material magnetization in an external magnetic field and has been utilized to probe the dynamical magnetic properties. From the magnetic resonance field and line width, one could obtain information such as magnetic dipolar interaction, superexchange interaction and spin-spin relaxation[1,2,10]. Fig. 4-3 demonstrates the FMR absorption

profiles of various spinel ferrites under ν = 9.88 GHz. Extracted values (resonance field, *H*, and line width, *ΔH*) along with structural and magnetic information are listed in Table 4-1. Each type of spinel ferrite has its own unique FMR absorption profile. While the resonance fields for all of the spinel ferrites are ranging within 2700-3500 G, their line widths vary from 500 G (pure $ZnFe_2O_4$) to >3000 G (spinel ferrites containing Co^{2+}). This is consistent with previous studies in literature[2,5,6,14,17,18,20], and indicates that the variation of compositions could directly tune the microwave absorption behaviors in order to achieve for a certain target application. MnZn ferrites nanoparticles have already been studied intensively and it has been concluded that the more Mn^{2+} to Zn^{2+} within the lattice, the resonance frequency tends to shift towards to a lower field, suggesting the increased crystalline anisotropy[5]. The strong spin-orbit coupling interaction of Co^{2+} contributes much in crystalline anisotropy of mixed spinel ferrites and thus has been reported to lower the FMR field[8,14]. Although FMR resonance field is mainly affected by anisotropy energy, recent studies have showed that thermal fluctuation must be considered, especially in nanoparticle systems, since the magnetism in nanoparticles is strongly dependent on temperature[20-22]. In order to understand the relationship between material composition and its FMR behavior, complicated physical models have been built; despite the fact that in real-world applications, empirical results or actual measurements are still required due to the

difficulty to “predict” the FMR profiles. To the best of our knowledge, no simple measurable material physical property, which could be considered solely in reasoning FMR, has been reported[8,18,20-22].

It is worthy to note that the temperature dependent magnetic susceptibility actually reflects both the effects of magnetic anisotropy and thermal fluctuation directly. With careful examination of the FMR absorption profiles and the magnetic susceptibility measurements, values of H in various spinel ferrites were plotted versus χ under FMR experimental temperature, i.e. room temperature at 300 K, as in Fig. 4-4. Despite the different spin orders among the representative sample series, a negative correlation could be found in the H versus χ plot. Qualitatively, a trend could be addressed among these samples: with a larger magnetic susceptibility, a lower applied field is required to reach the resonance frequency $\nu = 9.88$ GHz.

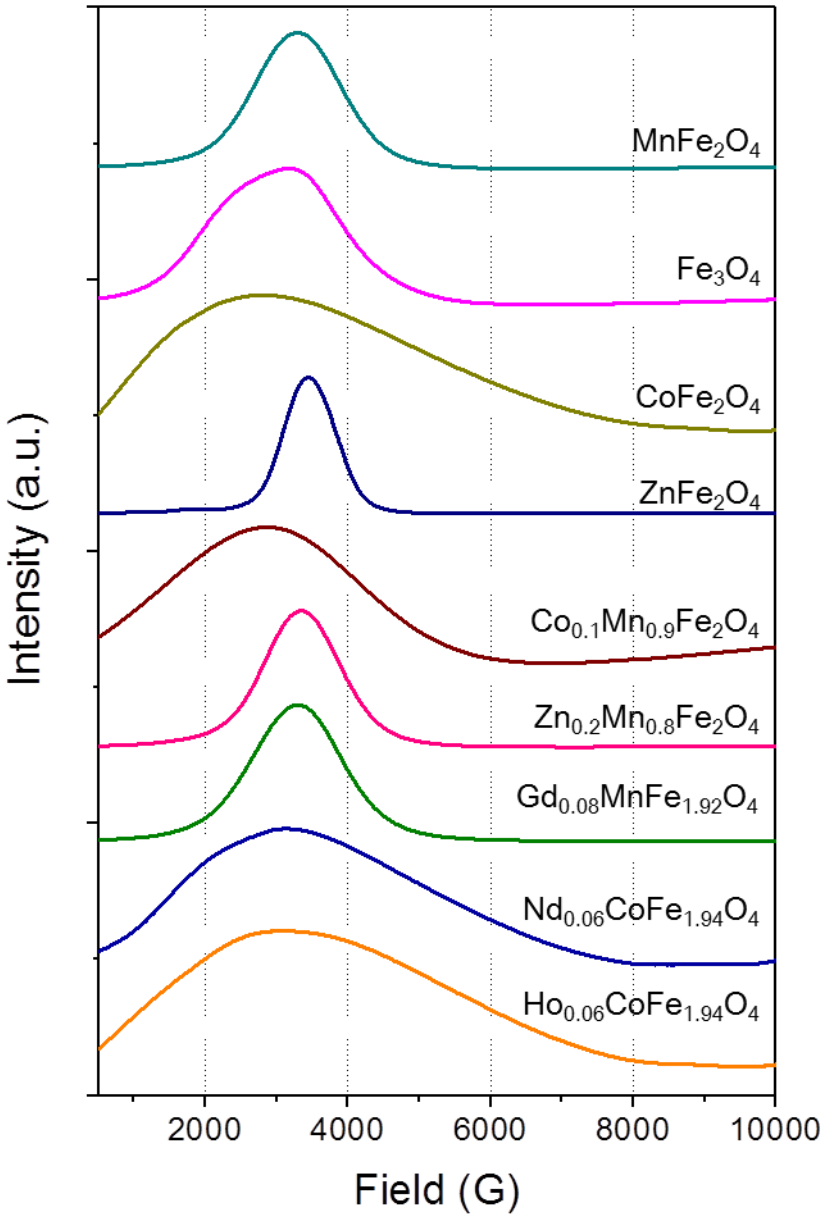

Fig. 4-3 Ferromagnetic resonance (FMR) absorption profiles of various spinel ferrite nanoparticles under ν = 9.88 GHz at room temperature 300 K. Center field = 5125.0 G and sweeping width = 9750.0 G

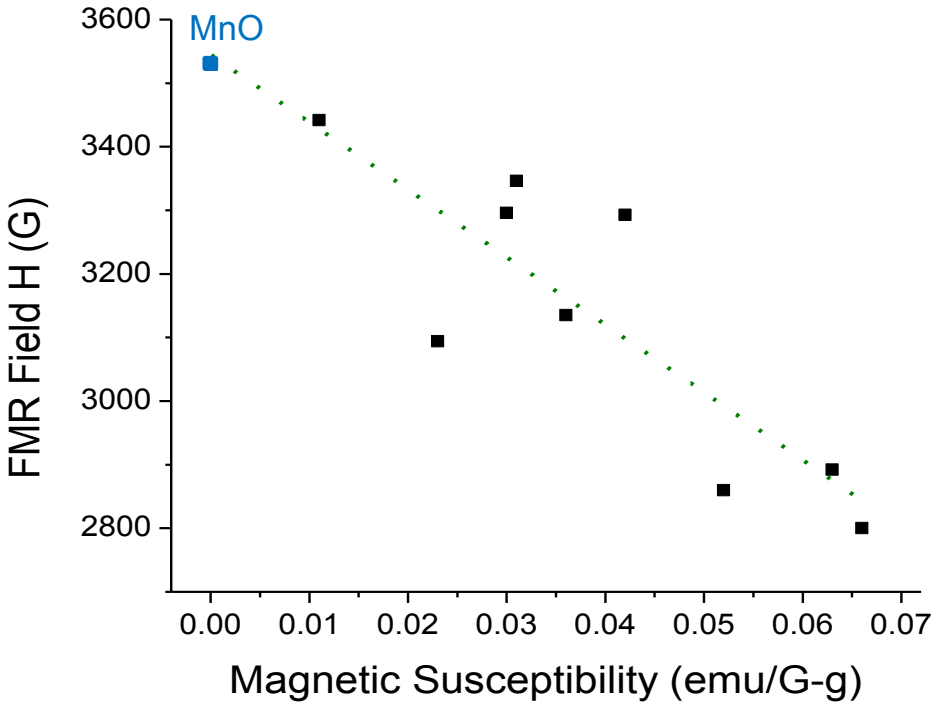

Fig. 4-4 FMR field with ν = 9.88 GHz (*H*) versus magnetic susceptibility (χ); all black data points were extracted from spinel ferrite samples and data from MnO nanoparticles is labeled.

With a higher magnetic susceptibility, the degree of magnetization would be larger in response to an applied magnetic field, and thus causes a larger energy difference arising from the magnetic dipolar coupling. This results in a smaller applied field in FMR measurements to achieve the fixed resonance frequency. Since both *H* and χ are affected by similar physical properties, their negative correlation relationship provides a simple insight in designing a certain microwave material for applications. This correlation allows one to bypass the complicated considerations of

detailed atomic & magnetic structures, which often need unique techniques such as neutron diffraction. Though currently this correlation has only been verified in spinel ferrite system, a trial case of antiferromagnetic MnO has been conducted successfully. The room temperature χ was found 8.0E-5 emu/G-g and its *H* fell at the further end of the spinel ferrite trend at 3529 G as shown in Fig. 4-4, suggesting the potential application of a wide range of microwave materials. A more quantitative study is undergoing with consideration of FMR peak broadening effect, and a variety of mixed spinel ferrites are under investigation to validate a more precise correlation model.

Table 4-1 Sample list with composition, size, extracted magnetic & FMR data; MnO is the only non-spinel ferrite sample and is listed here for comparison.

Sample	Size (nm)	T_B (K)	χ@RT (emu/G-g)	*H* (G)	*ΔH* (G)
$MnFe_2O_4$	5.6	100	0.042	3293	1145
Fe_3O_4	12	125	0.063	2892	1853
$CoFe_2O_4$	9.0	300	0.064	2598	3800
$ZnFe_2O_4$	6.0	50	0.011	3442	729
$Co_{0.1}Mn_{0.9}Fe_2O_4$	7.3	180	0.053	2860	2713
$Zn_{0.2}Mn_{0.8}Fe_2O_4$	6.2	75	0.028	3347	991
$Gd_{0.08}MnFe_{1.92}O_4$	6.6	70	0.029	3296	1195
$Nd_{0.06}CoFe_{1.94}O_4$	6.2	240	0.035	2952	3044
$Ho_{0.06}CoFe_{1.94}O_4$	5.9	200	0.023	3171	4273
MnO*	28	30	8.0E-5	3529	993

4-5 Conclusions

In conclusion, a series of spinel ferrite nanoparticles with well-defined sizes and compositions have been used for magnetic studies to illustrate FMR phenomenon, which has been applied in microwave devices. Temperature dependent magnetic susceptibility measurements showed that under an external field (100 G), each type of particles has very unique magnetization amplitude change over the temperature ranging 5-310 K, resulting signature blocking temperature. T_B results are consistent with particle size and cation composition. FMR analysis was carried with a standard electron paramagnetic resonance (EPR) setup under ν = 9.88 GHz. Different spinel ferrites possess their own characteristic absorption profiles, and their specific resonance field, *H*, and resonance field line width, ΔH, have been extracted. A simple correlation shows that a spinel ferrite nanoparticle sample with a larger magnetic susceptibility, a lower applied field is required to reach the FMR frequency. This negative correlation trend has provided a shortcut to foresee *H* with one single measurable χ without further structural information such as degree of inversion and magnetic structures. Other than spinel ferrites series, the MnO nanoparticle sample has also been demonstrated in consistent with this *H*-χ trend. Research regarding to ΔH is undergoing for the vindication of a more qualitative model which could be applied directly in designing microwave ferrites for specific needs such as radars,

satellites and different portable communication devices.

4-6 References

(1) Nan, C. W.; Bichurin, M. I.; Dong, S. X.; Viehland, D.; Srinivasan, G. *J. Appl. Phys.* **2008**, *103*.

(2) Pardavi-Horvath, M. *J. Magn. Magn. Mater.* **2000**, *215*, 171.

(3) Moumen, N.; Bonville, P.; Pileni, M. P. *J. Phys. Chem.* **1996**, *100*, 14410.

(4) Alivisatos, A. P. *Science* **1996**, *271*, 933.

(5) Thota, S.; Kashyap, S. C.; Sharma, S. K.; Reddy, V. R. *J. Phys. Chem. Solids* **2016**, *91*, 136.

(6) Yan, Q. Y.; Gambino, R. J.; Sampath, S.; Huang, Q. *J. Appl. Phys.* **2005**, *97*.

(7) Lyons, D. H.; Kaplan, T. A.; Dwight, K.; Menyuk, N. *Phys. Rev. B* **2005**, *72*.

(8) Yang, X.; Zhou, Z.; Nan, T.; Gao, Y.; Yang, G. M.; Liu, M.; Sun, N. X. *J. Mater. Chem. C* **2016**, *4*, 234.

(9) Dimri, M. C.; Kashyap, S. C.; Dube, D. C. *Phys. Status Solidi A-Appl. Mat.* **2010**, *207*, 396.

(10) Harris, V. G.; Geiler, A.; Chen, Y. J.; Yoon, S. D.; Wu, M. Z.; Yang, A.; Chen, Z. H.; He, P.; Parimi, P. V.; Zuo, X.; Patton, C. E.; Abe, M.; Acher, O.; Vittoria, C. *J. Magn. Magn. Mater.* **2009**, *321*, 2035.

(11) Liu, M.; Howe, B. M.; Grazulis, L.; Mahalingam, K.; Nan, T. X.; Sun, N. X.; Brown, G. J. *Adv. Mater.* **2013**, *25*, 4886.

(12) Xing, X.; Lou, J.; Yang, G. M.; Obi, O.; Driscoll, C.; Sun, N. X. *Appl. Phys. Lett.* **2009**, *95*.

(13) Tatarenko, A. S.; Gheevarughese, V.; Srinivasan, G. *Electron. Lett.* **2006**, *42*, 540.

(14) Kumar, A.; Yadav, N.; Rana, D. S.; Kumar, P.; Arora, M.; Pant, R. P. *J. Magn. Magn. Mater.* **2015**, *394*, 379.

(15) Carta, D.; Casula, M. F.; Falqui, A.; Loche, D.; Mountjoy, G.; Sangregorio, C.; Corrias, A. *J. Phys. Chem. C* **2009**, *113*, 8606.

(16) Tomiyasu, K.; Fukunaga, J.; Suzuki, H. *Phys. Rev. B* **2004**, *70*.

(17) Angadi, V. J.; Choudhury, L.; Sadhana, K.; Liu, H. L.; Sandhya, R.; Matteppanavar, S.; Rudraswamy, B.; Pattar, V.; Anavekar, R. V.; Praveena, K. *J. Magn. Magn. Mater.* **2017**, *424*, 1.

(18) Chao, L.; Sharma, A.; Afsar, M. N.; Obi, O.; Zhou, Z. Y.; Sun, N. A. *IEEE Trans. Magn.* **2012**, *48*, 4085.

(19) Yang, G. M.; Xing, X.; Daigle, A.; Liu, M.; Obi, O.; Stoute, S.; Naishadham, K.; Sun, N. X. *IEEE Trans. Antennas Propag.* **2009**, *57*, 2190.

(20) De Biasi, E.; Lima, E.; Ramos, C. A.; Butera, A.; Zysler, R. D. *J. Magn. Magn. Mater.* **2013**, *326*, 138.

(21) De Biasi, E.; Zysler, R. D.; Ramos, C. A.; Knobel, M. *J. Magn. Magn. Mater.* **2008**, *320*, E312.

(22) Trunova, A. V.; Lindner, J.; Meckenstock, R.; Spasova, M.; Farle, M.; Ciuculescu, D.; Amiens, C.; Chaudret, B.; Respaud, M. *J. Magn. Magn. Mater.* **2009**, *321*, 3502.

CHAPTER 5. FERROMAGNETIC STUDIES OF Zn(II) & Co(II) SUBSTITUTED MANGANESE FERRITE NANOPARTICLES

5-1 Abstract

In this work, manganese ferrite based nanoparticles were made using aminolytic method and the systematic control over size and compositions was carried out to further study their magnetic properties and FMR behaviors. Three sets of particles, namely, (1) $MnFe_2O_4$ with different sizes, (2) Mn-Zn ferrite $Mn_{1-x}Zn_xFe_2O_4$ with x = 0–0.5 (~6 nm), and (3) Mn-Co ferrite $Mn_{1-x}Co_xFe_2O_4$ with x = 0–0.5 (~7 nm), were synthesized successfully with the characterizations with XRD and ICP-MS. Temperature susceptibility measurements were conducted under 100 G from 5 to 310 K and FMR spectra were performed under room temperature (300 K) and with ν = 9.88 GHz. Results have revealed the close relationship between size/ composition and FMR absorption through magnetic correlations. This chapter also demonstrates how one could tune FMR absorption profile (both H and ΔH) of the material through synthesis controls.

5-2 Introduction

Soft ferrite materials have been used widely in various microwave components such as circulators, isolators, phase shifters, and frequency limiters for signal processing applications including radar detection, communication devices and certain instrumentations[1-5]. Spinel ferrites have been the most frequently used microwave ferrites and can be applied in 3–30 GHz band[3,5]. Within the spinel ferrite lattice, the magnetic cations form magnetic sublattices and the superexchange interaction between cations results in magnetic properties such as net magnetization, magnetic susceptibility and Neel point. Mixed ferrites have been widely studied since the substitution of different metal cation centers could tune the strength and type of the superexchange interaction. Numerous studies have focused on how structural and chemical modifications affect ferrite magnetism and researchers have demonstrated how different ferrites could have different microwave absorption behaviors[1,3,5-16]. For example, MnZn ferrites ($Zn_{1-x}Mn_xFe_2O_4$) have been used in microwave applications below 5 MHz and NiZn ferrites ($Zn_{1-x}Ni_xFe_2O_4$) have been demonstrated as the common materials for inductors at 70 MHz to 3 GHz[2,3,15]. Plenty of studies focusing on applications with empirical findings have been reported but yet most of the results are scattered among various ferrites and the fundamental relationship between magnetic structure and ferromagnetic resonance is still lacking[2,10,12,17-22].

Manganese ferrite materials have been used as microwave ferrites and according to Chapter 4, $MnFe_2O_4$ nanoparticles appeared great responses under EPR measurements and their absorption field and line width are both in the moderate range which could be tuned towards to different magnitude potentially. The metal centers in manganese spinel ferrite lattice are Mn(II) and Fe(III) which are both d^5 configuration contributing no magnetocrystalline anisotropy due to the lack of spin-orbit coupling. Thus in this chapter, the $MnFe_2O_4$ spinel ferrite nanoparticle was chosen to be the basic system to illustrate the magnetic correlations and FMR relations. Three sets of spinel ferrite nanoparticles, namely, (1) $MnFe_2O_4$ with the size ranging from 3–9 nm, (2) Mn-Zn ferrite ($Mn_{1-x}Zn_xFe_2O_4$, x = 0–0.5) with average size ~6 nm, and (3) Mn-Co ferrite ($Mn_{1-x}Co_xFe_2O_4$, x = 0–0.5) with average size ~7 nm, were made to study how the size and composition affect the FMR absorption behavior. Zn(II) is a nonmagnetic component (d^{10}) and Co(II) (d^7) has been known for contributing strong magnetocrystalline anisotropy. With the systematically synthesis of these $MnFe_2O_4$ based particles, the size and composition dependent magnetic properties and FMR have been studied. This work has also demonstrated the detailed relationships between material structures and magnetic properties and could further provide ways in designing microwave ferrites in numerous application devices.

5-3 Experimental

5-3-1 Synthesis

Synthesis of metal acetate precursors

Metal acetate precursors were prepared by reacting metal hydroxide with acetic acid. In brief, three sets of M(II)-Fe(III) acetate complex precursors, where M(II) = Mn(II), Zn(II) and Co(II), were prepared for further synthesis of mixed spinel ferrite nanoparticles. MCl_2 (5 mmol) and $FeCl_3$ (10 mmol) were first dissolved in 100 mL of distilled water. Upon the addition of 60 mL of 1.5 M NaOH solution (or > 80 mmol of NaOH in total), metal hydroxide solids would precipitate out. The solution was stirred for 2 hours and then the precipitate was collected and washed 4 times with distilled water through centrifugation. The metal hydroxide solids were re-dispersed in 200 mL of glacial acetic acid (99%) and then dried at 70 ^{o}C for 12 hours. Upon completely evaporating the liquid, a fine powder with stoichiometric ratio of 1:2 mixture M(II) acetate-Fe(III) acetate was collected.

Synthesis of spinel ferrite nanoparticles

Three sets of spinel ferrite nanoparticles, namely, (1) $MnFe_2O_4$ with the size ranging from 3–9 nm, (2) Mn-Zn ferrite ($Mn_{1-x}Zn_xFe_2O_4$, x = 0–0.5) with average size 6.3 ± 0.3 nm, and (3) Mn-Co ferrite ($Mn_{1-x}Co_xFe_2O_4$, x = 0–0.5) with average size 7.0

± 0.5 nm, were synthesized via aminolytic reaction. For the set (1) $MnFe_2O_4$ with the size ranging from 3–9 nm, Mn(II)-Fe(III) acetate complex precursor (2 g/ batch) was suspended in a mixture of 10 mL of oleylamine and 40 mL dibenzyl ether. The solution was heated to 140 ^oC and stirred for 1 hour under an Ar-purged reflux system. After all the solids dissolved, the temperature was raised to 250 ^oC at a ramping rate ranging from 0.92 to 5.5 ^oC/min. to vary the average size and the reaction solution was agitated for another 1 hour. The reaction was quenched by simply removing the heating bath. The mixture was transferred into a beaker after the reaction solution cooled down to 40 ^oC. The nanoparticles were collected by a magnet and washed with ethanol for four times. Similar protocols were followed to make (2) Mn-Zn ferrite ($Mn_{1-x}Zn_xFe_2O_4$, x = 0–0.5) with average size 6.3 ± 0.3 nm, yet the precursor was changed to the mix of Mn(II)-Fe(III) acetate and Zn(II)-Fe(III) acetate with different ratios and the reaction temperature ramping rate was set ~2 ^oC/min. to control the particle size at ~6 nm. For (3) Mn-Co ferrite ($Mn_{1-x}Co_xFe_2O_4$, x = 0–0.5) with average size 7.0 ± 0.5 nm, the precursor was the mix of Mn(II)-Fe(III) acetate and Co(II)-Fe(III) acetate with different ratios and the reaction temperature ramping rate was set to 1–5 ^oC/min. depending on the Co(II) percentage which will be addressed in the discussion section.

5-3-2 Instrumentation

Powder X-ray diffraction (XRD) patterns were collected with the Bruker AXS D8 Advance Powder X-Ray Diffractometer with copper Kα source over 15^{o}–85^{o} 2θ range. Particle sizes were determined from the average peak broadening by performing Debye-Scherrer equation analysis with the commercial program TOPAS. Elemental analysis was conducted with inductively coupled plasma mass spectrometry (ICP-MS) and the samples were prepared by digesting particles into nitric acid with a final dilution of 100–200 ppb metal ion in 1% HNO_3. Magnetic measurements were performed with Quantum Design MPMS-5S Superconducting QUantum Interference Device (SQUID). Zero-field cooled (ZFC) susceptibility measurements were performed under an applied field of 100 G. Ferromagnetic resonance absorption profiles were measured with Bruker EMX spectrometer operating at X-band frequency. The spectra were recorded under room temperature (300 K) and with ν = 9.88 GHz, center field = 5125.0 G, and sweeping width = 9750.0 G. Samples were prepared by suspending nanoparticle powders into KCl with 1–10 % (wt./ wt.) dependent on Co(II) concentration. With Co(II) amount increases, it is required to increase the weight percentage to ensure EPR spectrum with clear resolutions.

5-4 Results and discussion

5-4-1 Pure $MnFe_2O_4$ with different sizes

$MnFe_2O_4$ nanoparticles with size ranging from 3–9 nm were made by controlling the temperature ramping rate through the aminolytic method described in both Chapter 2 and the synthesis section. Fig. 5-1 shows the XRD patterns of the resulting samples and all of them appeared single spinel ferrite phase (magnetite JCPDS: 19-0629). The average sizes were analyzed through peak broadening fittings with the Scherrer equation. As demonstrated in Chapter 2, the reaction time and temperature in aminolytic method can tune particle sizes in a > 10 nm range, but it sometimes also produces metal oxide impurities when conditions meet. While synthesizing $MnFe_2O_4$ nanoparticles, it is important to use the mixed acetate, Mn(II)-Fe(II) acetate, and keep the reaction temperature under 250 ^oC to prevent the presence of MnO impurity. Thus in this case, the ramping rate would be the key parameter to adjust the particle size. With a faster ramping rate, more nucleation events occurred at once so that more seeds could form. And under the condition of fixed amount of metal ions, more nucleation centers would result in smaller particles. Note that the ramping rate range here was about 1–5 ^oC/ min. and that corresponds to size 3–9 nm. This should be applied as a reference, but not completely duplicated, for other similar aminolytic synthesis approaches.

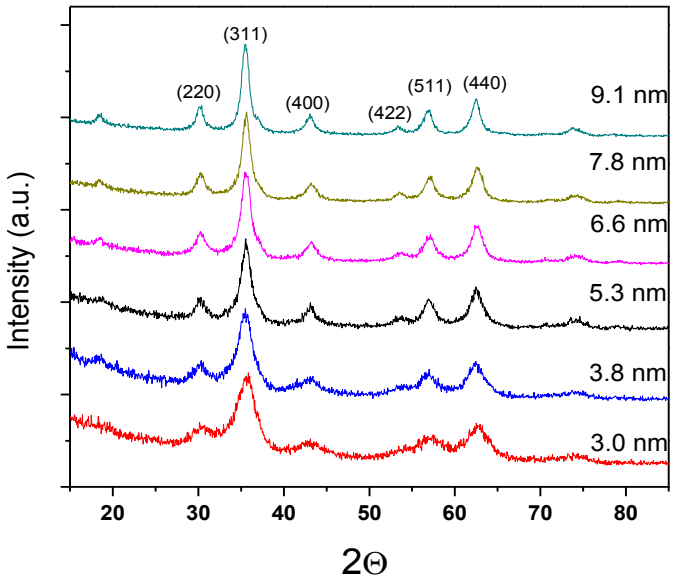

Fig. 5-1 XRD patterns of $MnFe_2O_4$ NPs with different sizes controlled by the temperature ramping rate in aminolytic synthesis method

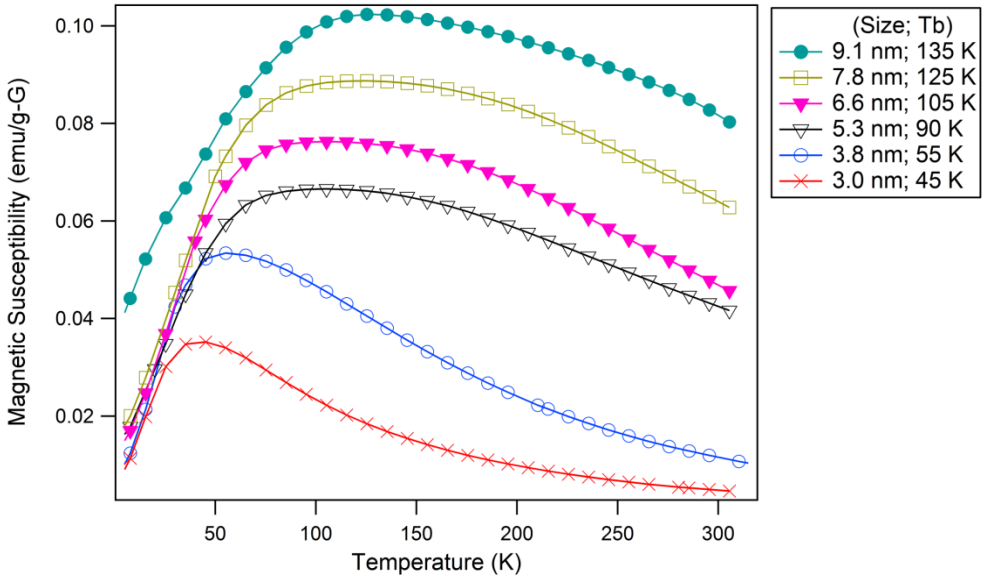

Fig. 5-2 Temperature dependent susceptibility measurements for $MnFe_2O_4$ NPs with different sizes under 100 G; room temperature susceptibilities were extracted in Table 5-1

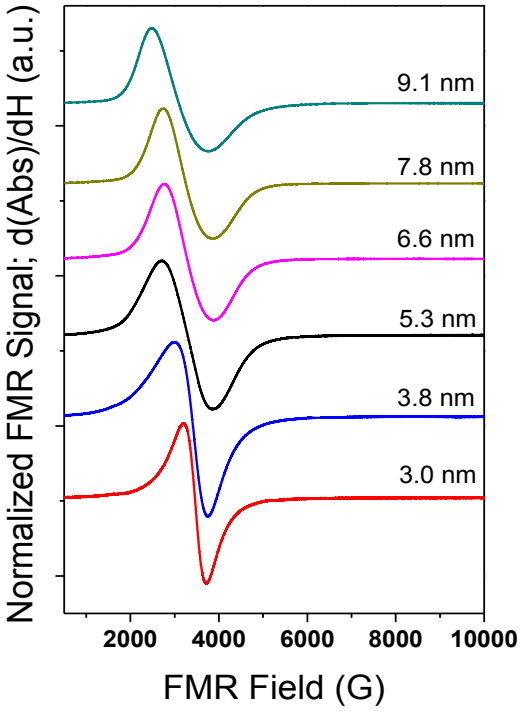

Fig. 5-3 Ferromagnetic resonance (FMR) absorption profiles of $MnFe_2O_4$ NPs with different sizes under ν = 9.88 GHz at room temperature 300 K. Center field = 5125.0 G and sweeping width = 9750.0 G

Temperature dependent susceptibility measurements were shown in Fig. 5-2 and the blocking temperature increases with the increase of the particle sizes. The result is as predicted by the Stoner-Wohlfarth model: larger nanoparticles have greater E_A and larger E_A results in a higher blocking temperature, which represents the threshold at which thermal activation is strong enough to overcome E_A. The susceptibilities at

room temperature (300 K) were recorded in Table 5-1 to further correlate with the FMR fields. The FMR absorption profiles were shown in Fig. 5-3 with first derivative form. All $MnFe_2O_4$ samples revealed similar absorption profiles with only the resonance field shifts which could be predicted through the magnetic susceptibility measurements. According to the conclusion in Chapter 4, a negative correlation showing that with a larger magnetic susceptibility, a lower applied field is required to reach the FMR frequency. Thus from Fig. 5-2, the size dependent susceptibilities should also result in the size dependent FMR field shifts in Fig. 5-3. Plotting these two physical quantities along with the change of sizes, one could obtain this consistent negative correlation between magnetic susceptibilities and FMR fields as shown in Fig. 5-4. Detailed extracted parameters from magnetic and FMR measurements were listed in Table 5-1. It is worthy to note that the resonance field line widths (ΔH) of all $MnFe_2O_4$ sample are within a similar range, except for the 3 nm one, due to the identical structures of the samples. Identical spinel ferrite structure and Mn(II) & Fe(III) composition cause the same effect on magnetic dipolar interaction and spin-spin relaxation. The surface disorder and local defects of the particles play an important role in affecting FMR absorption, and thus for the 3 nm $MnFe_2O_4$, the local lattice structure might be more close to that of the MnO lattice showing a relatively high FMR field and small line width.

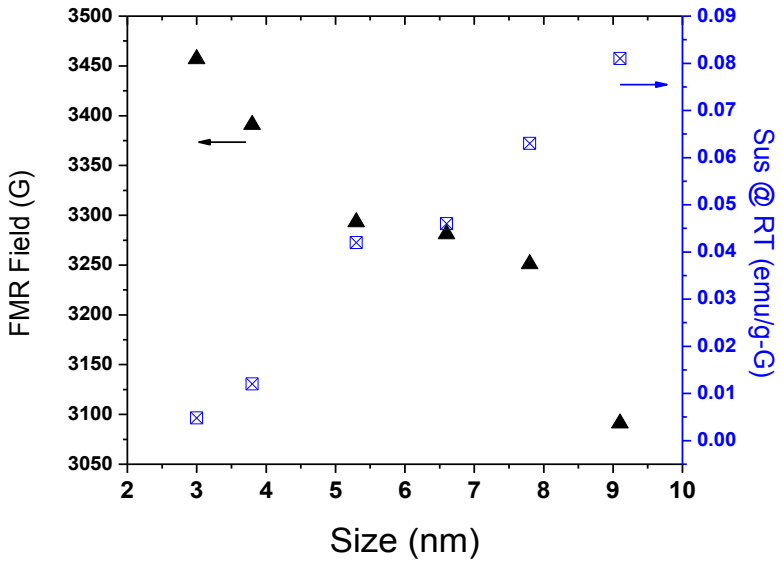

Fig. 5-4 Size dependent FMR absorption field (under 9.88 GHz) and magnetic susceptibility of $MnFe_2O_4$ NPs; the negative correlation between FMR field and susceptibility could also be seen from the plot

5-4-2 Zn(II) substitution $MnFe_2O_4$

In addition to size adjustment, composition changes could also affect the properties and thus the Zn(II) substituted $MnFe_2O_4$ particles were being studied. It is known that Zn(II), in which the electron configuration is d^{10}, exhibits no anisotropy contribution and tends to occupy tetrahedral site in the spinel lattice. Therefore we could expect that with the substitution of Zn^{2+} over Mn^{2+} (d^5), the magnetic dipolar interaction and as well as the inversion degree between Mn^{2+} and Fe^{3+} would be changed and this further affects the magnetic & FMR properties. Fig. 5-5

demonstrates that $Mn_{1-x}Zn_xFe_2O_4$ with x = 0–0.5 (0–50%) could be made successfully through the aminolytic synthesis approach and no detectable impurity phases could be seen on the XRD patterns. The chemical stoichiometry was confirmed with ICP-MS elemental analysis and the ratios of all the samples were consistent with their initial synthesis conditions (the ratios between acetate precursors). As seen in section 5-4-1, particle size could tune the properties and thus in this section, all the $Mn_{1-x}Zn_xFe_2O_4$ particles were controlled within 6.3 ± 0.3 nm so that the effect of Zn(II) substitution could be addressed out alone.

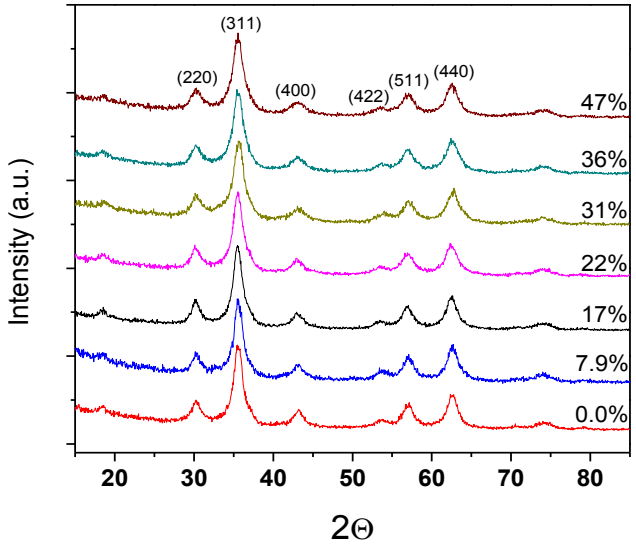

Fig. 5-5 XRD patterns of $Mn_{1-x}Zn_xFe_2O_4$ particles where the Zn(II) percentage were confirmed with ICP-MS and labeled onto the patterns. All samples appeared as single spinel ferrite phase and 6.3 ± 0.3 nm in size fitted by Scherrer equation.

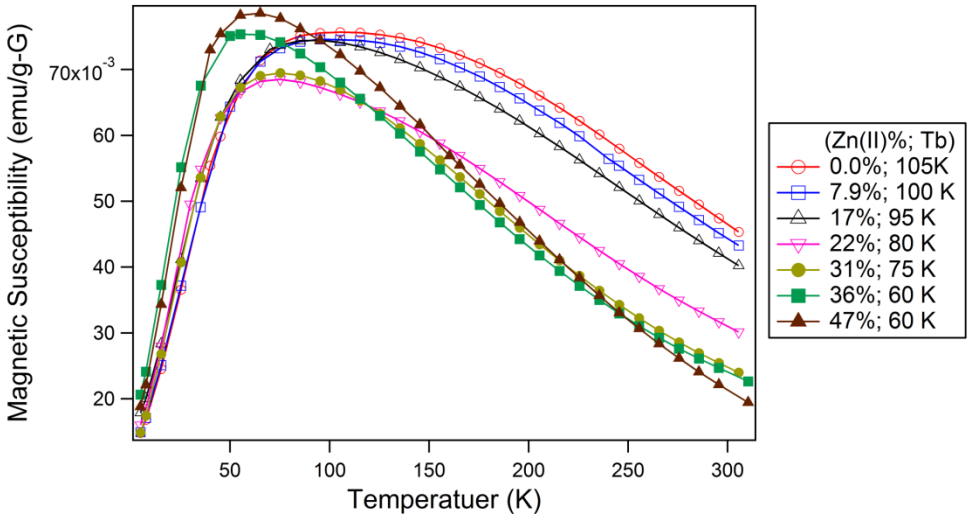

Fig. 5-6 Temperature dependent susceptibility measurements for ~6 nm $Mn_{1-x}Zn_xFe_2O_4$ NPs under 100 G; ; room temperature susceptibilities were extracted in Table 5-1

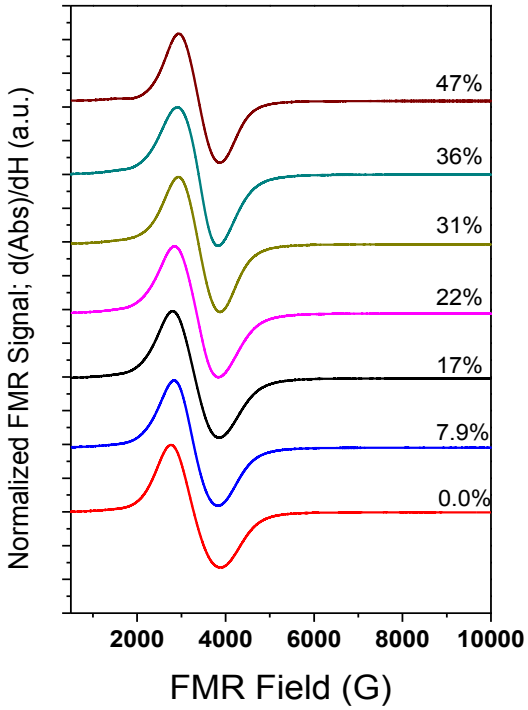

Fig. 5-7 Ferromagnetic resonance (FMR) absorption profiles of ~6 nm $Mn_{1-x}Zn_xFe_2O_4$ NPs under v = 9.88 GHz at room temperature 300 K. Center field = 5125.0 G and sweeping width = 9750.0 G

Temperature dependent susceptibility measurements were conducted under 100 Gauss and the results are shown in Fig. 5-6. With the substitution amount of Zn(II) over Mn(II) increased, the blocking temperature decreased indicating the decrease of the magnetic anisotropy energy since Zn(II) d^{10} denoting no anisotropy contribution. $Mn_{1-x}Zn_xFe_2O_4$ has a blocking temperature in between the range of the T_B of pure $MnFe_2O_4$ and $ZnFe_2O_4$ with similar size (with the $ZnFe_2O_4$ at the lowest end and

$MnFe_2O_4$ at the highest end) and this is consistent with the results in Chapter 4 and literatures. It is interesting to note that Zn(II) substitution could lower and then increase the maximum susceptibility as the substitution amount increases. Zn(II) tends to occupy the tetrahedral sites within the spinel lattice and thus its substitution could result in increasing the difference of magnetic moments between tetrahedral and octahedral sites. Since the magnetic moments in tetrahedral and octahedral sites are anti-parallel to each other, the increase of this difference can directly increase the saturation magnetization as well as the maximum susceptibility. It has been demonstrated that the introduction of Zn(II) into magnetite can increase the net magnetic moment. In addition of the increase in net magnetic moment, the tetrahedral site occupancy of Zn(II) could also lead to the change of Mn(II) and Fe(III) inversion degree and potentially decrease the net moment. And thus in the case here there could be these two factors competing in affecting the maximum susceptibility[2,23]. As for the room temperature susceptibility (at 300 K), a simple trend that depends on Zn(II) substitution amount could be obtained (Table 5-1). The FMR absorption profiles were shown in Fig. 5-7 with first derivative form. All samples revealed similar absorption profiles but their resonance fields shifted toward to higher fields as the Zn(II) substitution amount increased. As shown in Fig. 5-8, the systematic variation of Zn(II) substitution in $MnFe_2O_4$ can tune both the magnetic susceptibility and FMR field.

As the Zn(II) substitution amount went over 30%, the room temperature susceptibility went to the lower end below 0.025 emu/g-G and the FMR achieved to ~3390 G.

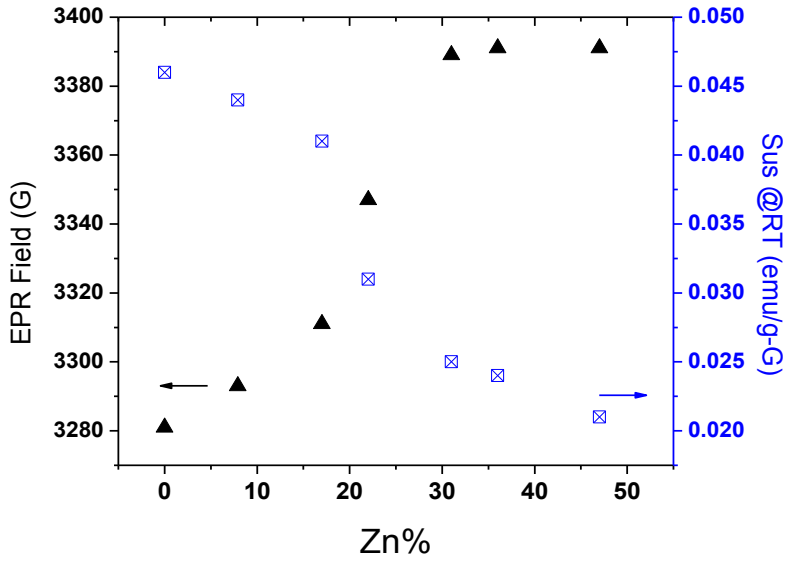

Fig. 5-8 Zn(II)% dependent FMR absorption field (under 9.88 GHz) and magnetic susceptibility of $Mn_{1-x}Zn_xFe_2O_4$ NPs; the negative correlation between FMR field and susceptibility could also be seen from the plot

5-4-3 Co(II) substitution $MnFe_2O_4$

Co(II) with the electron configuration d^7 contributes significant angular momentum and thus can often increase the anisotropy energy. Experimentally it has been reported that $CoFe_2O_4$ nanoparticles has a high blocking temperature (~ room temperature) (Chapter 2 & 4). In addition, the strong spin-orbit coupling interaction of Co^{2+} contributes much in crystalline anisotropy of mixed spinel ferrites and thus has

been reported to lower the FMR field. A series of nanoparticles, Mn-Co ferrite ($Mn_{1-x}Co_xFe_2O_4$, x = 0–0.5) with average size 7.0 ± 0.5 nm, was made to systematically study the effect of Co(II). Note that the other two metal centers, Mn(II) (d^5) and Fe(III) (d^5), both exhibit no anisotropy contribution and thus the effect of the introduction of Co(II) into the $MnFe_2O_4$ system could be easily extracted out. Fig. 5-9 demonstrates that $Mn_{1-x}Co_xFe_2O_4$ with x = 0–0.5 (0–50%) could be made successfully through the aminolytic synthesis approach and no detectable impurity phases could be seen on the XRD patterns. The chemical stoichiometry was confirmed with ICP-MS elemental analysis and the ratios of all the samples were consistent with the ratios between acetate precursors used during the synthesis. Similar to the case in section 5-4-2, all the $Mn_{1-x}Co_xFe_2O_4$ particles were controlled within 7.0 ± 0.5 nm so that the effect of Co(II) substitution could be addressed out alone.

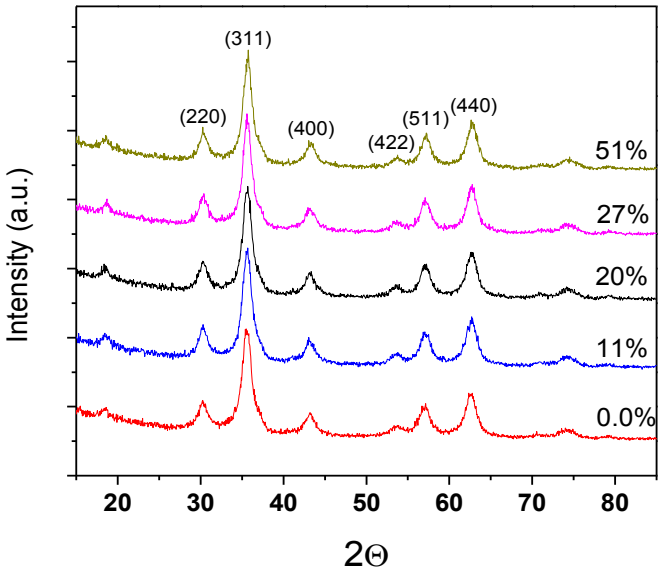

Fig. 5-9 XRD patterns of $Mn_{1-x}Co_xFe_2O_4$ particles where the Co(II) percentage were confirmed with ICP-MS and labeled onto the patterns. All samples appeared as single spinel ferrite phase and 7.0 ± 0.5 nm in size fitted by Scherrer equation.

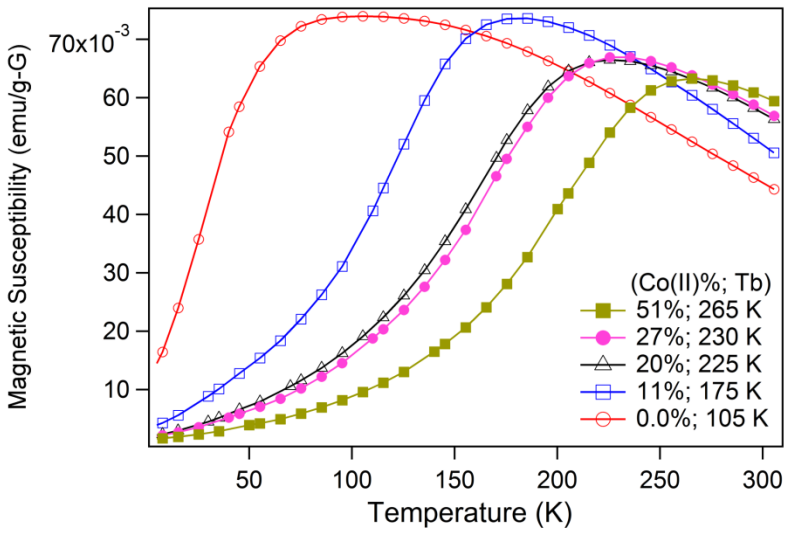

Fig. 5-10 Temperature dependent susceptibility measurements for ~7 nm $Mn_{1-x}Co_xFe_2O_4$ NPs under 100 G; ; room temperature susceptibilities were extracted in Table 5-1

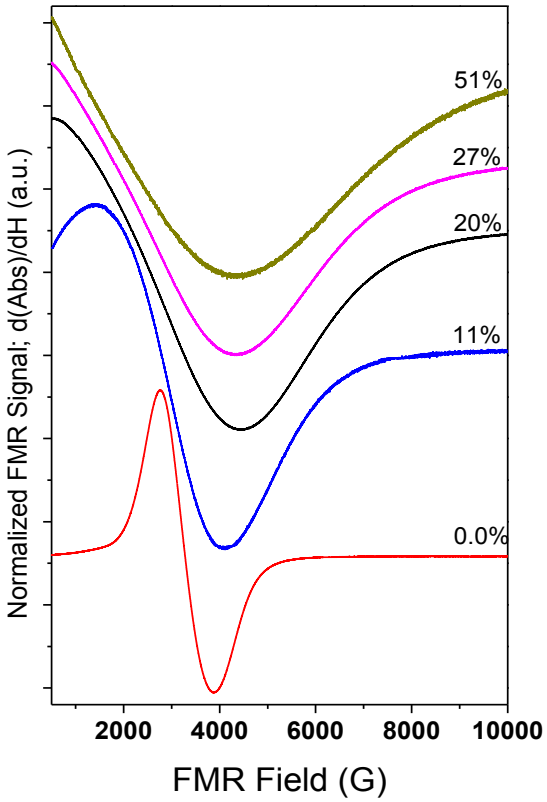

Fig. 5-11 Ferromagnetic resonance (FMR) absorption profiles of ~7 nm $Mn_{1-x}Co_xFe_2O_4$ NPs under ν = 9.88 GHz at room temperature 300 K. Center field = 5125.0 G and sweeping width = 9750.0 G

Temperature dependent susceptibility measurements were conducted under 100 Gauss and the results are shown in Fig. 5-10. With the increase of the Co(II) substitution amount, the blocking temperature increased due to the contribution of anisotropy energy barrier from Co(II) spin-orbit coupling. As the blocking

temperature shifts towards to a higher temperature with Co(II)% increasing, the room temperature susceptibility also increases. Fig. 5-11 shows the FMR absorption profiles of the $Mn_{1-x}Co_xFe_2O_4$ series and the introduction of Co(II) changes not only the FMR field but also the line width. Higher substitution would actually mess up the spectrum (out of the setting range and bad resolution). It has been reported that magnetocrystalline anisotropy from Co(II) $CoFe_2O_4$ could lower the FMR field and broaden the line width[6,13,14,24,25]. Herein, the two FMR effects from Co(II), the field shift and line width broadening, are discussed in succession.

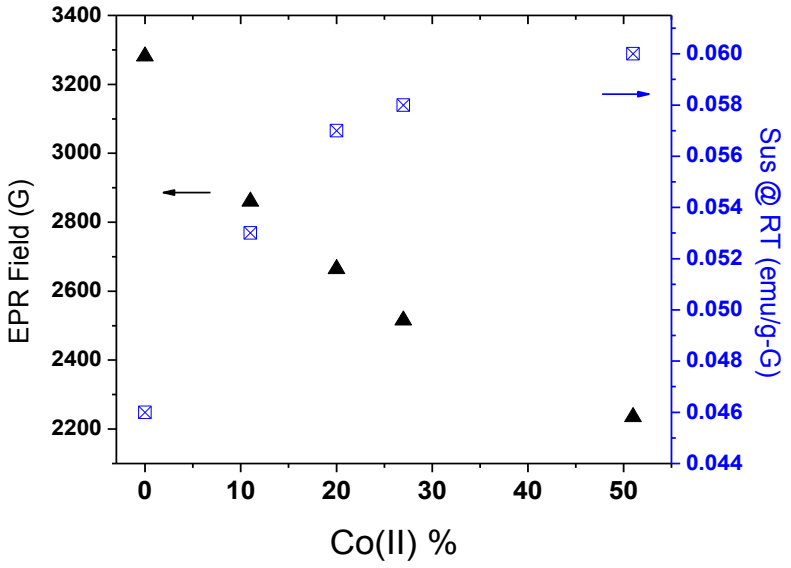

Fig. 5-12 Co(II)% dependent FMR absorption field (under 9.88 GHz) and magnetic susceptibility of $Mn_{1-x}Co_xFe_2O_4$ NPs; the negative correlation between FMR field and susceptibility could also be seen from the plot

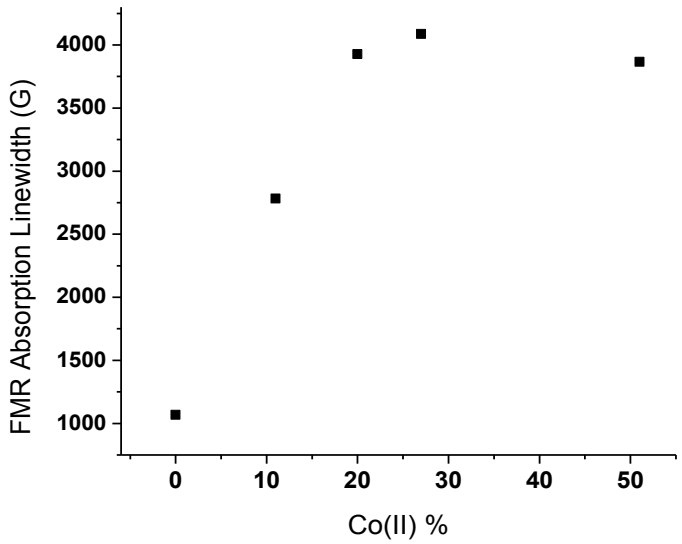

Fig. 5-13 Co(II)% dependent FMR absorption field line width of $Mn_{1-x}Co_xFe_2O_4$ NPs

As shown in Fig. 5-12, the systematic variation of Co(II) substitution in $MnFe_2O_4$ can tune both the magnetic susceptibility and FMR field. As the Co(II) substitution amount increased, the room temperature susceptibility increased as well and this led to the decrease of the FMR field. The negative correlation between magnetic susceptibility and FMR field is in consistence with previous results from other spinel ferrite systems (Chapter 4, 5-4-1 & 5-4-2). Fig. 5-13 displays the line width broadening effect with the Co(II) substitution. Experiment results shows that a small substitution ($Mn_{0.89}Co_{0.11}Fe_2O_4$) could increase the line width ~3 fold (1000 to 3000 G approximately) and when the Co(II) achieve to 50%, the line width tended to maximum out around 4000 G. The FMR line width is mainly affected by the T_2

relaxation, i.e., spin-spin relaxation, which is a process then the excited spins interact with each other causing the decay of the transverse component of the magnetization vector towards its equilibrium value. With the introduction of magnetocrystalline anisotropy from Co(II) into the $MnFe_2O_4$ lattice, the spin-spin relaxation decay becomes more rapidly due to the local field inhomogeneities in the nano-scale, and thus causes the line width broadening in FMR spectrum. Thus in summary, the magnetocrystalline anisotropy from Co(II) increases the room temperature susceptibility so that decreases the FMR field, and also introduces local field inhomogeneity to accelerate T_2 relaxation, which broadens the FMR absorption peak. For further application design, one could control the material magnetocrystalline anisotropy to change the FMR window broadness.

Table 5-1 Sample list with composition, size, extracted magnetic & FMR data

Chemical Formula	Size (nm)	T_B (K)	χ@RT (emu/G-g)	*H* (G)	*ΔH* (G)
$MnFe_2O_4$	3.0	45	0.0048	3457	519
$MnFe_2O_4$	3.8	55	0.012	3391	744
$MnFe_2O_4$	5.3	90	0.042	3293	1164
$MnFe_2O_4$	6.6	105	0.046	3281	1007
$MnFe_2O_4$	7.8	125	0.063	3251	1132
$MnFe_2O_4$	9.1	135	0.081	3091	1278
$Mn_{0.921}Zn_{0.079}Fe_2O_4$	6.0	100	0.044	3293	997
$Mn_{0.83}Zn_{0.17}Fe_2O_4$	6.6	95	0.041	3311	1047
$Mn_{0.78}Zn_{0.22}Fe_2O_4$	6.2	80	0.031	3347	991
$Mn_{0.69}Zn_{0.31}Fe_2O_4$	6.2	75	0.025	3389	934
$Mn_{0.64}Zn_{0.36}Fe_2O_4$	6.0	60	0.024	3391	920
$Mn_{0.53}Zn_{0.47}Fe_2O_4$	6.1	60	0.021	3391	923
$Mn_{0.89}Co_{0.11}Fe_2O_4$	7.3	175	0.052	2860	2782
$Mn_{0.80}Co_{0.20}Fe_2O_4$	6.8	225	0.057	2664	3927
$Mn_{0.73}Co_{0.27}Fe_2O_4$	7.5	230	0.058	2515	4088
$Mn_{0.49}Co_{0.51}Fe_2O_4$	6.8	265	0.060	2235	3867

5-5 Conclusions

In conclusion, three sets of manganese ferrite nanoparticle series were systematically designed, and both size and composition effects on FMR were studied with SQUID and EPR techniques. These three sets of experiments is concluded as following: (1) $MnFe_2O_4$ with the size ranging from 3–9 nm showed that with the increase in size, magnetic susceptibility increased and thus lowered the FMR field. (2) Mn-Zn ferrite ($Mn_{1-x}Zn_xFe_2O_4$, x = 0–0.5) with average size 6.3 ± 0.3 nm were made to study the nonmagnetic element substitution. And it has demonstrated that with the increase of the Zn(II) over Mn(II) in the spinel ferrite lattice, the magnetic susceptibility decreased and thus increased the FMR field. (3) Mn-Co ferrite ($Mn_{1-x}Co_xFe_2O_4$, x = 0–0.5) with average size 7.0 ± 0.5 nm were made to study the substitution of Co(II) which displays significant magnetocrystalline anisotropy from the spin-orbit coupling. It has been showed that with more Co(II) over Mn(II) in the structure, the magnetic susceptibility increased and both the resonance field and line width changed in FMR absorption spectra. The anisotropy from Co(II) increases the room temperature susceptibility so that decreases the FMR field, and also introduces local field inhomogeneity to accelerate T_2 relaxation, which broadens the FMR absorption peak. This work demonstrated detailed relationships between material structures (sizes & compositions) and magnetic properties and provides ways in

designing microwave ferrites in numerous application devices such as circulators, isolators, and frequency limiters.

5-6 References

(1) Cini, A.; Ceci, P.; Falvo, E.; Gatteschi, D.; Fittipaldi, M. *Z. Phys. Chemie-Int. J. Res. Phys. Chem. Chem. Phys.* **2017**, *231*, 745.

(2) Thota, S.; Kashyap, S. C.; Sharma, S. K.; Reddy, V. R. *J. Phys. Chem. Solids* **2016**, *91*, 136.

(3) Harris, V. G.; Geiler, A.; Chen, Y. J.; Yoon, S. D.; Wu, M. Z.; Yang, A.; Chen, Z. H.; He, P.; Parimi, P. V.; Zuo, X.; Patton, C. E.; Abe, M.; Acher, O.; Vittoria, C. *J. Magn. Magn. Mater.* **2009**, *321*, 2035.

(4) Nan, C. W.; Bichurin, M. I.; Dong, S. X.; Viehland, D.; Srinivasan, G. *J. Appl. Phys.* **2008**, *103*.

(5) Pardavi-Horvath, M. *J. Magn. Magn. Mater.* **2000**, *215*, 171.

(6) Singamaneni, S. R.; Martinez, L. M.; Swadipta, R.; Ramana, C. V. *AIP Adv.*

2018, *8*.

(7) Rajagiri, P.; Sahu, B. N.; Venkataramani, N.; Prasad, S.; Krishnan, R. *AIP Adv.* **2018**, *8*.

(8) Angadi, V. J.; Choudhury, L.; Sadhana, K.; Liu, H. L.; Sandhya, R.; Matteppanavar, S.; Rudraswamy, B.; Pattar, V.; Anavekar, R. V.; Praveena, K. *J. Magn. Magn. Mater.* **2017**, *424*, 1.

(9) Yang, X.; Zhou, Z.; Nan, T.; Gao, Y.; Yang, G. M.; Liu, M.; Sun, N. X. *J. Mater. Chem. C* **2016**, *4*, 234.

(10) Sahu, B. N.; Doshi, A. S.; Prabhu, R.; Venkataramani, N.; Prasad, S.; Krishnan, R. *AIP Adv.* **2016**, *6*.

(11) Raita, O.; Popa, A.; Toloman, D.; Badilita, V.; Piticesu, R. R.; Giurgiu, L. M. *J. Optoelectron. Adv. Mater.* **2015**, *17*, 1314.

(12) Pachauri, N.; Khodadadi, B.; Althammer, M.; Singh, A. V.; Loukya, B.; Datta, R.; Iliev, M.; Bezmaternykh, L.; Gudim, I.; Mewes, T.; Gupta, A. *J. Appl. Phys.* **2015**, *117*.

(13) Kumar, A.; Yadav, N.; Rana, D. S.; Kumar, P.; Arora, M.; Pant, R. P. *J.*

Magn. Magn. Mater. **2015**, *394*, 379.

(14) Jnaneshwara, D. M.; Avadhani, D. N.; Prasad, B. D.; Nagabhushana, B. M.; Nagabhushana, H.; Sharma, S. C.; Shivakumara, C.; Rao, J. L.; Gopal, N. O.; Ke, S. C.; Chakradhar, R. P. S. *J. Magn. Magn. Mater.* **2013**, *339*, 40.

(15) Chao, L.; Sharma, A.; Afsar, M. N.; Obi, O.; Zhou, Z. Y.; Sun, N. A. *IEEE Trans. Magn.* **2012**, *48*, 4085.

(16) Salado, J.; Insausti, M.; Lezama, L.; de Muro, I. G.; Goikolea, E.; Rojo, T. *Chem. Mat.* **2011**, *23*, 2879.

(17) Sun, K.; Pu, Z. Y.; Yang, Y.; Chen, L. L.; Yu, Z.; Wu, C. J.; Jiang, X. N.; Lan, Z. W. *J. Alloy. Compd.* **2016**, *681*, 139.

(18) Pachauri, N.; Khodadadi, B.; Singh, A. V.; Mohammadi, J. B.; Martens, R. L.; LeClair, P. R.; Mewes, C.; Mewes, T.; Gupta, A. *J. Magn. Magn. Mater.* **2016**, *417*, 137.

(19) Khan, M. A.; ul Islam, M.; Iqbal, M. A.; Ahmad, M.; Din, M. F.; Murtaza, G.; Ahmad, I.; Warsi, M. F. *Ceram. Int.* **2014**, *40*, 3571.

(20) Khan, M. A.; Islam, M. U.; Ishaque, M.; Rahman, I. Z. *J. Alloy. Compd.*

2012, *519*, 156.

(21) Gama, L.; Hernandez, E. P.; Cornejo, D. R.; Costa, A. A.; Rezende, S. M.; Kiminami, R.; Cost, A. *J. Magn. Magn. Mater.* **2007**, *317*, 29.

(22) Rao, B. P.; Kumar, A. M.; Rao, K. H.; Murthy, Y. L. N.; Caltun, O. F.; Dumitru, I.; Spinu, L. *J. Optoelectron. Adv. Mater.* **2006**, *8*, 1703.

(23) Lai, J. R.; Shafi, K.; Ulman, A.; Loos, K.; Yang, N. L.; Cui, M. H.; Vogt, T.; Estournes, S.; Locke, D. C. *J. Phys. Chem. B* **2004**, *108*, 14876.

(24) He, Y. X.; Pavlidis, S.; Chen, W. Y.; Drew, E.; Zhang, Z. J.; Papapolymerou, J.; Ieee In *2017 Ieee Radio and Wireless Symposium*; Ieee: New York, 2017, p 72.

(25) Cao, X. B.; Gu, L. *Nanotechnology* **2005**, *16*, 180.

CHAPTER 6. FABRICATION AND CHARACTERIZATION OF NANOMAGNETIC FILMS

6-1 Abstract

In this chapter, spinel ferrite nanoparticles described in previous chapters were used in the fabrication of magnetic films in order to fulfill the potential applications in radio frequency (RF) wave transmission components, in particular, the frequency selective limiters. Different attempts utilizing layer-by-layer (LbL) techniques have been tested and stable films up to 5 μm with $CoFe_2O_4$ or $MnFe_2O_4$ on either glass or copper substrates have been produced successfully using the epoxy curing method. Both optical microscopy and SEM (scanning electron microscopy) images demonstrated the film homogeneity. RF wave absorption device for film samples has been developed in collaboration with the Papapolymerou lab in Michigan State University. RF transmission and ferromagnetic resonance data have been studied. Future research direction and ways for improvement of particle loading amount onto the films have also been illustrated.

6-2 Introduction

Wireless applications utilizing the radio frequency (RF) and millimeter wave bands has become more and more widespread as tons of technology needs require all forms of transmissions[1]. As the bands have become more and more crowded, the signals generated by other nearby applications, especially occupying the same or adjacent bandwidth, would become an RF interference or jammer to the local receiver. Currently there are power limiters which are used to select out the signals and protect the receivers by blocking the high power interferences but yet the effect is limited since they're not frequency selective and could often block out the target signals as well[2,3]. Frequency Selective Limiter (FSL) has been developed to capture and suppress the large power interference signal especially applied in a very narrow bandwidth. The FSL can be achieved through different ways but most of the current approaches could result in severe distortion or might require sophisticated topology and manufacturing and increase the cost[2,4,5]. As magnetic ferrite materials have been shown the non-linear signal property, they would be great candidates for FSL materials[6]. In this chapter, spinel ferrites described in the previous chapters have been applied into film forms and the study for the FSL applications has been collaborated with Dr. Papapolymerou group in Michigan State University.

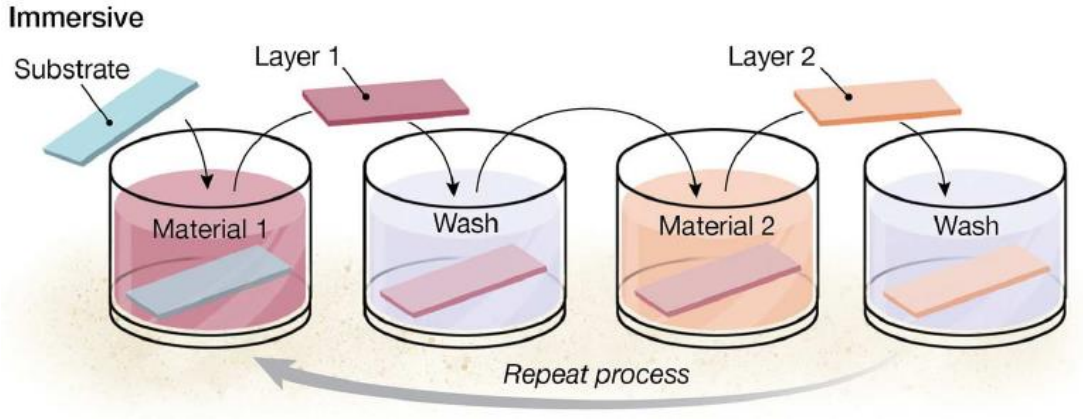

Fig. 6-1 Concept scheme of the basic immersive LbL assembly techniligy. (Illustration credit: A. Burke, C. Lynm, *Science* 2015, *348*.)[7]

Layer-by-layer (LbL) film fabrication technique has been developed and utilized in a wide range of fields. In general, the films are formed by depositing alternating layers of different materials, often oppositely charged, with wash steps in between. This can be accomplished by using various techniques such as immersion, spin, spray, electromagnetism, or fluidics[7-9]. Fig. 6-1 illustrates the basic concepts of immersive LbL assembly, and in addition to polyelectrolytes that could be used as layer materials, various combinations have been studied to achieve the bindings between the layers[8,10-13]. In this research, two main approaches have been studied fully and other potential film making techniques has been discussed. Magnetic films based on spinel

ferrite nanoparticles were further tested and their microwave/ RF absorption was compared with the results from previous chapters.

6-3 Experimental

6-3-1 Preparation of film particles and substrates

Particles were synthesized by aminolytic method described in the previous chapters and the stripping procedure which washes out the surface ligands would be performed prior to film fabrication. Briefly, as-synthesized particles were added to 1:1 (v/v) 10 M $NaOH_{(aq)}$ + ethanol and the mixture was either stirred for 1 hour or sonicated for 15 min. And then the particles were collected with a magnet and rinsed with water. The above protocols were repeated for two more times. Finally the particles were again mixed with another fresh 1:1 (v/v) 10 M $NaOH_{(aq)}$ + ethanol and the mixture was let stirred overnight. The particles were collected with a magnet and rinsed thoroughly with water and then ethanol prior to film making. The glass substrates were cleaned with 3 M $HCl_{(aq)}$ in the sonication bath for 20 min. and then 3 M $NaOH_{(aq)}$ for another 20 min. so that no industrial contaminations would be left on the surface.

6-3-2 Layer by layer fabrication of nanoparticle films via polyelectrolytes method

Firstly, 5 layers polyelectrolytes as the base layer was made before applying the nanoparticle layers. The base layer was composed of alternating layers of sodium poly(styrenesulfonate) (PSS), the polyanion, and poly(diallyldimethylammonium chloride) (PDDA), the polycation; in order to provide a solid ionic surface onto the substrate. As the particles were used directly after stripping, they would be surface charged with negative potential due to the hydroxides coating. Thus the film could be built through the electrostatic interaction between oppositely charged components via alternating layers of PDDA and nanoparticles (NPs). The sequential absorptions of PDDA and NPs were repeated until the film thickness has been achieved (normally at least 10 sets of PDDA/ NPs). The thin film was then spin coated with a layer of Torlon TF4000 polymer to both chemically and physically protect the underlying particle film. Fig. 6-2 illustrates the film building concept of this polyelectrolytes method.

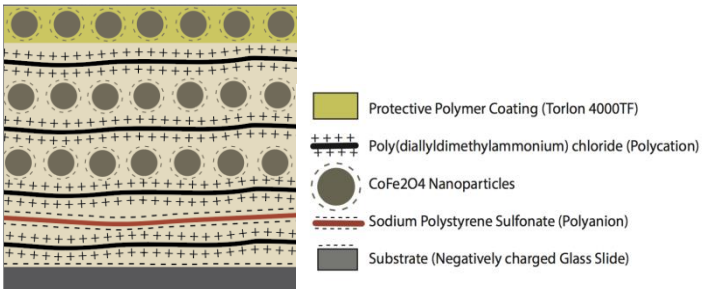

Fig. 6-2 Illustration of the LbL polyelectrolytes method (drawn by Eric Drew)

6-3-3 Layer by layer fabrication of nanoparticle films via epoxy curing method

The $CoFe_2O_4$ or $MnFe_2O_4$ nanoparticles were chemically bound to the glass substrate using the S_N2 nucleophilic addition between the surface-coated amine groups and epoxy groups. Hence two sets of surface modified particles were prepared, namely, 3-aminotriethoxypropylsilane coated particles and (3-glycidyloxypropyl) trimethoxysilane coated particles. The glass slides were surface modified with (3-glycidyloxypropyl) trimethoxysilane prior to particle attachment.

Epoxy coated slides

(3-glycidyloxypropyl) trimethoxysilane ethanol solution was prepared (1% v/v) and the glass slide was dipped into the solution and allowed to soak for 30 minutes.

After the slide was removed from the solution, it was air dried and ready to be further coated with particles.

Amine/ epoxy coated $CoFe_2O_4$ particles

The $CoFe_2O_4$ nanoparticles were synthesized and followed with NaOH stripping ensuring that the particle surface is bare without other capping agent. 3-Aminotriethoxypropylsilane ethanol solution was prepared (1% v/v) and bare particles were added to it (1 mg/ 1mL). The solution was stirred overnight. The particles were collected through a magnet and washed with ethanol for three times to remove any excess coating agent. The particles were then re-suspended into ethanol and agitated before being used. The same procedure was followed for epoxy coated particles but the (3-glycidyloxypropyl)trimethoxysilane ethanol solution was used.

Layer-by-Layer Fabrication

The glass slide was dipped into amine coated particle solution and then epoxy coated particle solution. Each dipping step was set to 30 minutes and followed with rinsing and air-drying. With the alternating dipping from these two solutions, a film with certain thickness could be made. The film was then spin coated with a layer of

Torlon TF4000 polymer to both chemically and physically protect the underlying particle film.

6-4 Results and discussion

6-4-1 Characterization of film particles

Two basic spinel ferrite nanoparticle systems, $CoFe_2O_4$ and $MnFe_2O_4$, were used as the magnetic film material. Both types of particles could be produced with high yield and controllable sizes steadily and successfully with the aminolytic method as described in Chapter 2. The as synthesized particles were surface coated with oleylamine as the capping agent so that while processing the films, the stripping procedure was necessary to remove the surface organic ligands. The bare particles maintained the same crystallinity and average size and also presented similar magnetic performances. Fig. 6-3 ,6-4 and 6-5 show the basic characterizations of typical particles used as the film materials. Both XRD and SQUID results were in accordance with results from previous chapters. While sizes could be tuned from the synthesis, ~8 nm $CoFe_2O_4$ and ~7 nm $MnFe_2O_4$ were most commonly used.

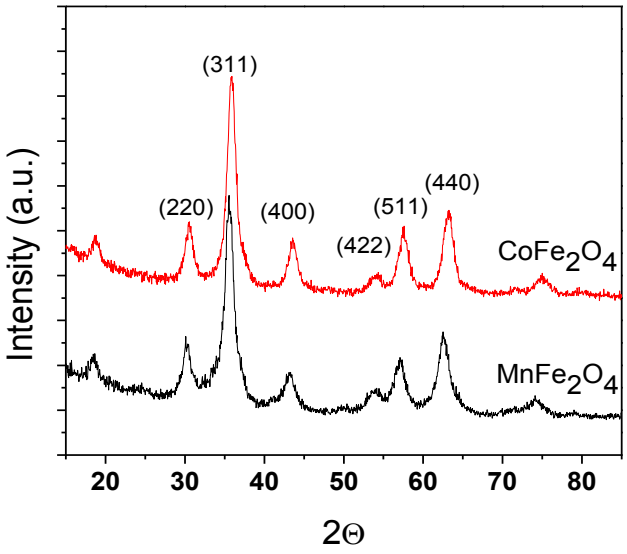

Fig. 6-3 XRD patterns for typical particle samples used for film fabrication

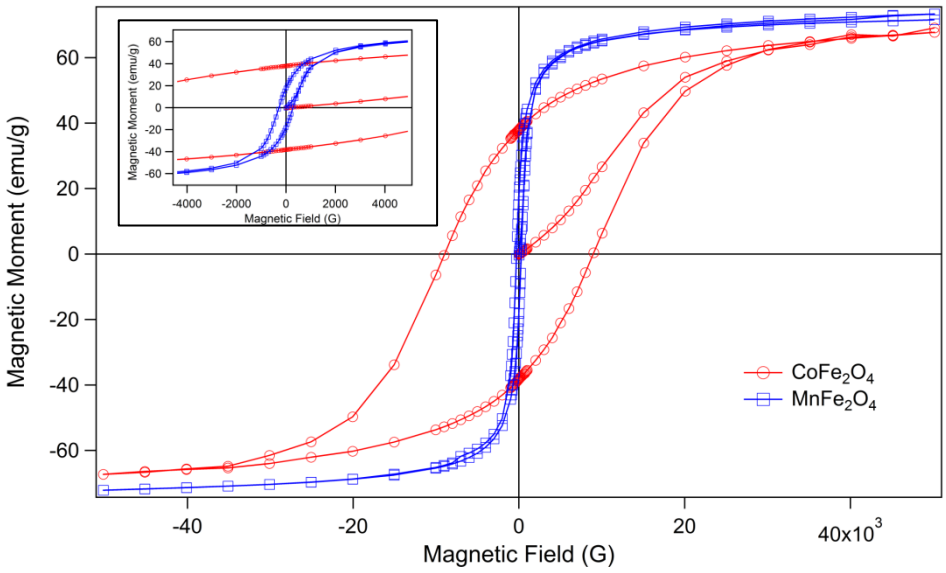

Fig. 6-4 Hysteresis curves at 5 K for $CoFe_2O_4$ and $MnFe_2O_4$ NPs

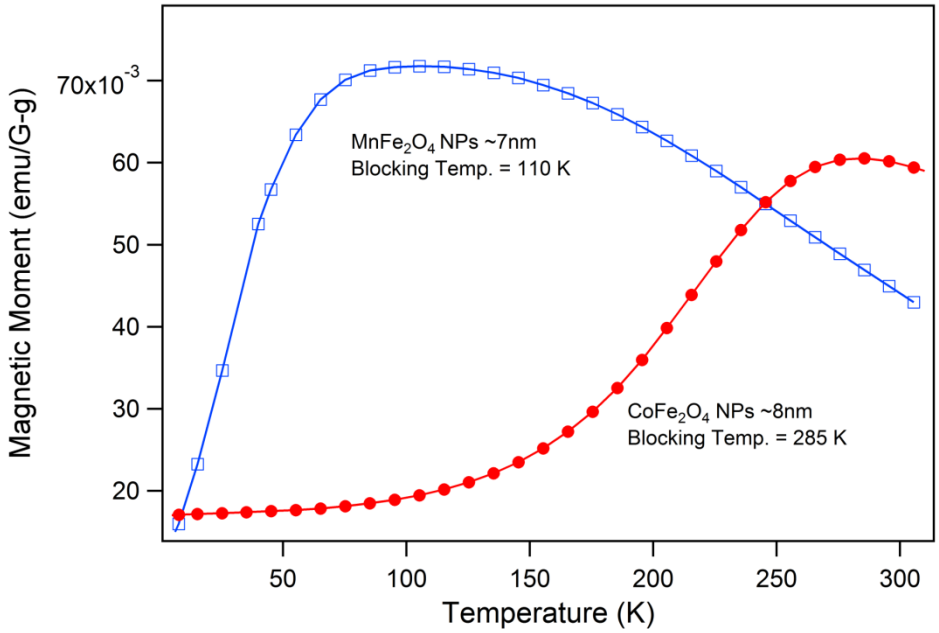

Fig. 6-5 Temperature dependent susceptibility measurements for $CoFe_2O_4$ and $MnFe_2O_4$ NPs

6-4-2 $CoFe_2O_4$ Thin Films via polyelectrolyte LbL method

In this polyelectrolyte LbL attempt, the film was designed to be built through the electrostatic interaction between oppositely charged components. Depending on the surface charge of the particles, one could pick corresponding poly cation/ anion to accomplish the absorption events. After several trials, under the requirement that the particle solution could form a suspension and the solvents between different dipping solutions could be miscible, the combination of bare NPs in water with pH value > 10 and PDDA polycation was selected. The stripped NPs are bare without surface

capping agents, and thus they tend to aggregate unless the repelling force from the charged surface (hydroxide groups containing) is effective enough in the suspended solvent. Several attempts have been made, including recoating the particles with other ligands, and it has been concluded that bare particles would be best suspended in water with a solution pH value > 10 (pH adjustment with 12 M $NaOH_{(aq)}$ if needed). Since the particle surface would consist of hydroxides from the strong base stripping process, particles could suspend well in the basic solution due to the repelling force among the negative charge potential. PDDA would be used as the polycation to pair with the NPs solution achieving the electrostatic interactions in between absorption layers. It is worth to note that the initial base layer composing by alternating layers of PSS and PDDA is necessary to provide a solid ionic surface onto the substrate so that the film building process can be carried out properly on the surface.

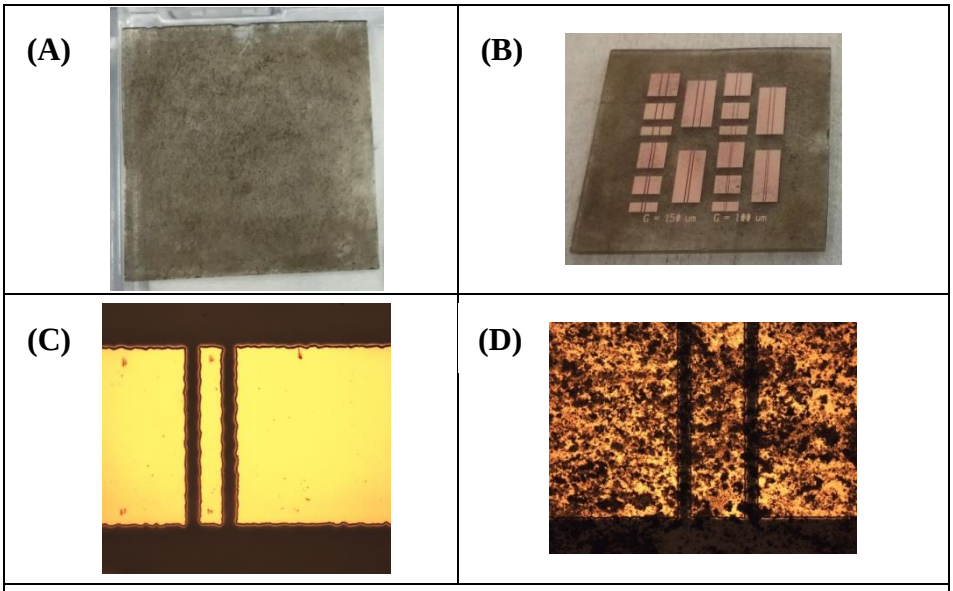

Fig. 6-6 Representative images for the film upon 1 inch × 1 inch soda lime glass substrate. (A) Photo picture. (B) Film with metal wires used for RF wave measurements. (C) Control image under microscope of slide + wires only; without the particle film. (D) Film with metal wires under microscope; film voids could be observed.

Fig. 6-6 shows how the films look via this fabrication route and as seen in panel (A), though particles could indeed be added on to the substrate, the roughness could be seen by eyes since the particles might still form clusters in the suspension. Panel (B) shows the assemble with metals for RF wave absorption measurement device and (C) and (D) are pictures under microscopy with the metal line onto the films. Panel (C) shows "the glass slide (the substrate) + metal lines" only and it was taken as a control comparison. In (D), the particle clustering could be observed. The films fabricated by

this method appeared to change the RF wave measurements significantly in background which revealed potentials for further applications (in cooperation with Dr. Papapolymerou in Michigan State University). However the particle loading amount was too low to give distinctive absorption frequencies in conventional coplanar waveguide (CPW) transmission line. Thus an alternative film fabrication method was needed to solve the clustering and loading issues.

6-4-3 Nanomagnetic films via epoxy curing LbL method

In order to achieve a better film quality, different approaches have been tested. Among various attempts, the LbL adsorption based on the covalent bonds formation through epoxy curing has been providing stable particle films and the film thickness could reach to micro meter range. The general idea is to chemically bind the particles onto the substrate using the S_N2 nucleophilic addition between amine groups and epoxy groups. Hence the proper coating of the particles with ligands is essential and how to choose the compounds for epoxy curing pairs was one of the main challenges developing the method. In order to satisfy the following conditions: 1) proper functional groups would stick out for adsorption after ligands coating onto the particles, 2) coated particles would suspend in corresponding solvents so that the

adsorption process could take place, and 3) the substrate could be coated with proper functional groups and the surface hydrophilicity could match the particle suspensions. It has been found that using 3-aminotriethoxypropylsilane and (3-glycidyloxypropyl) trimethoxysilane as the coating compounds and ethanol as the solvent could fulfill the above conditions and thus the protocol described in 6-3-3 was developed.

Fig. 6-7 shows the typical films made through the epoxy curing LbL method. The edge roughness and not evenly covered areas were mainly caused by the imperfect tweezers handling technique. As shown in Fig. 6-7 the center area where has been undisturbed during the dipping process appeared smooth surface covered with uniform particle layers. Both bare glass slides (A) and slides pre-coated with a copper layer (B) were used as substrates. While glass slides could directly be surface modified with silane compounds through hydrolysis and condensation, i.e. forming (-Si-O-Si-) bonds, the copper coated substrates tend to have better affinity with acid type small chelating groups. Herein, considering cost and effect, the phosphonic acid based compound: 3-phosphonopropionic acid was used to modify the copper surface with a layer of carboxylate groups. This layer of carboxylate groups could further react with amine-coated particles and successfully “attach” the first layer of particles through amide bonding formation. The copper substrate was used to accommodate different microwave devices.

(A) 	**(B)** 
Fig. 6-7 Representative images for the film by LbL epoxy curing method upon 1 inch × 1 inch (A) glass (B) copper substrate.	

Film homogeneity has been examed through different microscopic techniques. Fig. 6-8 shows the images under optical microscopy with scale bars representing 5 μm. Panel (A) shows the controlled background image captured through picturing the bare glass slide. The dark spots under the view did not move while moving the whole slide and thus they were from the inner lens contamination. (B) is the image of film samples and compared to (A), the brightness is significantly darker indicating the presence of the particle layers. Note that the lens contamination spots were a lot less easy to see due to the darker particle contract. No obvious texture contrast could be seen. Panel (C) is another controlled experiment showing the area that was scratched purposely and the texture contrast could be observed. This has demonstrated the uniformity of the film sample under micrometer range.

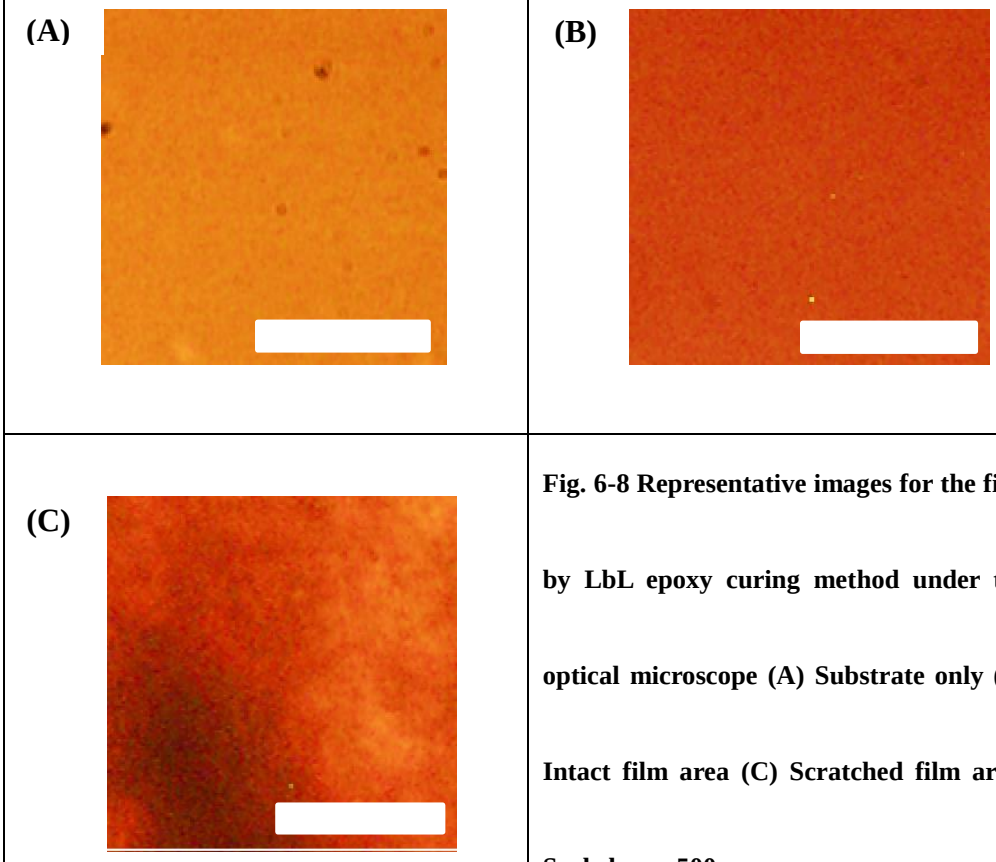

Fig. 6-8 Representative images for the film by LbL epoxy curing method under the optical microscope (A) Substrate only (B) Intact film area (C) Scratched film area. Scale bar = 500 μm

Other than the optical microscope, SEM has also been used to observe the film under nanometer range. SEM samples were prepared by peeling layers of films off from the substrate with conductive carbon tape. In this case, the film layer micro-arrangements could be preserved under SEM without the complexity of loading up the whole setup including the substrate. As shown in Fig. 6-9, no significant cracking or inhomogeneity could be seen and the film layer-layer arrangement could

be observed around the boundary areas created through tape peeling. Note that the voids among the aggregations increased throughout the SEM measurement duration and this could be explained by the damage of organic components under the exposure of vacuum environment.

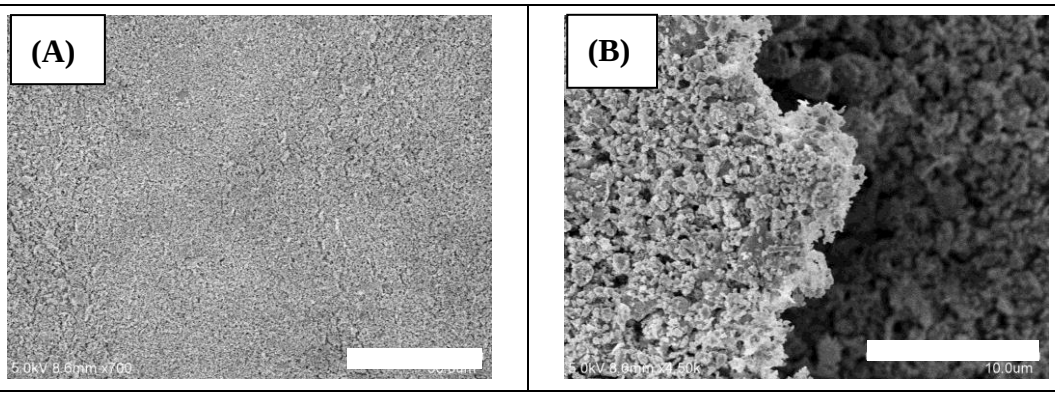

Fig. 6-9 Representative SEM images for the film by LbL epoxy curing method.

Scale bar = (A) 50.0 μm (B) 10.0 μm

6-4-4 Direction of future work

All different "generations" of films have been sent to the collaborator testing out the performance on the RF wave absorption and at the meantime the measurement setup as well as the film incorporation method have been changed/ adjusted in order to get a better reading. In this section, the major combinations of "film + device set up"

would be briefly introduced and the directions for improvements would be discussed. The first attempt that showed promising measurements was the coplanar waveguide (CPW) transmission lines onto a $CoFe_2O_4$ film made through polyelectrolyte LbL method. A significant increase in the group delay could be observed with the magnetic film indicating certain interactions between the magnetic film and the RF transmission signals. Due to the signal weakness, more dense film and better device were required to extract more information from the measurements. While a resonator type of device has been under development at the end of the collaborator, the film processing including the type of particles and method of fabrication has been studied extensively in the Zhang group.

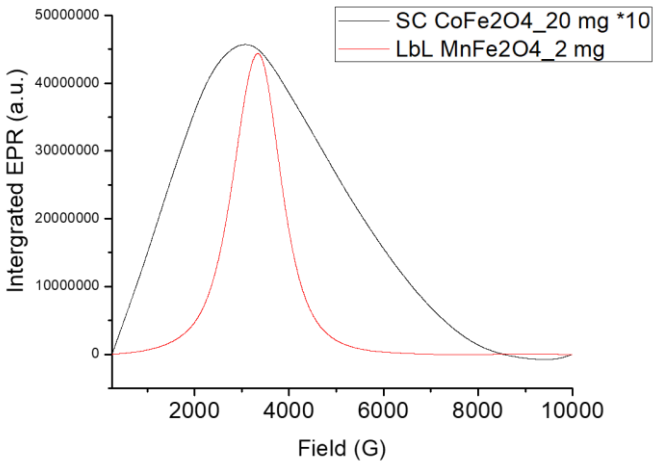

Fig. 6-10 FMR measurement of film particle samples

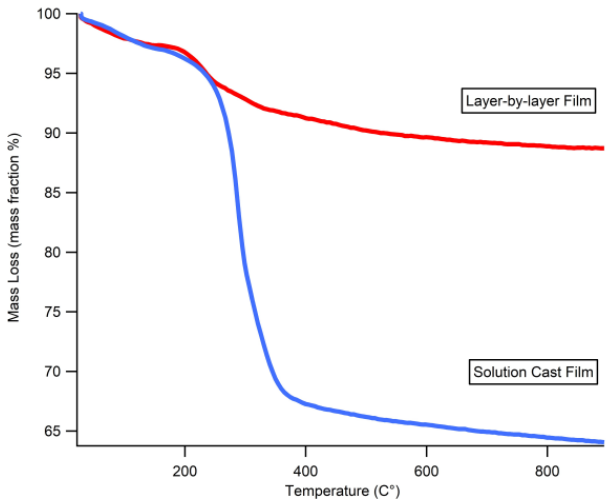

Fig.6-11 TGA curves for LbL and SC films showing particle loading densities of 90% and 65% for LbL and SC respectfully. (Conducted by Eric Drew)

According to previous chapters, different spinel ferrite nanoparticles appear different room temperature susceptibility and thus their powder form samples have different FMR fields under the same input frequency. The sample anisotropy also affects the line width of the FMR peak and thus can affect the spectra resolution. As shown in Fig. 6-10, the strong spin-orbit coupling arising from Co^{2+} could broaden the FMR absorption profile and thus $CoFe_2O_4$ tends to be a lot less sensitive than $MnFe_2O_4$ in FMR spectrum. In addition to particle types, significantly increasing the particle loading amount upon the film could also improve the signal intensity. Although LbL film fabrication technique has been developed for decades and proved to produce high-quality nanoparticle thin films with high loading density (as shown in Fig. 6-11), thickness of several micro-meter was pretty much the upper limit for

"thick films" (in the case of the epoxy curing LbL method here, thickness maximum ~ 5 μm). Thus the solution casting (SC) method has been pretty common in industrial manufacturing for films with thickness in micro-meter range and thus it is the inevitable direction for studies of thicker film production methods. Mr. Eric Drew in the Zhang group is currently working on improving the SC method (current methodology is in the section **6-7 Appendices**). It is worthy to note that the LbL process produces more condensed magnetic films than the SC method, but however it is less time efficient than the latter in producing thicker films since the thickness of SC films (> 100 μm) could achieve more than 20 times of that of LbL films. Combined with the RF transmission cavity setup developed in the Papapolymerou group, which consists the 3-D printed test bed with a tapered microstrip line integrating with the magnetic film, the 3-D printed clamping and supporting structures, better signal to noise ratio from the measurements could be expected.

6-5 Conclusions

In conclusion, different approaches for the fabrication of nanomagnetic films have been developed and the measurements of RF transmission have been studied in the collaboration with the Papapolymerou lab from Michigan State University. Two main LbL methods have been described thoroughly and the films from the epoxy curing approach have shown great homogeneity under SEM and the thickness could be achieved up to 5 μm. According to previous chapters and the RF measurements from the collaborator, $MnFe_2O_4$ nanoparticles have stronger ability in increasing the group delay than the $CoFe_2O_4$ nanoparticles. In addition, a positive linear relationship could be found between the magnetic film thickness and the amount of group delay, i.e., thicker magnetic film introduces more group delay. Therefore for the future research direction, the SC method would be focused in the thicker film production and the cavity type RF transmission setup would be developed and revised for better signal requisition.

6-6 References

(1) Wang, C. X.; Haider, F.; Gao, X. Q.; You, X. H.; Yang, Y.; Yuan, D. F.; Aggoune, H. M.; Haas, H.; Fletcher, S.; Hepsaydir, E. *IEEE Commun. Mag.* **2014**, *52*, 122.

(2) van Wanum, M.; van Vliet, F. E. *IEEE Trans. Microw. Theory Tech.* **2013**, *61*, 3034.

(3) Givernaud, J.; Crunteanu, A.; Orlianges, J. C.; Pothier, A.; Champeaux, C.; Catherinot, A.; Blondy, P. *IEEE Trans. Microw. Theory Tech.* **2010**, *58*, 2352.

(4) Adam, J. D. *IEEE Microw. Mag.* **2014**, *15*, 45.

(5) Adam, J. D.; Winter, F. *IEEE Trans. Magn.* **2013**, *49*, 956.

(6) Eerenstein, W.; Mathur, N. D.; Scott, J. F. *Nature* **2006**, *442*, 759.

(7) Richardson, J. J.; Bjornmalm, M.; Caruso, F. *Science* **2015**, *348*.

(8) Richardson, J. J.; Ejima, H.; Lorcher, S. L.; Liang, K.; Senn, P.; Cui, J. W.; Caruso, F. *Angew. Chem.-Int. Edit.* **2013**, *52*, 6455.

(9) Zhang, X.; Chen, H.; Zhang, H. Y. *Chem. Commun.* **2007**, 1395.

(10) Rydzek, G.; Thomann, J. S.; Ben Ameur, N.; Jierry, L.; Mesini, P.; Ponche, A.; Contal, C.; El Haitami, A. E.; Voegel, J. C.; Senger, B.; Schaaf, P.; Frisch, B.; Boulmedais, F. *Langmuir* **2010**, *26*, 2816.

(11) Ott, P.; Trenkenschuh, K.; Gensel, J.; Fery, A.; Laschewsky, A. *Langmuir* **2010**, *26*, 18182.

(12) Kotov, N. A. *Nanostruct. Mater.* **1999**, *12*, 789.

(13) Decher, G. *Science* **1997**, *277*, 1232.

6-7 Appendices (Developed by Mr. Eric Drew)

Fabrication of $CoFe_2O_4$ Films via Solution Casting Method

Epoxy coated slides and particles

(3-glycidyloxypropyl)trimethoxysilane ethanol solution was prepared (1% v/v) and the glass slides and particles were dipped/ soaked into the solution individually. The glass slide was removed from the solution after 12 hours and air-dried. The particles were collected through a magnet after stirring overnight and washed with ethanol for three times to remove any excess coating agent. The coated particles were suspended in an appropriate amount of dichloromethane.

Film Casting

Approximately 10-20% (w/w) poly(methyl methacrylate) PMMA was added to the particle DCM solution and stirred for approximately 30 minutes before the solution was cast onto the substrate. With a syringe the nanoparticle solution was applied to the prepared substrate evenly, allowing the solution to flood above the substrate. The film was air-dried and stored in a descator until treated with Torlon protective coating. The film was then protected by spin-coating a layer of Torlon TF4000 polymer onto the surface to both chemically and physically protects the underlying film.